

Old Dominion University

ODU Digital Commons

Mechanical & Aerospace Engineering Theses & Dissertations

Mechanical & Aerospace Engineering

Spring 2020

Rotorcraft Blade Angle Calibration Methods

Brian David Calvert Jr.

Old Dominion University, brian.calvert75@gmail.com

Follow this and additional works at: https://digitalcommons.odu.edu/mae_etds



Part of the [Aerospace Engineering Commons](#), and the [Applied Statistics Commons](#)

Recommended Citation

Calvert, Brian D.. "Rotorcraft Blade Angle Calibration Methods" (2020). Master of Science (MS), Thesis, Mechanical & Aerospace Engineering, Old Dominion University, DOI: 10.25777/81he-th14
https://digitalcommons.odu.edu/mae_etds/315

This Thesis is brought to you for free and open access by the Mechanical & Aerospace Engineering at ODU Digital Commons. It has been accepted for inclusion in Mechanical & Aerospace Engineering Theses & Dissertations by an authorized administrator of ODU Digital Commons. For more information, please contact digitalcommons@odu.edu.

ROTORCRAFT BLADE ANGLE CALIBRATION METHODS

by

Brian David Calvert Jr.
B.S.E 2018, James Madison University

A Thesis Submitted to the Faculty of
Old Dominion University in Partial Fulfillment of the
Requirements for the Degree of

MASTER OF SCIENCE

AEROSPACE ENGINEERING

OLD DOMINION UNIVERSITY

May 2020

Approved by:

Drew Landman (Director)

Gene Hou (Member)

Miltos Kotinis (Member)

ABSTRACT

ROTORCRAFT BLADE ANGLE CALIBRATION METHODS

Brian David Calvert Jr.
Old Dominion University, 2020
Director: Dr. Drew Landman

The most vital system of a rotorcraft is the rotor system due to its effects on the overall flight quality of the vehicle. Therefore, it is of importance to be able to accurately determine blade position during flight so that fine adjustments can be made to ensure a safe and efficient flight. In this study, a current calibration method focusing on the pitch, flap, and lead-lag blade angles is analyzed and found to have larger than acceptable error associated with the sensor calibrations. A literature review is conducted which reveals four novel methods that can potentially increase the accuracy of the sensor calibrations. An uncertainty analysis is conducted aiding in the decision of which of the four methods would best improve the calibration accuracy. The results conclude that a simpler method can be applied and calibration times can greatly be reduced while increasing the accuracy of the calibration. Finally, a new calibration method is proposed utilizing the newly chosen sensor that can be later implemented into the system.

Copyright, 2020, by Brian David Calvert Jr., All Rights Reserved.

This thesis is dedicated to my family and loving girlfriend, Tara Carrico, for all of the support and motivation they provided during my research.

ACKNOWLEDGMENTS

I would like to thank my thesis director, Dr. Drew Landman, for his guidance and support throughout the process of writing this thesis. I would also like to thank Dr. Kenneth Toro for guiding me and providing me with the opportunity to conduct this research. Additionally, I want to thank the committee members, Dr. Hou and Dr. Kotinis for their contributions to this thesis.

NOMENCLATURE

SMR	<i>Spherically Mounted Retroreflector</i>
IFM	<i>Interferometer</i>
ADM	<i>Absolute Distance Meter</i>
CCD	<i>Charged Coupled Device</i>
CMOS	<i>Complementary Metal Oxide Semiconductor</i>
CMA	<i>Coordinate Measurement Arm</i>
MEMS	<i>Micromechanical Systems</i>
FOG	<i>Fiber Optic Gyroscope</i>
RLG	<i>Ring Laser Gyroscope</i>
ANN	<i>Artificial Neural Network</i>
ARW	<i>Angle Random Walk</i>
IMU	<i>Inertial Measurement Unit</i>
CMM	<i>Coordinate Measurement Machine</i>
A_R	<i>Rotational Axis</i>
O_H	<i>Hub Origin</i>
O_W	<i>World Origin</i>
Ψ	<i>Yaw</i>
θ	<i>Pitch</i>
φ	<i>Roll</i>
d	<i>Distance</i>
Θ	<i>Azimuth angle</i>
Φ	<i>Elevation angle</i>
f	<i>Focal length</i>
γ	<i>Viewing angle</i>
u	<i>X pixel coordinate</i>
v	<i>Y pixel coordinate</i>

σ_x	<i>Uncertainty in x component</i>
σ_y	<i>Uncertainty in y component</i>
σ_z	<i>Uncertainty in z component</i>
ε_{bias}	<i>Bias error</i>
ε_{ARW}	<i>Angle random walk error</i>
ω_E	<i>Earth rotation rate</i>
O_g	<i>Gyroscope origin</i>
Ψ	<i>X-Axis offset</i>
φ	<i>Gyroscope latitude location</i>
R_x	<i>X rotation matrix</i>
R_y	<i>Y rotation matrix</i>
R_z	<i>Z rotation matrix</i>
R_{XYZ}	<i>Combined rotation matrix</i>

TABLE OF CONTENTS

	Page
LIST OF TABLES.....	viii
LIST OF FIGURES.....	x
Chapter	
1. INTRODUCTION AND BACKGROUND.....	1
1.1 PROBLEM STATEMENT	1
1.2 OBJECTIVES	2
1.3 ROTORCRAFT BACKGROUND	2
1.3.1 Hub Assembly Components	2
1.3.2 Blade Position During Flight	6
1.3.2.1 Pitch	7
1.3.2.2 Flap	8
1.3.2.3 Lead-Lag	10
2. CURRENT SYSTEM.....	12
2.1 Current Calibration Process.....	13
2.2 Data Analysis of Blade Calibration.....	16
2.2.1 Blade Pitch.....	16
2.2.2 Blade Flap:.....	28
2.2.3 Blade Lead-Lag.....	38
2.3 Summary	48
3. LITERATURE REVIEW	50
3.1 LASER TRACKER.....	50
3.1.1 Historic Background	50
3.1.2 Concepts of Operation	51
3.1.3 Case Study	58
3.2 PHOTOGRAMMETRY	62
3.2.1 History/ Background.....	62
3.2.2 Concepts of Operation	63
3.2.3 Case Study	66
3.3 Coordinate Measurement Arm	70

Chapter	Page
3.3.1 Historic Background	70
3.3.2 Concept of Operation.....	71
3.3.3 Case Study	74
3.4 GYROSCOPE	76
3.4.1 Historic Background	76
3.4.2 Concept of Operation.....	77
3.4.3 Case Study	80
4. UNCERTAINTY ANALYSIS	85
4.1 Propagation of Error.....	85
4.1.1 Laser Tracker	87
4.1.2 Stereo Vision Camera	95
4.1.3 Coordinate Measurement Arm.....	102
4.1.4 Gyroscope	109
4.2 Monte Carlo Method	115
4.2.1 Gyroscope	117
5. PROPOSED CALIBRATION METHOD	120
6. CONCLUSION AND FUTURE WORK.....	124
REFERENCES.....	126
APPENDIX	134
Camera Uncertainty.....	134
Laser Tracker Uncertainty.....	138
Coordinate Measurement Arm Uncertainty	140
Gyroscope Uncertainty	142
Gyroscope Monte Carlo	145
VITA.....	148

LIST OF TABLES

Table	Page
Table 1: Blade Pitch Sensor Run Order	18
Table 2: ANOVA table blade 1	21
Table 3: ANOVA table blade 2	21
Table 4: ANOVA table blade 3	21
Table 5: ANOVA table blade 4	22
Table 6: Lack of Fit table blade 1	22
Table 7: Lack of Fit table blade 2	23
Table 8: Lack of Fit table blade 3	23
Table 9: Lack of Fit table blade 4	23
Table 10: Summary of fit table blade 1	25
Table 11: Summary of fit table blade 2	26
Table 12: Summary of fit table blade 3	26
Table 13: Summary of fit table blade 4	26
Table 14: Flap Sensor Run Order	29
Table 15: ANOVA table blade 1	32
Table 16: ANOVA table blade 2	32
Table 17: ANOVA table blade 3	32
Table 18: ANOVA table blade 4	32
Table 19: Lack of Fit table blade 1	33
Table 20: Lack of Fit table blade 2	33
Table 21: Lack of Fit table blade 3	34
Table 22: Lack of Fit table blade 4	34
Table 23: Summary of fit table blade 1	36
Table 24: Summary of fit table blade 2	36
Table 25: Summary of fit table blade 3	36
Table 26: Summary of fit table blade 4	36
Table 27: Lead-Lag Run Order	39
Table 28: ANOVA table blade 1	42
Table 29: ANOVA table blade 2	42
Table 30: ANOVA table blade 3	42
Table 31: ANOVA table blade 4	42
Table 32: Lack of Fit table blade 1	43
Table 33: Lack of Fit table blade 2	43
Table 34: Lack of Fit table blade 3	44
Table 35: Lack of Fit table blade 4	44
Table 36: Summary of fit table blade 1	46
Table 37: Summary of fit table blade 2	46
Table 38: Summary of fit table blade 3	46
Table 39: Summary of fit table blade 4	46

Table	Page
Table 40: Standard Deviation of Sensors.....	48
Table 41: Summary of Results.....	61
Table 42: Single Vs Stereo Camera Measurement Uncertainty	69
Table 43: Test results [52]	84
Table 44: Estimated Values and their uncertainty	100
Table 45: True and Uncertainty Values of Gyroscope	114

LIST OF FIGURES

Figure	Page
Figure 1: Helicopter Hub [1].....	3
Figure 2: Pitch Link connected to pitch horn and blade grip.....	4
Figure 3: Illustration of forward, hover, and reward flight [2]	6
Figure 4: Fully Articulated Rotor System [5]	7
Figure 5: Blade Pitch Angle [5]	8
Figure 6: Dissymmetry of Lift Diagram [6]	9
Figure 7: Lead-lag positions of blade [7].....	11
Figure 8: CAD Model of mounted sensors	13
Figure 9: Mounted Machined Angle Indicator Plate	15
Figure 10: Linear fit model blade 1	19
Figure 11: Linear fit model blade 2	19
Figure 12: Linear fit model blade 3	20
Figure 13: Figure 13: Linear fit model blade 4.....	20
Figure 14: Pitch Calibration Angle Vs Linear Residual Error.....	24
Figure 15: Pitch Calibration Angle Vs Quartic Residual Error	27
Figure 16: Linear fit model blade 1	30
Figure 17: Linear fit model blade 2	30
Figure 18: Linear fit model blade 3	31
Figure 19: Linear fit model blade 4	31
Figure 20: Flap Calibration Angle Vs Linear Residual Error.....	35
Figure 21: Flap Calibration Angle Vs Polynomial Residual Error.....	37
Figure 22: Linear fit model blade 1	40
Figure 23: Linear fit model blade 2	40
Figure 24: Linear fit model blade 3	41
Figure 25: Linear fit model blade 4	41
Figure 26: Lead-Lag Calibration Angle Vs Linear Residual Error	45
Figure 27: Lead-Lag Calibration Angle Vs Linear Residual Error	47
Figure 28: Schematic of Laser Tracker [16]	52
Figure 29: Cat Eye and SMR Reflectors [18].....	53
Figure 30: Constructive and Destructive Waves [22].....	55
Figure 31: Basic depiction of Michelson Interferometer [23]	56
Figure 32: Laser Tracker Components [26].....	58
Figure 33: Laser projection on target [27]	59
Figure 34: Stereo Camera Triangulation.....	64
Figure 35: Photogrammetry pattern target [32]	65
Figure 36: Experimental Test System [35]	67
Figure 37: Single camera setup (left) and dual camera setup (right) [27]	68

Figure	Page
Figure 38: Plot of errors [27]	69
Figure 39: Coordinate Measurement Arm in use [37]	71
Figure 40: Mounting styles of CMA [38]	72
Figure 41: CMA calibration plate [40]	73
Figure 42: Accuracy and Repeatability Measurement Spread [41]	75
Figure 43: Invar buttons [41]	76
Figure 44: Representation of RLG [46]	78
Figure 45: Representation of FOG [48]	79
Figure 46: Representation of MEMS Gyroscope [50]	80
Figure 47: Sensor position on Wind Turbine [51]	82
Figure 48: Test stand [52]	83
Figure 49: Hub coordinate system defined by laser tracker	88
Figure 50: Defined coordinate system of laser tracker and target	89
Figure 51: Rotation visual from local to world coordinate system.....	89
Figure 52: 3D point in space	91
Figure 53: Representation of conversion from meters to degrees	93
Figure 54: Graph representing laser tracker uncertainty driving factor.....	94
Figure 55: Optotrak with respect to hub and world coordinate system	95
Figure 56: Representation of World Vs Camera Coordinate System [60]	96
Figure 57: Uncertainty trend of Optotrak Certus	102
Figure 58: Distance between two 3D points	103
Figure 59: Distance Uncertainty Trend.....	105
Figure 60: Cosine method to determine angle between 2 vectors	106
Figure 61: Angle Uncertainty Trend.....	107
Figure 62: Total Uncertainty of Faro Arm Trend	108
Figure 63: Modeling Gyroscope to Determine Uncertainty	110
Figure 64: Projection of Gyroscope onto XY-plane	111
Figure 65: Gyroscope Uncertainty over time.....	115
Figure 66: Direct Monte Carlo Method Flowchart [55]	117
Figure 67: Gyroscope uncertainty over time	119

CHAPTER 1

INTRODUCTION AND BACKGROUND

Rotorcraft vehicles are a complex and dynamic means of transportation. Being complex, it is vital that the aerodynamic characteristics of the vehicle are well understood to ensure safe and efficient flight. More importantly, knowing rotor blades' positions throughout flight is crucial since they are responsible for generating the necessary lift needed for flight. Not only do these blades provide lift, they provide flight control aiding in the pitching, rolling, and lateral movement of the aircraft. To better understand these properties, precise measurement systems must be implemented. Therefore, a series of sensors are used to determine the blade pitch, blade lag angle, and the blade flap angle during flight. Given the importance of these blade positions, these sensors need proper calibration.

1.1 PROBLEM STATEMENT

Currently, the calibration method used for rotor hubs at NASA Langley contains inconsistencies in the provided sensor data that may contribute to larger errors than the specified allowed tolerances. These large errors negatively affect the computational fluid dynamic models that simulate the flight characteristics of the helicopter rotor assembly since the calibration data is used to build these models. In order to address this problem, I was hired on as an intern to evaluate the system and come up with a solution to mitigate these errors. Upon further investigation I discovered that not only is the current calibration method potentially causing undesirable uncertainty, it also takes an average of 3 hours per blade to calibrate the pitch, flap, and lead-lag sensors. This equates to a total average calibration time of 12 hours over multiple

days per hub resulting in higher operation costs. Since the calibration time is long, if any problems occur related to these sensors during hub use, all tests must be stopped and another daunting calibration must take place. This characteristic of the system is undesirable since blade analysis usually takes place in expensive wind tunnels that charge an occupancy rate whether or not the system is operating.

1.2 OBJECTIVES

Given the problems associated with the current calibration process, the objective of this thesis is to determine a new calibration method that satisfies the following criteria:

- Shorten calibration time
- Increase calibration accuracy (± 0.1 degree tolerance)
- Simplify the calibration process

1.3 ROTORCRAFT BACKGROUND

1.3.1 Hub Assembly Components

A rotary-wing aircraft is a type of aircraft that relies on lift and thrust to propel it through the air, but different from a traditional fixed wing, tractor propeller aircraft that uses a set of lifting surfaces fixed to the fuselage. The main difference between the two is that the conventional aircraft relies on the wings to produce lift and a fixed set of propellers to produce the thrust, while the rotorcraft generates thrust and lift using a only a set of rotating blades. Generally, the power plant drive shaft angular velocity of the rotorcraft is held constant and the

movement of the blades determines the amount of lift force generated, therefore blade position is crucial when controlling a rotorcraft. All of the input flight controls are relayed through the main hub assembly of the rotorcraft using a series of push rods seen in Figure 1.

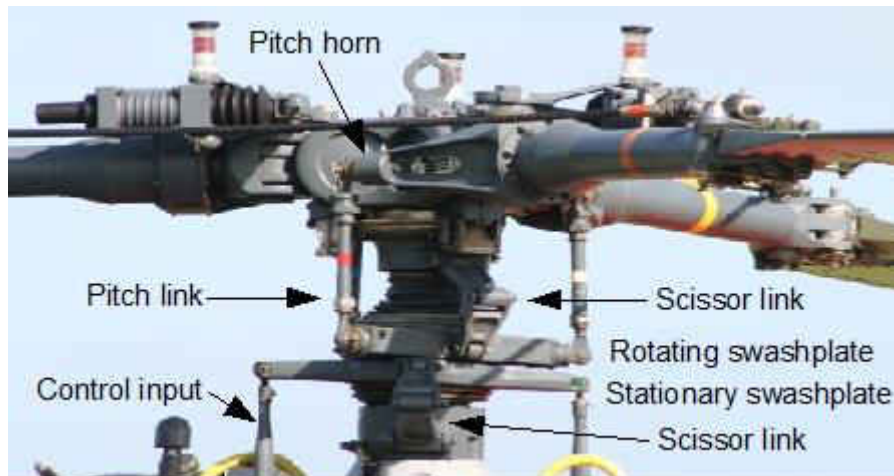


Figure 1: Helicopter Hub [1]

Push rods mounted to the swashplate translate the control inputs from the pilot to the blades. The swash plate is made up of two sections: an upper plate that rotates with the blades and a lower plate that stays stationary with the fuselage. The lower section of the swash plate is connected to the fuselage using a scissor link. This link is mounted to the lower section of the swash plate using a pin joint and is then attached to the fuselage using a ball joint. In between the ball joint and the pin joint is a hinge that allows for vertical movement of the plate. The purpose of the ball joint is to allow for the tilting motion of the plate when desired blade angles are required. The upper plate is mounted in a similar fashion using a second scissor link that is fixed

to the rotor mast. Since it is fixed to the rotor mast, it allows the upper plate to stay in sync with the angular velocity of the blades. Again, the scissor link used for the upper plate is comprised of pin joints, hinges, and ball joints to allow for full articulation of the plate. Attached to the upper swashplate are the pitch links that are also connected to the pitch horn seen in Figure 2.



Figure 2: Pitch Link connected to pitch horn and blade grip

Figure 2 depicts three major components of the hub assembly: the pitch link (yellow), the pitch horn (blue), and the blade grip (green). The lower half of the pitch link is connected to the upper swashplate while the upper half of the pitch link is connected to the pitch horn. The purpose of the pitch link is to translate the swashplate motion to the pitch horn. The pitch horn is an offset lever that is mounted to the blade grip responsible for translating the pitch link motion

to the blade. As the pitch horn moves up and down, the blade will pitch in either the positive or negative direction. The blade grip holds the blade in place via a series of bolts to ensure the blade stays attached to the hub during flight.

All of these components work together to determine flight path and speed of the rotorcraft. To better understand how the components within the system work together, a brief and simplified flight simulation will be explained. The rotorcraft starts on the take-off pad with the engines set at the optimal speed for the particular aircraft. As mentioned earlier, the engine speed will typically remain the same during flight, meaning the blade angles will control aircraft motion. When the aircraft is ready to take-off, the pilot sends controls to the hub assembly via the control links. To produce lift for the aircraft to begin flying, the blade pitch must be changed, which is done by moving the swashplate equally in the vertical direction – called collective. By applying an equal vertical motion to the swash plate, all of the pitch links move simultaneously, thus pitching each blade the same amount. The pitching motion of the blade generates the lift needed for the aircraft to rise. Once the aircraft is hovering above land the next step is to propel the aircraft in the forward direction, which is done by applying a tilting motion to the swash plate – cyclic control. When the hub assembly is tilted in the forward direction the blades produce forward thrust, which propels the aircraft forward. Likewise, when the hub assembly is tilted rearward the blades produce rearward thrust which propels the aircraft backwards (Figure 3).

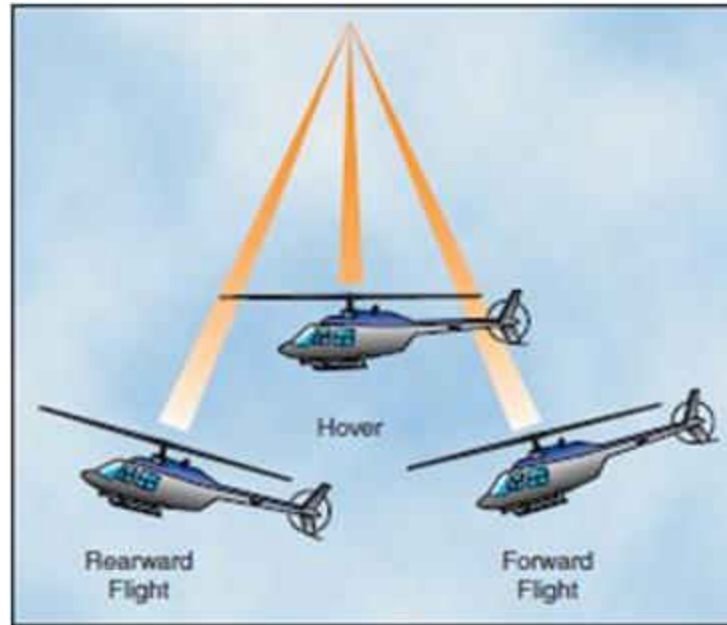


Figure 3: Illustration of forward, hover, and rearward flight [2]

1.3.2 Blade Position During Flight

There are three types of rotor systems seen on rotorcraft: a rigid rotor, a semi-rigid rotor, and a fully articulated rotor [3]. The rigid rotor system is a design that rigidly attaches the blade roots to the rotor hub without any type of hinges that allow for flapping or lagging of blades. Therefore, elastomeric bearings are used to allow for these motions of blades during flight to prevent damage to the blades [3]. The next type of system used is the semi-rigid design, which is attached to the rotor hub using one set of hinges that allows for blade flap. This system is generally used on a two blade rotor setup that allows the blades to have a “teetering” effect to reduce the stress within the blades during flight [4]. The last system, most commonly used with a three or more blade setup, is the fully articulated rotor. This design consists of two sets of hinges per blade allowing the blades to flap, lag, and pitch independently from each other (Figure 4).

This system proves to be superior in reducing stresses on the blades as well as increasing flight control [4].

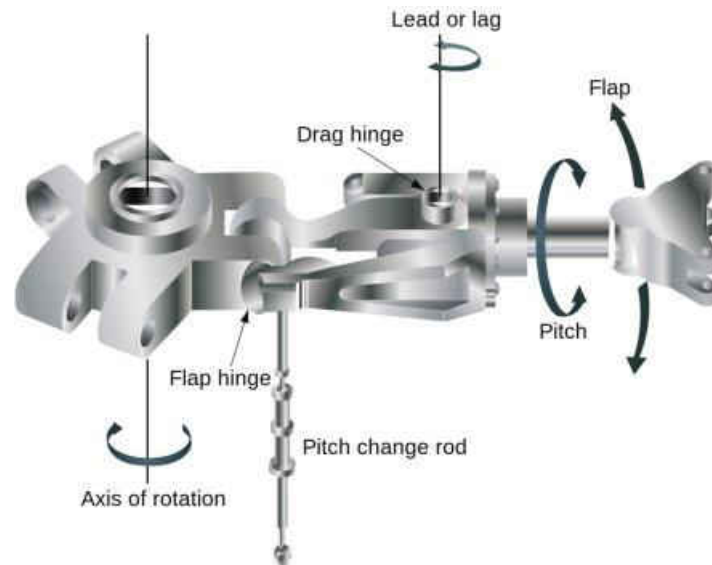


Figure 4: Fully Articulated Rotor System [5]

1.3.2.1 Pitch

The rotational movement of the blade about its feathering axis is commonly referred to as blade pitch. The pitching of the blade is directly related to the angle between the chord line of the blade and the rotational plane of the blades seen in Figure 5 [5].

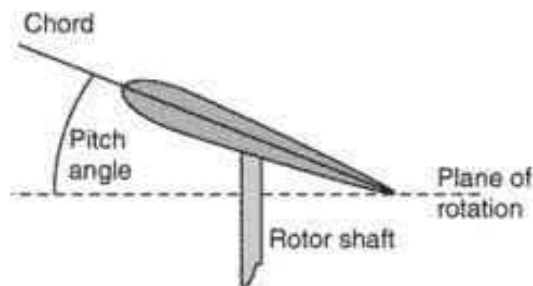


Figure 5: Blade Pitch Angle [5]

The blade pitch is responsible for determining the amount of lift generated by the blades during flight. Given the wing-like structures of the blades, as air flows over the blades the airspeed is faster on top and slower on the bottom. This difference in airspeed over the blades causes a difference in pressure, with the top of the airfoil being the lowest due to its higher velocity [5]. This difference in pressure results in a lifting force. This lifting force can then be manipulated through the pitch control of the rotor blades. To generate more lift, the pitch angle is increased also resulting in a greater drag force on the blades. Consequently, when the pitch angle of the blade is decreased, the drag on the blade is decreased as well.

1.3.2.2 Flap

The vertical movement of the blade as it follows the azimuth during blade rotation is known as blade flap. This motion of the blade is used to compensate for the dissymmetry of lift the helicopter experiences during flight. Dissymmetry of lift is the theory that the lifting forces on the left and right side of the helicopter are not equal during forward flight, therefore this imbalance would cause the aircraft to constantly want to roll. The difference in the lift is

modeled by splitting the rotors into two sides: the advancing half and the retreating half (Figure 6).

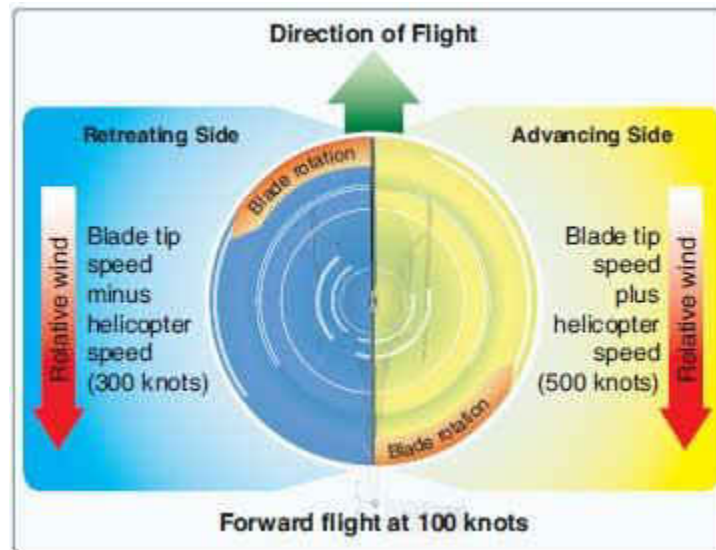


Figure 6: Dissymmetry of Lift Diagram [6]

As the helicopter begins to move through the air, the relative airflow across the advancing and retreating half begin to differ. During forward flight the advancing half of the rotors experience an increase in airspeed since the rotors are moving against the flow of the oncoming air. Consequently, the retreating half of the rotors experience a decrease in airspeed since the rotors are moving with the flow of the oncoming air. Given the nature of lifting properties of airfoils having more lift as the speed increases, the amount of lift generated on the advancing side of the rotors is greater than then retreating half. This imbalance in lifting force must be compensated for to prevent instabilities during flight. This is done by allowing the blades to flap during flight by implementing a horizontal hinge on the hub. This hinge enables

the blades to move freely in the vertical direction, thus changing the pitch of the blades as they rotate about the azimuth. Since the advancing half of the rotors experience more lift, the blades are forced in an upward direction with the highest position being at the 3 O'clock position as viewed from above. By flapping the blades upwards, the blade pitch is reduced, thus generating less lift when compared to a rigid system. Adversely, since the retreating half of the blades experience less lift the blade is in a more downward position compared to the advancing half, with the lowest position being at the 9 O'clock position. This downward position increases the angle of attack of the blades, thus generating more lift. Therefore, the act of flapping the blades creates an overall balance of lift among the rotors which prevents a constant rolling motion in the aircraft.

1.3.2.3 Lead-Lag

The horizontal movement of the blade as it follows the azimuth during blade rotation is known as blade lead-lag. When the blade is in the leading position, the blade position is advanced with respect to its center line. Adversely, when the blade is lagging the blade position is retarded with respect to its center line (Figure 7).

Lead-Lag Motion is least Damped and Often requires Dampers

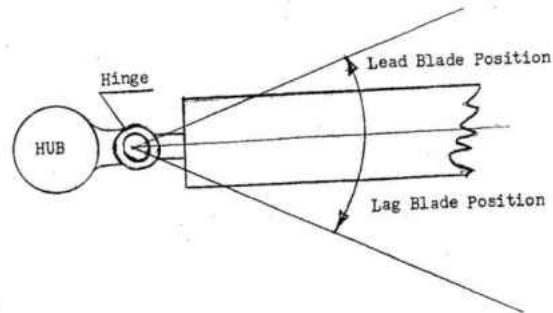


Figure 7: Lead-lag positions of blade [7]

These motions of the blades are used to compensate for the Coriolis Effect the helicopter blades experience during flight. The Coriolis Effect is the phenomena that an object's rotational speed increases or decreases as its center of gravity moves closer or further away from its rotational axis [8]. This effect is caused by the flapping motion of the blades during flight. Therefore, as the blade flaps up the center of gravity of the blade moves closer to the rotational axis. This movement causes the blades rotational speed to increase, thus placing the blade in the leading position. Consequently, as the blade flaps down the center of gravity moves further from the rotational axis. Since the center of gravity is further from the rotational axis the blade slows down, putting it in the lagging position. Due to the blades being able to lead and lag, vibrations and blade stress is significantly reduced [9].

CHAPTER 2

CURRENT SYSTEM

Currently, there are a total of 5 sensors measuring the pitch, flap, and lead-lag position of the blades during flight. The flap and lead-lag position are each measured with a single-turn inductive potentiometer manufactured by P3 America. The flap and lead-lag angle is measured by placing a potentiometer on the center line of the flap pin and lead-lag pin. As the blade pivots, the potentiometer stud spins about its axis, changing resistance which in turn allows a bridge circuit to create a varying voltage that can be related to angles using a calibration equation. The pitch angle is currently being measured using a series of three Honeywell SS496A1 sensors mounted to an offset bracket that cradles the cuff link. Attached to the cuff link is a custom polarized magnet that generates magnetic forces as the magnet passes the series of Honeywell sensors. These magnetic forces are then transformed into degrees using the provided sensor calibration equation. All of these sensors can be seen via a CAD model in Figure 8 below.

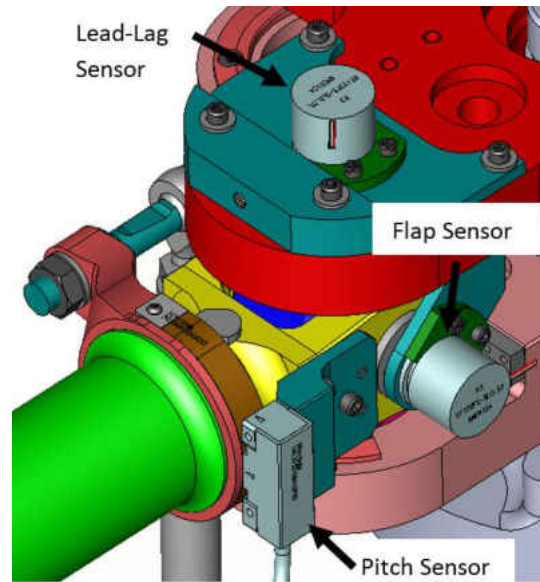


Figure 8: CAD Model of mounted sensors

2.1 Current Calibration Process

The current calibration process begins by leveling the swashplate of the hub so that each blade can be properly zeroed. This process is done by placing an inclinometer on the four quadrants of the swash plate and making micro adjustments on the swashplate pitch and roll pushrods until the rotating plane is level. Once the plane is level, the first degree of freedom calibrated is the rotor's motion of pitch. This process begins by ensuring the lead-lag and the flap of the blade is set to the zero reference which is achieved by aligning two centering marks: one on the cuff link and the other on the hub itself. Once the lead-lag is set the focus is shifted towards zeroing out the flap position of the blade. This is done by pitching the blade until it is relatively level and then the inclinometer is placed on the blade in a parallel configuration. The calibrator then progressively raises the blade until the inclinometer reads zero. A shim is then placed between the hub and the physical stop on the flap hinge to ensure the blade does not move

from its current flap position. Once the flap and lead-lag positions are set, the inclinometer is placed on the rotor perpendicularly to measure the pitch angle. The blade is then pitched by a defined angle generated using statistical software with built in redundancies to ensure the full range of motion is captured. Once the blade reaches the specified pitch angle the sensor voltage is recorded and the blade is then moved to a new angle. This process continues until all data points are successfully recorded. After completing the pitch sensor calibration, the flap sensor is the next sensor to be calibrated.

The process of calibrating the flap sensor begins by zeroing out the pitch and lead-lag position of the blade. The lead-lag position should still be zeroed from the pitch calibration, however, it is still verified to ensure the blade has not moved. Once the lead-lag position is verified, the blade pitch is adjusted back to zero. This is verified again by placing the inclinometer on the blade perpendicularly and ensuring it reads zero degrees. The blade is then supported by a small scissor jack that will be adjusted incrementally until the desired flap position is reached. To ensure the jack remains level and makes full contact with the blade at all times, a ball bearing is placed at the base of the scissor jack. This technique allows the scissor jack to rotate with the blade as it moves vertically about its range of motion. After the scissor jack is placed the shims are removed from the blade stop and the inclinometer is placed parallel on top of the blade. A series of blade positions are then presented and the blade is moved to each position using the scissor jack. Once the blade reaches the desired flap angle, the sensor output voltage is recorded and the calibrator adjusts the blade to the next position. This process continues until all the data points are taken and successfully recorded. After calibrating the flap sensor, the final part of the blade calibration is focused on the lead-lag sensor.

The lead-lag sensor is the final sensor that is calibrated during the process using a different calibration device. As mentioned earlier, the pitch and flap sensors are calibrated using an inclinometer, but the lead-lag sensor is calibrated using a machined angle indicator plate as seen in Figure 9.

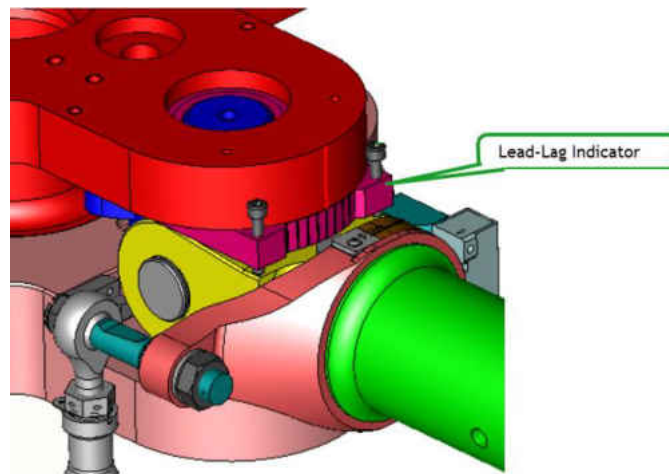


Figure 9: Mounted Machined Angle Indicator Plate

This plate consists of ten marks ranging from negative five degrees to positive five degrees along the contour of the hub. This mounted plate allows the operator to align the mark on the rotor cuff link with the desired angle on the angle indicator plate. Before this method of calibration is performed, the flap angle is shimmed back to its zero position and the pitch angle is toggled back to its zero position. After both flap and pitch are at zero, the calibrator proceeds to incrementally adjust the lead-lag position of the blade. This process is done by having the calibrator align the mark on the rotor cuff link with the specified lead-lag calibration angle by eye. Once the calibrator has determined the rotor is in proper position the sensor voltage output is recorded and

the calibrator moves onto the next data point. This process is continued until all calibration points are successfully recorded.

Once the pitch, flap, and lead-lag sensors are calibrated, the recorded sensor output values are then compiled and a calibration equation is generated. This calibration equation translates the sensor voltage output to an angle output with a desired tolerance of ± 0.1 degrees. However, due to the nature of the calibration process for the lead-lag sensor it was decided that further investigation of the current blade angle measurements should be done given the desired tolerance specification.

2.2 Data Analysis of Blade Calibration

Since the current calibration method relies on the human eye to establish blade position with an acceptance tolerance of ± 0.1 degrees, it is of concern that this method is not capable of meeting the overall accuracy. Therefore, it was justified that an analysis should be conducted focusing on the associated error with each blade sensor. This analysis involves applying a first order calibration math model, converting blade angle predictions to degrees for interpretation, determining any nonlinear characteristics, and subsequently increasing model order to account for any non-linear behavior in order to reduce any residual errors.

2.2.1 Blade Pitch

Currently, the blade pitch angle is measured with an angle indicator, accurate out to a hundredth of a degree. Given this information it could be assumed that the calibration accuracy

should fall within the desired tolerance of ± 0.1 degrees, however, upon further investigation this assumption is not valid. Each of the four blades were analyzed individually and then compared at the end of the analysis. Each blade also goes through a randomized series of calibration angles generated by a statistical program. At each data point provided, a nominal voltage is produced by each sensor and this is then converted to the associated blade angle using a calibration equation. The sensors being used are linear sensors, therefore a linear fit model was the first model used to analyze the system. The run order and associated output angles can be seen in Table 1.

BLADE	CALIBRATION ANGLE	PREDICTED 1st Order Model
1	-5	-5.138
1	0	-0.117
1	10	10.187
1	20	19.981
1	30	29.688
1	20	20.254
1	10	10.157
1	0	0.034
1	-5	-5.047
2	-5	-5.203
2	0	-0.028
2	10	10.392
2	20	20.096
2	30	29.420
2	20	20.264
2	10	10.352
2	0	-0.106
2	-5	-5.187
3	0	-0.191
3	10	10.128
3	20	20.151
3	30	29.515
3	20	20.306
3	10	10.283
3	0	-0.022
3	-4.3	-4.471
4	0	0.080
4	10	10.135
4	20	19.887
4	30	30.047
4	20	19.924
4	10	10.063
4	0	-0.064
4	-3.9	-3.974

Table 1: Blade Pitch Sensor Run Order

Using Ordinary Least Squares regression [10], a first order model is fit using sensor output voltage as the dependent variable and blade angle as the independent variable in the calibration model seen in Figure 10 through 13.

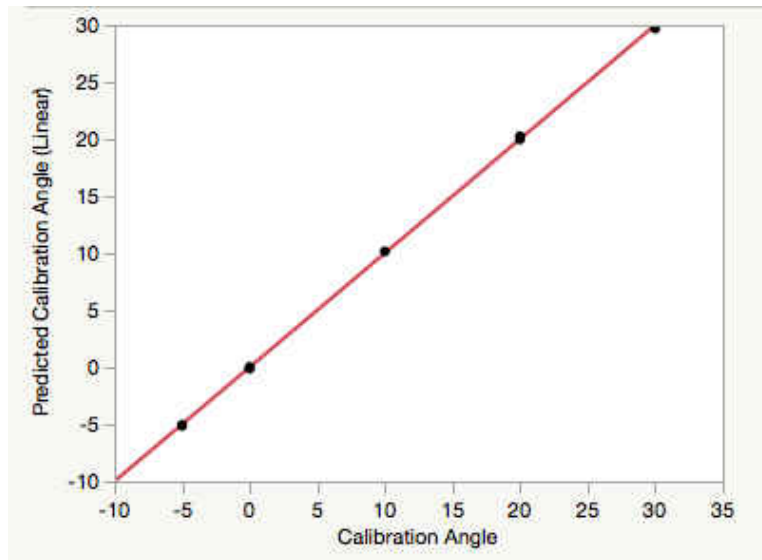


Figure 10: Linear fit model blade 1

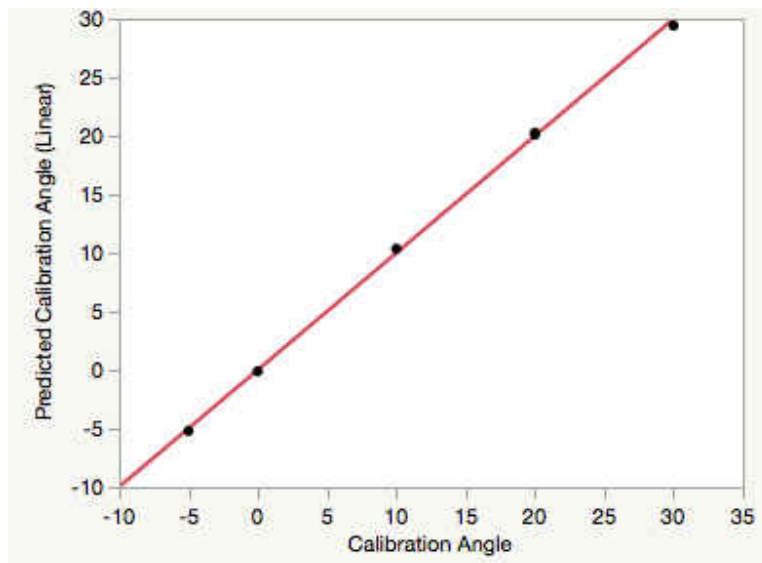


Figure 11: Linear fit model blade 2

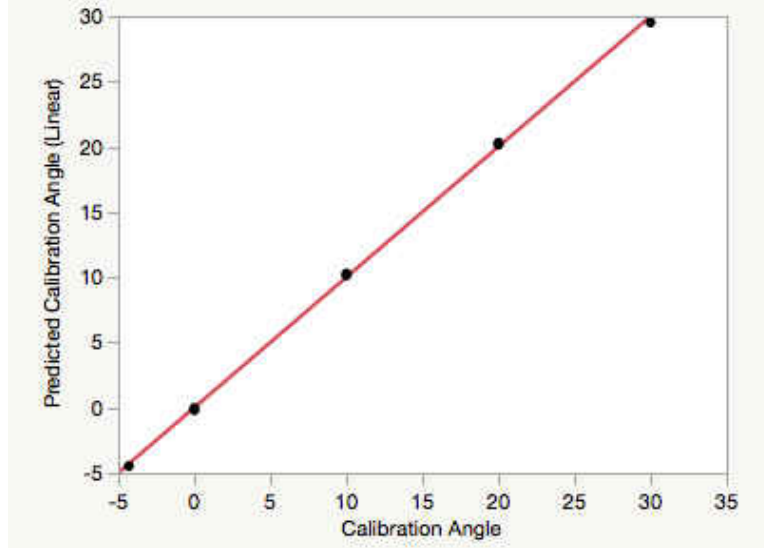


Figure 12: Linear fit model blade 3

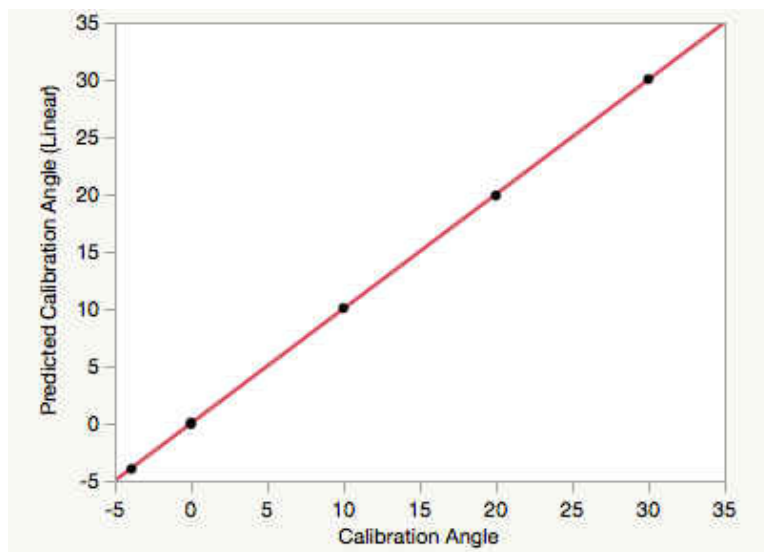


Figure 13: Figure 13: Linear fit model blade 4

The ANOVA tables for the blade pitch sensors with a linear fit applied are then evaluated and seen in Table 2 through 5. These tables are used to determine significant terms within the generated models. After reviewing the associated ANOVA tables, it was found that all of the

terms had an alpha value of less than 0.05 meaning that all the terms are deemed to be significant.

Analysis of Variance				
Source	DF	Sum of Squares	Mean Square	F Ratio
Model	1	1238.3717	1238.37	33526.66
Error	7	0.2586	0.036937	Prob > F
C. Total	8	1238.6303		<.0001*

Table 2: ANOVA table blade 1

Analysis of Variance				
Source	DF	Sum of Squares	Mean Square	F Ratio
Model	1	1237.3255	1237.33	11083.35
Error	7	0.7815	0.11	Prob > F
C. Total	8	1238.1069		<.0001*

Table 3: ANOVA table blade 2

Analysis of Variance				
Source	DF	Sum of Squares	Mean Square	F Ratio
Model	1	999.39853	999.399	11643.98
Error	6	0.51498	0.086	Prob > F
C. Total	7	999.91351		<.0001*

Table 4: ANOVA table blade 3

Analysis of Variance				
Source	DF	Sum of Squares	Mean Square	F Ratio
Model	1	988.44038	988.440	100207.4
Error	6	0.05918	0.009864	Prob > F
C. Total	7	988.49956		<.0001*

Table 5: ANOVA table blade 4

After determining that all of the parameters are significant, the models were then evaluated to determine if the lack of fit was significant or not. The lack of fit model utilizes the F-test which compares the two variances, s_1 and s_2 , to determine if they are equal [10]. Upon further analysis of the pitch sensors in blades 1 through 4, it was found that blades 1 and 4 were insignificant while blades 2 and 3 were significant as seen in table 6 through 9.

Lack Of Fit				
Source	DF	Sum of Squares	Mean Square	F Ratio
Lack Of Fit	3	0.20496167	0.068321	5.0989
Pure Error	4	0.05359682	0.013399	Prob > F
Total Error	7	0.25855849		0.0748
				Max RSq
				1.0000

Table 6: Lack of Fit table blade 1

Lack Of Fit				
Source	DF	Sum of Squares	Mean Square	F Ratio
Lack Of Fit	3	0.76349880	0.254500	56.6547
Pure Error	4	0.01796846	0.004492	Prob > F
Total Error	7	0.78146725		0.0010*
				Max RSq
				1.0000

Table 7: Lack of Fit table blade 2

Lack Of Fit				
Source	DF	Sum of Squares	Mean Square	F Ratio
Lack Of Fit	3	0.47649783	0.158833	12.3831
Pure Error	3	0.03847981	0.012827	Prob > F
Total Error	6	0.51497765		0.0339*
				Max RSq
				1.0000

Table 8: Lack of Fit table blade 3

Lack Of Fit				
Source	DF	Sum of Squares	Mean Square	F Ratio
Lack Of Fit	3	0.04536017	0.015120	3.2814
Pure Error	3	0.01382350	0.004608	Prob > F
Total Error	6	0.05918368		0.1776
				Max RSq
				1.0000

Table 9: Lack of Fit table blade 4

After determining that there was a significant in lack of fit in blades 2 and 3, it was imperative to evaluate the residual error within the measurements. From JMP statistical software, the residuals are taken and a graph depicting the calibration angle versus the residual error is

created (Figure 14). Residuals are the difference of observed values and calibration model predicted values.

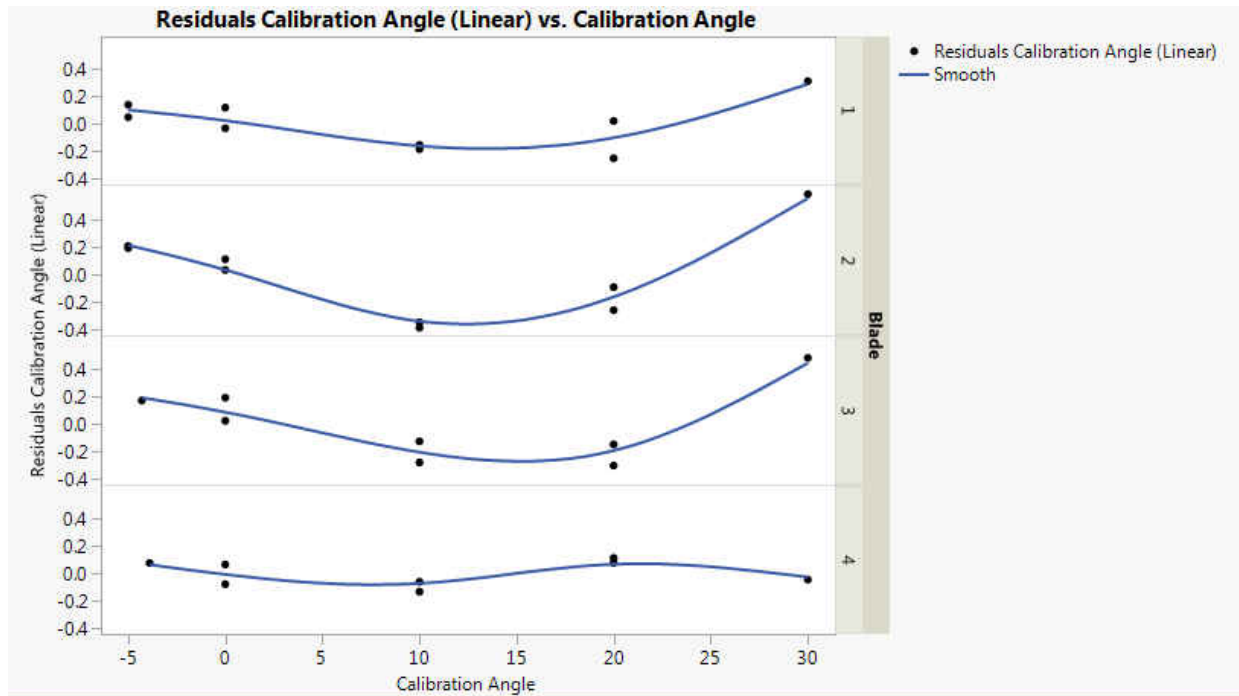


Figure 14: Pitch Calibration Angle Vs Linear Residual Error

Upon further investigation of blade one, it was found that the maximum residual error was 0.31 degrees at the 30 degree calibration angle. This value is already three times larger than the accepted tolerance. It is also important to note that when the calibration angle is repeated, the variance is rather large. For example, at the 20 degree calibration angle blade one reads 19.98 degrees and then reads 20.25 degrees when repositioned. This variance in the data is undesirable since it is nearly triple the accepted tolerance range. Another major influence to the non-linear behavior of the calibration data is the 30 degree calibration angle. This calibration point skews the data tremendously by increasing the variance from roughly ± 0.2 degrees to ± 0.4 degrees.

This trend of data spread and large variance continues through blades one through three with blade two having the largest residual error of 0.57 degrees. However, blade four was determined to have an insignificant lack of fit with very little variance in the repeated calibration angles. For example, when comparing the 20 degree calibration to blade one it was found that blade one had a variance of approximately 0.27 degrees whereas blade four only had a variance of 0.04 degrees. This disparity in the data suggests that the method being used to calibrate blade four could be inconsistent with blades one through three. In order to verify this assumption, the summary of fit tables are evaluated. More specifically, the mean square error is of main focus in determining the spread of the variance between the actual value and the predicted value of the linear model [10]. After reviewing the values seen in table 10 through 13, blades 1 through 3 exceeded 0.1 degrees while blade 4 barely remained under 0.1 degrees given a value of 0.099 degrees.

Summary of Fit	
RSquare	0.999791
RSquare Adj	0.999761
Root Mean Square Error	0.19219
Mean of Response	8.888889
Observations (or Sum Wgts)	9

Table 10: Summary of fit table blade 1

Summary of Fit	
RSquare	0.999369
RSquare Adj	0.999279
Root Mean Square Error	0.334123
Mean of Response	8.888889
Observations (or Sum Wgts)	9

Table 11: Summary of fit table blade 2

Summary of Fit	
RSquare	0.999485
RSquare Adj	0.999399
Root Mean Square Error	0.292967
Mean of Response	10.7125
Observations (or Sum Wgts)	8

Table 12: Summary of fit table blade 3

Summary of Fit	
RSquare	0.99994
RSquare Adj	0.99993
Root Mean Square Error	0.099317
Mean of Response	10.7625
Observations (or Sum Wgts)	8

Table 13: Summary of fit table blade 4

Since there is such a large variance within the calibration of the pitch angles using a linear fit model, a polynomial regression was applied to mitigate some of the residual error (Figure 15).

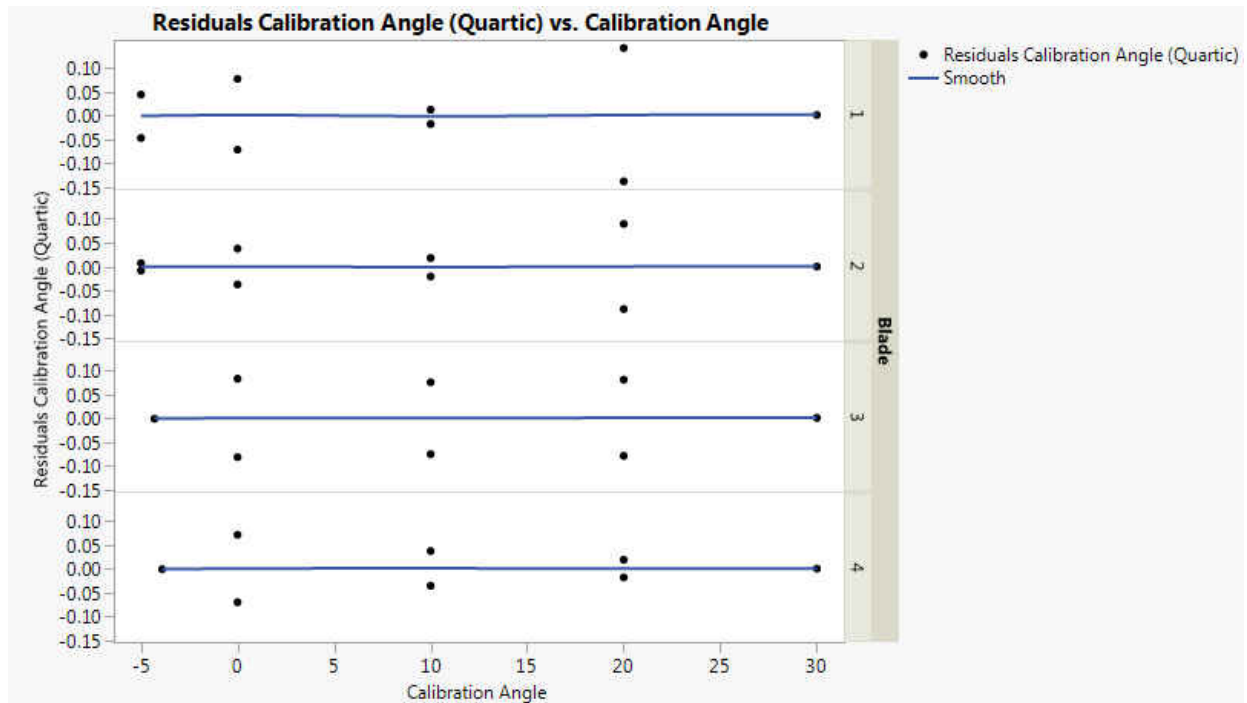


Figure 15: Pitch Calibration Angle Vs Quartic Residual Error

With a quartic fit, the residual error is significantly reduced, and the data is conceptualized as having a more linear form. However, though the residual error has been reduced, there is still the same large variance discrepancy in similar calibration angles when compared to the linear fit model. Focusing on blade one, specifically on the 20 degree calibration angle, there is still a total variance of 0.28 degrees, but the curvature is significantly reduced. This data may suggest that using a quartic fit may be the best way to represent the system, however, with such a large variance between certain data points it is difficult to justify the repeatability of the system. Therefore, the data is suggesting that there may be a problem in the calibration method rather than the sensor itself given the information that blade four was significantly different from blades one through three. Therefore, the flap and lead-lag sensors

need an evaluation to better understand the errors associated within the sensors during the calibration process.

2.2.2 Blade Flap:

The flap sensors are also classified as linear sensors, therefore, a linear fit model is used to analyze the system similarly to the pitch sensor analysis. The run order and associated output angles with this linear fit can be seen in Table 14.

BLADE	CALIBRATION ANGLE (deg)	PREDICTED 1 st Order (deg)
1	-3.1	-3.336
1	-3	-3.163
1	0	0.268
1	6	6.422
1	12	11.961
1	13.9	13.532
1	12	11.838
1	6	6.355
1	0	0.217
1	-3	-3.130
1	-3.1	-3.266
2	-3.6	-3.546
2	-3	-2.920
2	0	0.001
2	6	5.744
2	12	12.050
2	14	14.215
2	12	12.000
2	6	5.746
2	0	0.006
2	-3	-2.949
2	-3.6	-3.548
3	-4.2	-4.207
3	-3	-2.896
3	0	0.097
3	6	5.891
3	12	12.036
3	14	14.186
3	12	11.883
3	6	5.817
3	0	0.047
3	-3	-2.982
3	-4	-4.075
4	-3.9	-4.069
4	-3	-3.010
4	0	0.219
4	6	6.301
4	12	11.936
4	14.6	14.350
4	12	11.875
4	6	6.259
4	0	0.237
4	-3	-3.197
4	-3.9	-4.103

Table 14: Flap Sensor Run Order

The first order models are fit using ordinary least square regression similarly to the pitch sensors and can be seen in Figure 16 through 19.

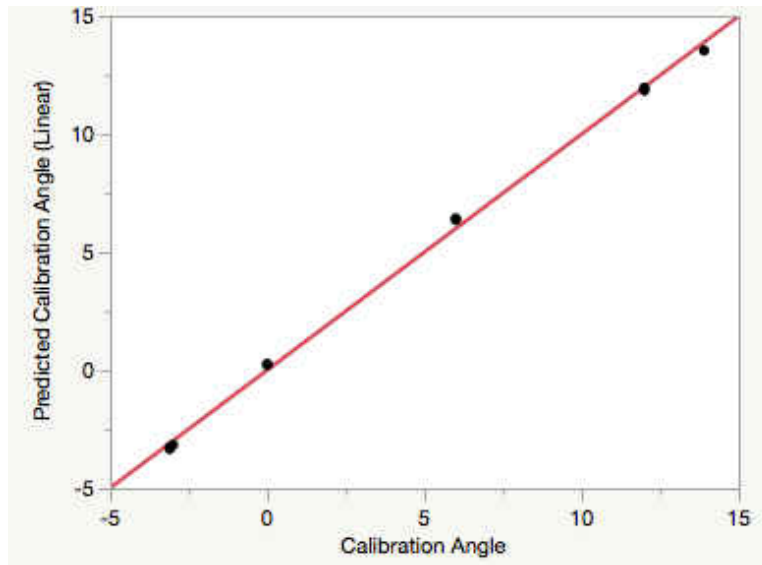


Figure 16: Linear fit model blade 1

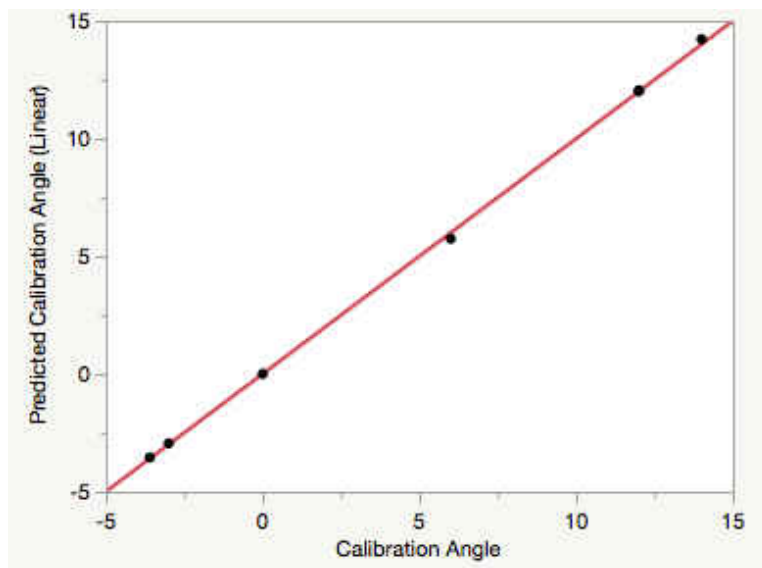


Figure 17: Linear fit model blade 2

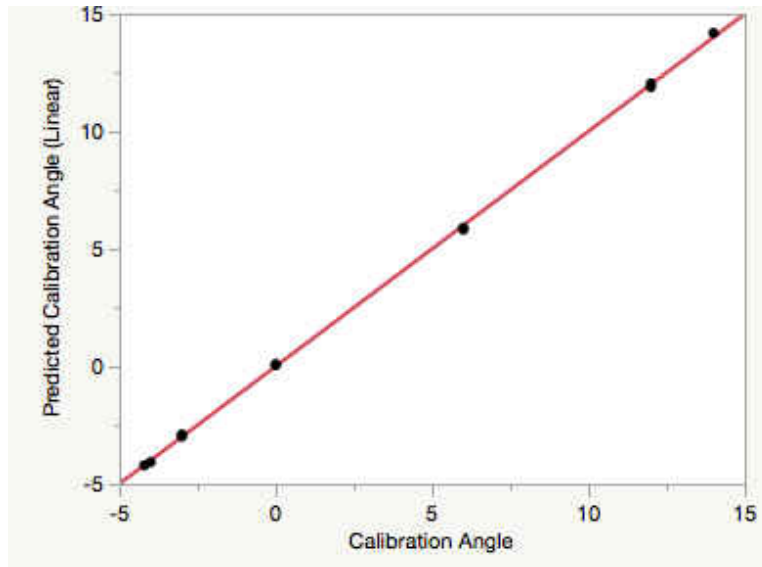


Figure 18: Linear fit model blade 3

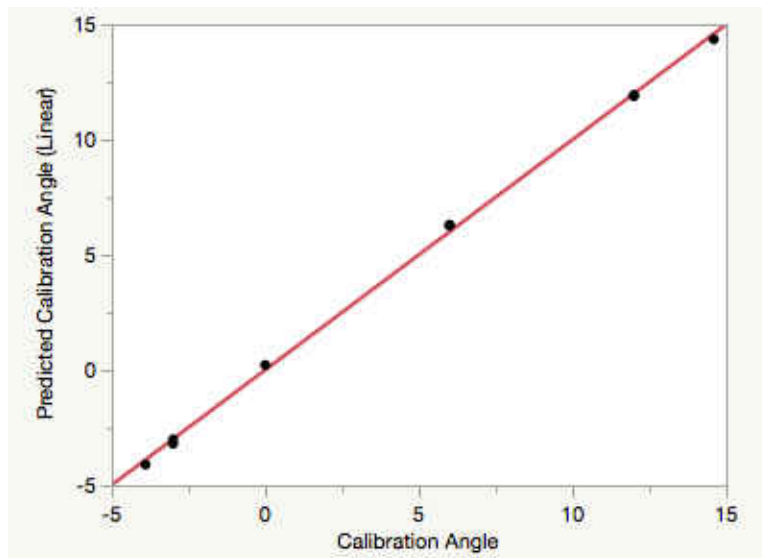


Figure 19: Linear fit model blade 4

The ANOVA tables for the blade pitch sensors with a linear fit applied are then evaluated and seen in Table 15 through 18. After reviewing the tables, it was determined that all of the terms were classified as significant due to an alpha value of less than 0.05.

Analysis of Variance				
Source	DF	Sum of Squares	Mean Square	F Ratio
Model	1	459.79367	459.794	5799.620
Error	9	0.71352	0.079	Prob > F
C. Total	10	460.50719		<.0001*

Table 15: ANOVA table blade 1

Analysis of Variance				
Source	DF	Sum of Squares	Mean Square	F Ratio
Model	1	476.42017	476.420	22157.85
Error	9	0.19351	0.022	Prob > F
C. Total	10	476.61368		<.0001*

Table 16: ANOVA table blade 2

Analysis of Variance				
Source	DF	Sum of Squares	Mean Square	F Ratio
Model	1	490.88095	490.881	35874.86
Error	9	0.12315	0.014	Prob > F
C. Total	10	491.00409		<.0001*

Table 17: ANOVA table blade 3

Analysis of Variance				
Source	DF	Sum of Squares	Mean Square	F Ratio
Model	1	497.55971	497.560	9872.747
Error	9	0.45358	0.050	Prob > F
C. Total	10	498.01328		<.0001*

Table 18: ANOVA table blade 4

After determining that all of the parameters are significant, the models were then evaluated to determine if the lack of fit was significant or not utilizing the F-test again. Upon further analysis of the flap sensors in blades 1 through 4, it was found that the lack of fit for blades 1, 2, and 4 were significant while blade 3 was insignificant as seen in Table 19 through 22.

Lack Of Fit				
Source	DF	Sum of Squares	Mean Square	F Ratio
Lack Of Fit	4	0.69951138	0.174878	62.4192
Pure Error	5	0.01400833	0.002802	Prob > F
Total Error	9	0.71351971		0.0002*
				Max RSq
				1.0000

Table 19: Lack of Fit table blade 1

Lack Of Fit				
Source	DF	Sum of Squares	Mean Square	F Ratio
Lack Of Fit	4	0.19177877	0.047945	138.4134
Pure Error	5	0.00173194	0.000346	Prob > F
Total Error	9	0.19351070		<.0001*
				Max RSq
				1.0000

Table 20: Lack of Fit table blade 2

Lack Of Fit				
Source	DF	Sum of Squares	Mean Square	F Ratio
Lack Of Fit	5	0.10377963	0.020756	4.2865
Pure Error	4	0.01936869	0.004842	Prob > F
Total Error	9	0.12314832		0.0917
				Max RSq
				1.0000

Table 21: Lack of Fit table blade 3

Lack Of Fit				
Source	DF	Sum of Squares	Mean Square	F Ratio
Lack Of Fit	4	0.43249525	0.108124	25.6456
Pure Error	5	0.02108038	0.004216	Prob > F
Total Error	9	0.45357563		0.0016*
				Max RSq
				1.0000

Table 22: Lack of Fit table blade 4

After determining that there was a significance in lack of fit in blades 1, 2, and 4, it was imperative to evaluate the residual error within the measurements. From JMP statistical software, the residuals are taken and a graph depicting the calibration angle versus the residual error is created seen in Figure 20.

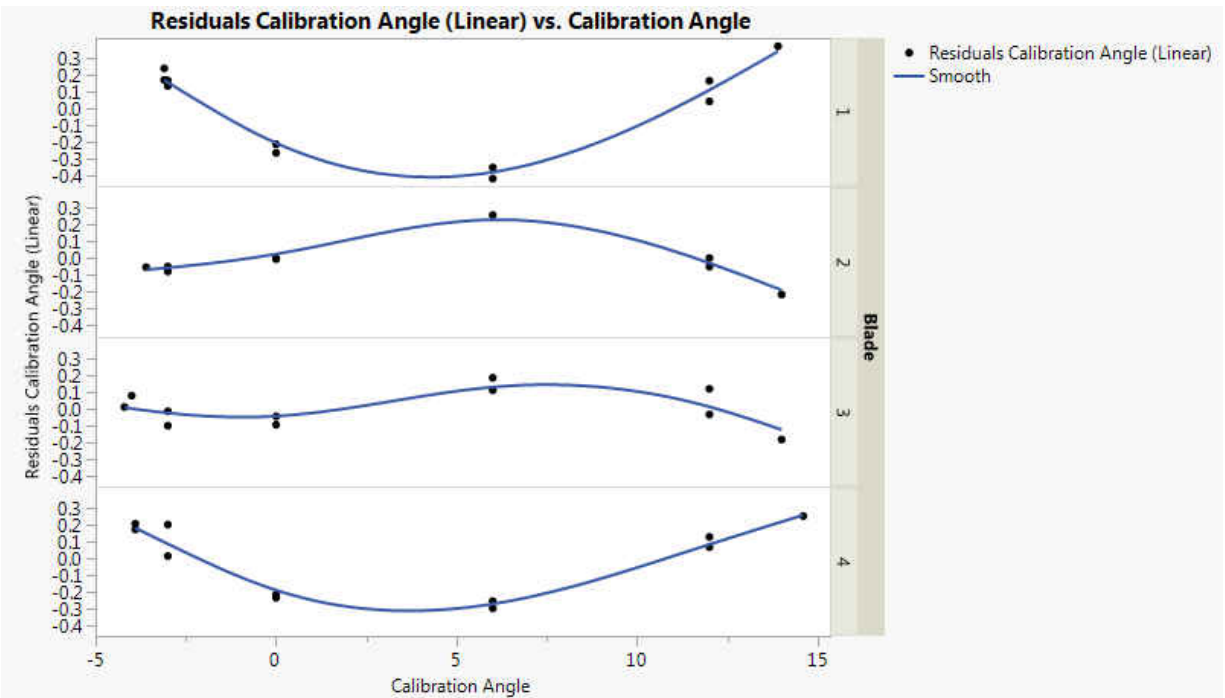


Figure 20: Flap Calibration Angle Vs Linear Residual Error

Focusing on blades 1 and 4, it is seen that there is a relatively large error beginning from the 0 degree calibration angle to the 6 degree calibration angle. Blade one has an error as large as 0.42 degrees in the negative direction, which is four times larger than the accepted 0.1 degree tolerance. Even though the variance between the data points is much smaller, each blade does not follow a similar trend. For example, blades one and four have a significant amount of error from 0 to 6 degrees in the negative direction whereas blade two has a significant amount of error at 6 degrees in the positive direction. Also, when compared to the pitch sensors, the troubled blade has shifted from blade four to blade three again suggesting that the current calibration process could be flawed. Again, these large variances were realized by evaluating the summary of fit tables seen in Table 23 through 26.

Summary of Fit	
RSquare	0.998451
RSquare Adj	0.998278
Root Mean Square Error	0.281567
Mean of Response	3.427273
Observations (or Sum Wgts)	11

Table 23: Summary of fit table blade 1

Summary of Fit	
RSquare	0.999594
RSquare Adj	0.999549
Root Mean Square Error	0.146633
Mean of Response	3.345455
Observations (or Sum Wgts)	11

Table 24: Summary of fit table blade 2

Summary of Fit	
RSquare	0.999749
RSquare Adj	0.999721
Root Mean Square Error	0.116975
Mean of Response	3.254545
Observations (or Sum Wgts)	11

Table 25: Summary of fit table blade 3

Summary of Fit	
RSquare	0.999089
RSquare Adj	0.998988
Root Mean Square Error	0.224493
Mean of Response	3.345455
Observations (or Sum Wgts)	11

Table 26: Summary of fit table blade 4

In order to mitigate the residual error for the flap sensors, a polynomial regression of the 5th order was applied (Figure 21).

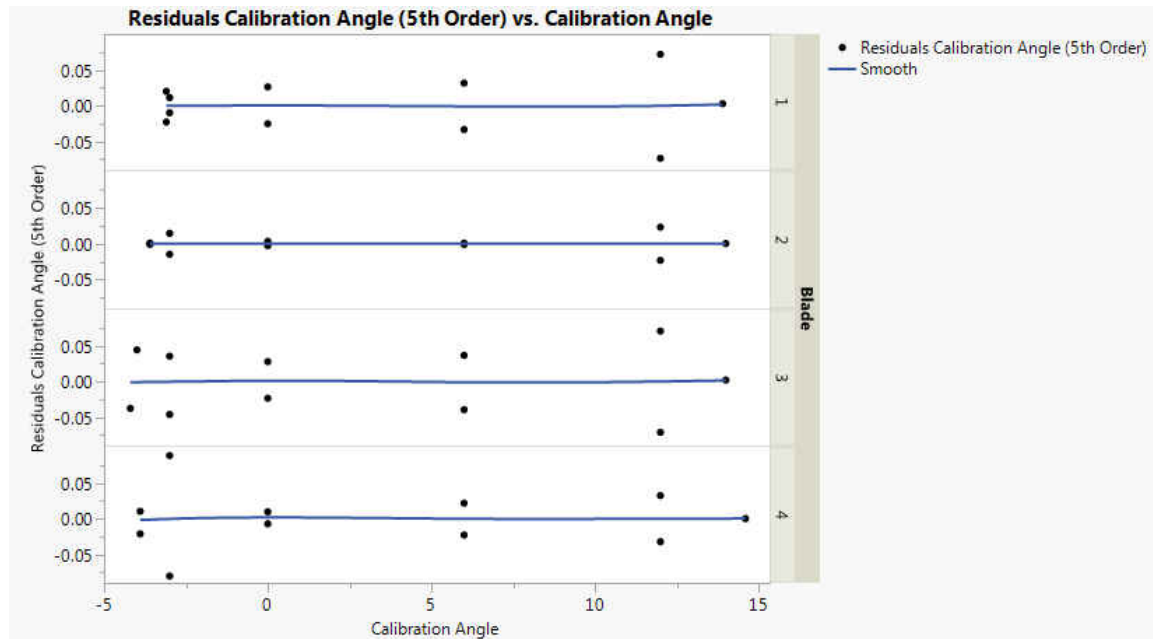


Figure 21: Flap Calibration Angle Vs Polynomial Residual Error

With a polynomial regression applied to the flap sensor data, it is much easier to visualize the variance within the data set. The variance stays within the ± 0.1 degree tolerance for each blade, suggesting that the sensor output would be acceptable for accurate data collection. However, even though the sensor outputs stay within the desired tolerance there is an inconsistency with the variance between each blade. Blades one and three follow a similar pattern of having a large variance at the 12 degree calibration angle while blades two and four share the pattern of having a small variance at the 12 degree calibration angle. Again, this inconsistency would suggest that the method of calibrating the flap sensor could be inconsistent

in terms of placing the blade at the exact location of the first data point since the blades follow a similar trend. Based on the calibration data it can be assumed that the flap sensor calibration is successful, therefore the focus of the analysis is shifted towards the lead-lag sensor.

2.2.3 Blade Lead-Lag

The lead-lag sensors are also classified as linear sensors, therefore, a linear fit model is used to analyze the system similarly to the pitch sensor analysis. The run order and associated output angles with this linear fit can be seen in Table 27.

BLADE	CALIBRATION ANGLE	PREDICTED LINEAR
1	-16	-15.808
1	-8	-8.063
1	-4	-4.134
1	0	-0.162
1	4	4.778
1	0	-0.559
1	-4	-4.243
1	-8	-8.009
1	-16	-15.797
2	-16	-15.779
2	-8	-7.766
2	-4	-4.106
2	0	-0.478
2	5	5.873
2	0	-0.482
2	-4	-4.379
2	-8	-8.064
2	-16	-15.815
3	-16	-15.760
3	-8	-7.698
3	-4	-4.294
3	0	-0.645
3	7	7.972
3	0	-0.670
3	-4	-4.266
3	-8	-7.900
3	-16	-15.737
4	-12	-12.294
4	-8	-7.497
4	-4	-3.492
4	0	-0.096
4	7	7.028
4	0	-0.440
4	-4	-4.137
4	-8	-7.975
4	-12	-12.094

Table 27: Lead-Lag Run Order

The first order models are fit using ordinary least square regression similarly to the pitch and flap sensors and can be seen in Figures 22 through 25.

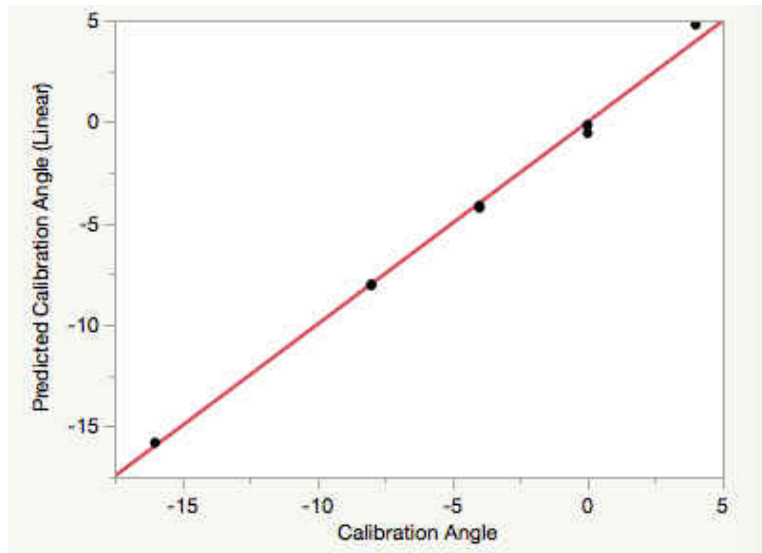


Figure 22: Linear fit model blade 1

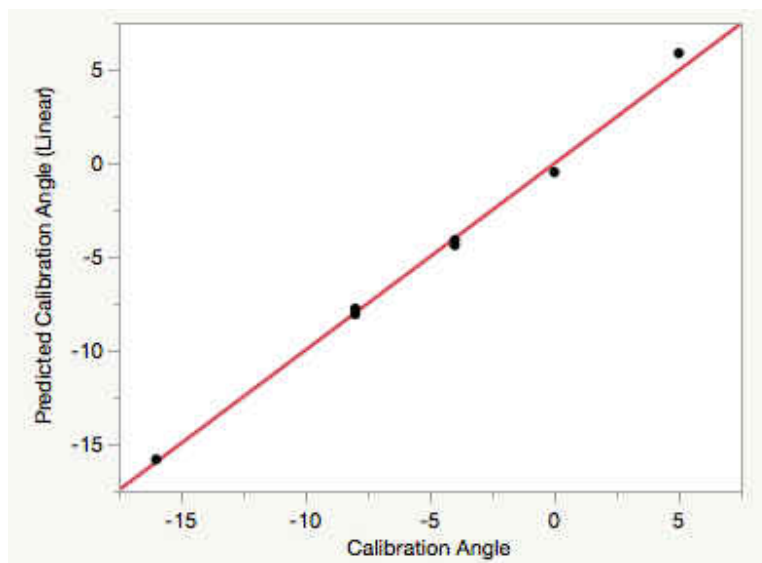


Figure 23: Linear fit model blade 2

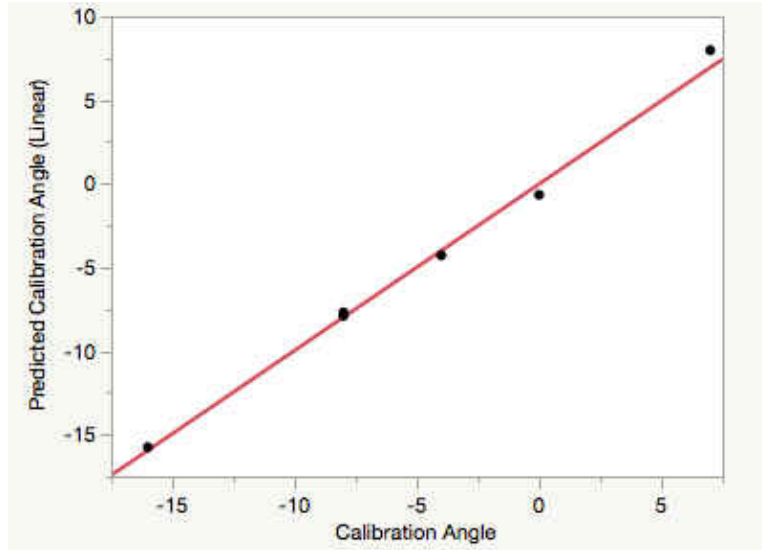


Figure 24: Linear fit model blade 3

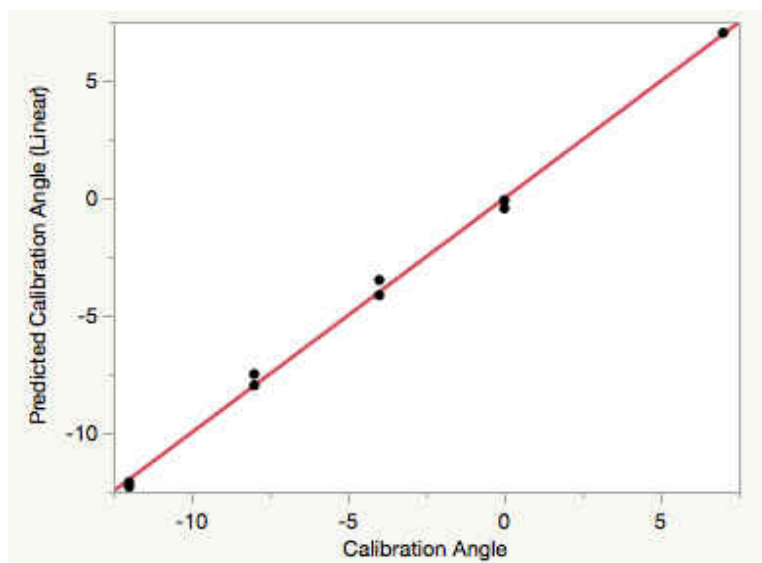


Figure 25: Linear fit model blade 4

The ANOVA tables for the blade lead-lag sensors with a linear fit applied are then evaluated and seen in Table 28 through 31. After reviewing the tables, it was determined that all of the terms were classified as significant due to an alpha value of less than 0.05.

Analysis of Variance				
Source	DF	Sum of Squares	Mean Square	F Ratio
Model	1	385.35016	385.350	2449.723
Error	7	1.10113	0.157	Prob > F
C. Total	8	386.45128		<.0001*

Table 28: ANOVA table blade 1

Analysis of Variance				
Source	DF	Sum of Squares	Mean Square	F Ratio
Model	1	404.96232	404.962	1869.876
Error	7	1.51600	0.217	Prob > F
C. Total	8	406.47832		<.0001*

Table 29: ANOVA table blade 2

Analysis of Variance				
Source	DF	Sum of Squares	Mean Square	F Ratio
Model	1	449.84043	449.840	1440.751
Error	7	2.18559	0.312	Prob > F
C. Total	8	452.02602		<.0001*

Table 30: ANOVA table blade 3

Analysis of Variance				
Source	DF	Sum of Squares	Mean Square	F Ratio
Model	1	308.56307	308.563	2607.162
Error	7	0.82846	0.118	Prob > F
C. Total	8	309.39153		<.0001*

Table 31: ANOVA table blade 4

After determining that all of the parameters are significant, the models were then evaluated to determine if the lack of fit was significant or not utilizing the F-test once again. Upon further analysis of the sensors in blades 1 through 4, it was found that the lack of fit for blades 1 through 3 were significant while blade 4 was insignificant as seen in Table 32 through 35.

Lack Of Fit				
Source	DF	Sum of Squares	Mean Square	F Ratio
Lack Of Fit	3	1.0146905	0.338230	15.6525
Pure Error	4	0.0864347	0.021609	Prob > F
Total Error	7	1.1011252		0.0112*
				Max RSq
				0.9998

Table 32: Lack of Fit table blade 1

Lack Of Fit				
Source	DF	Sum of Squares	Mean Square	F Ratio
Lack Of Fit	3	1.4336157	0.477872	23.2013
Pure Error	4	0.0823869	0.020597	Prob > F
Total Error	7	1.5160026		0.0054*
				Max RSq
				0.9998

Table 33: Lack of Fit table blade 2

Lack Of Fit				
Source	DF	Sum of Squares	Mean Square	F Ratio
Lack Of Fit	3	2.1641923	0.721397	134.8865
Pure Error	4	0.0213927	0.005348	Prob > F
Total Error	7	2.1855850		0.0002*
				Max RSq
				1.0000

Table 34: Lack of Fit table blade 3

Lack Of Fit				
Source	DF	Sum of Squares	Mean Square	F Ratio
Lack Of Fit	3	0.42599389	0.141998	1.4113
Pure Error	4	0.40247080	0.100618	Prob > F
Total Error	7	0.82846469		0.3626
				Max RSq
				0.9987

Table 35: Lack of Fit table blade 4

After determining that there was a significance in lack of fit in blades 1 through 3, it was imperative to evaluate the residual error within the measurements. From JMP statistical software, the residuals are taken and a graph depicting the calibration angle versus the residual error is created seen in figure 26.

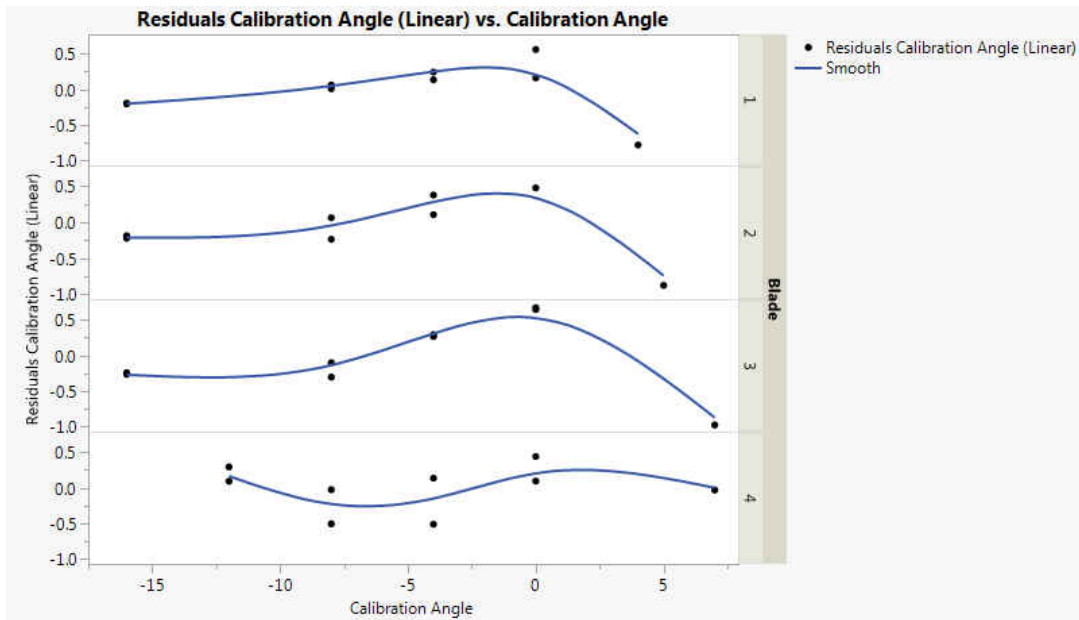


Figure 26: Lead-Lag Calibration Angle Vs Linear Residual Error

Blades 1 through 3 follow a similar trend that the residual error is the highest at the 0 degree calibration angle and the highest calibration angle for each run. Since these sensors are calibrated by eye mentioned above, the data suggest that whoever is calibrating at the time may have trouble aligning the marks in the positive direction. This translates to having an error of 0.67 degrees at the 7 degree calibration angle seen in blade 3. This error is almost 7 times outside of the accepted tolerance deeming the linear fit to be unusable when trying to accurately represent the system with minimal error. However, blade 4 stands out in that even though the lack of fit is insignificant it still carries a large variance between calibration angles -8 degrees and -4 degrees. This variance is as large as 0.37 degrees at the -4 degree calibration angle, again suggesting that the repeatability of the calibration is questionable. The large variance trend is then confirmed by comparing the RMSE found in the summary of fit tables, Table 36 through 39.

Summary of Fit	
RSquare	0.997151
RSquare Adj	0.996744
Root Mean Square Error	0.396615
Mean of Response	-5.77778
Observations (or Sum Wgts)	9

Table 36: Summary of fit table blade 1

Summary of Fit	
RSquare	0.99627
RSquare Adj	0.995738
Root Mean Square Error	0.465373
Mean of Response	-5.66667
Observations (or Sum Wgts)	9

Table 37: Summary of fit table blade 2

Summary of Fit	
RSquare	0.995165
RSquare Adj	0.994474
Root Mean Square Error	0.558772
Mean of Response	-5.44444
Observations (or Sum Wgts)	9

Table 38: Summary of fit table blade 3

Summary of Fit	
RSquare	0.997322
RSquare Adj	0.99694
Root Mean Square Error	0.344023
Mean of Response	-4.55556
Observations (or Sum Wgts)	9

Table 39: Summary of fit table blade 4

Given the ill effects of a linear regression model, a 4th order polynomial fit is applied to the data to decrease the residual error (Figure 27).

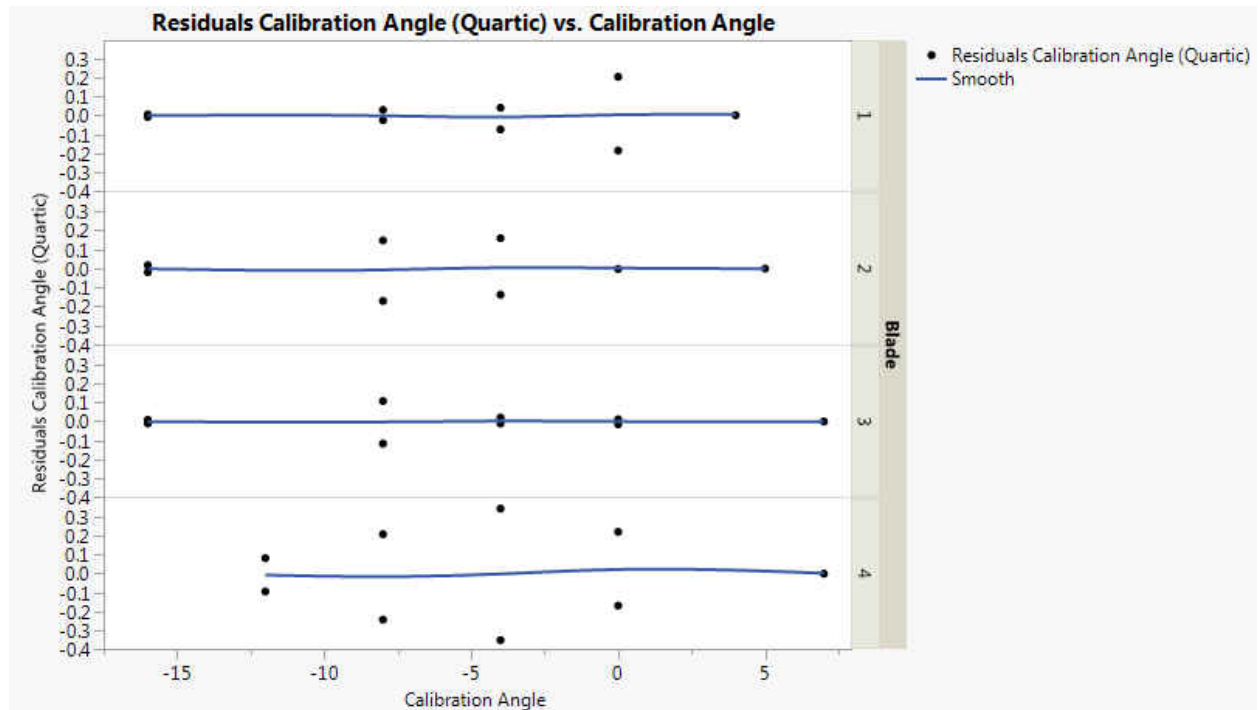


Figure 27: Lead-Lag Calibration Angle Vs Linear Residual Error

This model greatly reduced the residual error, however, each blade still contains residual error larger than the accepted tolerance at certain calibration angles. Blade 4 has the most error of 0.34 degrees with a variance of 0.69 degrees. This large variance trend continues throughout the data once again suggesting that there may be a problem with the calibration method being used.

2.3 Summary

After analyzing each blade and its 3 degrees of freedom a consistent trend of large variance found by analyzing the RMSE suggests that the current methods being used to calibrate these sensors could be flawed. It can be assumed that a non-linear model would best represent each system, but the non-linear models still do not bring all of the sensors within the desired tolerance range. This assumption is supported with the analysis of the standard deviation for each system. The standard deviation, one sigma, for each degree of freedom was compiled into one data set per sensor and represented in Table 40.

Axis	Standard Deviation (1σ)							
	Blade 1		Blade 2		Blade 3		Blade 4	
	Linear model	Non-linear model	Linear model	Non-linear model	Linear model	Non-linear model	Linear model	Non-linear model
Pitch	0.10	0.05	0.17	0.03	0.14	0.04	0.03	0.03
Flap	0.12	0.02	0.10	0.01	0.06	0.02	0.09	0.03
Lead-Lag	0.25	0.08	0.25	0.08	0.28	0.05	0.2	0.12

Table 40: Standard Deviation of Sensors

It can be seen that all of the standard deviations are out of the desired tolerance for the linear models with the highest being 0.28 degrees for the lead-lag. The non-linear model was able to bring the pitch and flap within the desired tolerance, but was still unable to satisfy the specifications for the lead-lag. These large variances and non-linear behaviors imply that the

current calibration process may not be repeatable and the most accurate. Therefore, it has been decided that a new course of action is needed when calibrating these sensors.

CHAPTER 3

LITERATURE REVIEW

After determining the current calibration method is possibly causing nonlinear and inaccurate data, a new method was proposed. The new method will focus on reducing the time it takes to calibrate each blade as well as increase the accuracy and repeatability of the blade calibration. To aid in the decision of what method to use, a literature study was conducted focusing on different measurement techniques used to measure blade displacement on helicopter rotors. From the literature study, it was found that the four most recognized techniques were the use of interferometry, photogrammetry, coordinate measurement arms, and inertial measurement units (IMU).

3.1 LASER TRACKER

3.1.1 Historic Background

The first laser tracker was invented by Lau et al. in 1987 at the National Institute of Standards and Technology (NIST) in an effort to increase the accuracy of robot metrology [11]. During this time, the use of robotics was increasing in the manufacturing industry to streamline the assembly process. These simple robotic machines consisted of an arm that performed a task commanded by a small controller. However, during this time period robotics were not very sophisticated resulting in poor accuracy. This problem stemmed Lau to come up with a design that allowed the robot to “know” where its arm was at all times during its movement. The first prototype design consisted of a device that was mounted to a rotary table with a laser beam that

tracked a reflective target. As the target moved, the rotary table would make small adjustments allowing the beam to stay in contact with the reflective target and record the targets position [12]. The prototype transformed into the first laser tracking that encompassed a distance measuring interferometer and a set of encoders analyzing the azimuth and elevation angles. This new technology allowed for easier transportation, faster measurements, and more accurate static and dynamic measurements [13]. Since the success of the first laser tracker, many improvements have been implemented into the original design aiding in the overall performance of the trackers themselves. With the modern day laser tracker having tolerances as small as 0.7 microns [14], it has become a popular measurement tool within the metrology field.

3.1.2 Concepts of Operation

Generally, the measurement of the X, Y, and Z coordinate positions are sufficient when there is a need to measure position of a system. Therefore, a 3-D laser tracker system can be used to accommodate the need to obtain precise measurements on a system of particular interest. A reflective target, also referred to as a retroreflector, is used as the measurement point when using this style laser tracker system. The concept behind the retroreflector is that if a beam is off center with respect to the reflector, the reflected beam will be offset as well [15]. Consequently, if the beam were to strike the center of the reflector, the returned beam would follow the same path as the transmitted beam [15]. Given the properties of the retroreflector, a mechanism such as the laser tracker can be devised to track specified targets by keeping the returning beam on the same path as the transmitted beam.

To accommodate the characteristics of these reflective targets, various components are combined to develop a 3-D laser tracker. The tracker is comprised of angle encoders with beam steering technology, an interferometer, a laser light source, a reflective source, a control module, and other miscellaneous components [16]. A schematic of a laser tracker can be seen in Figure 28.

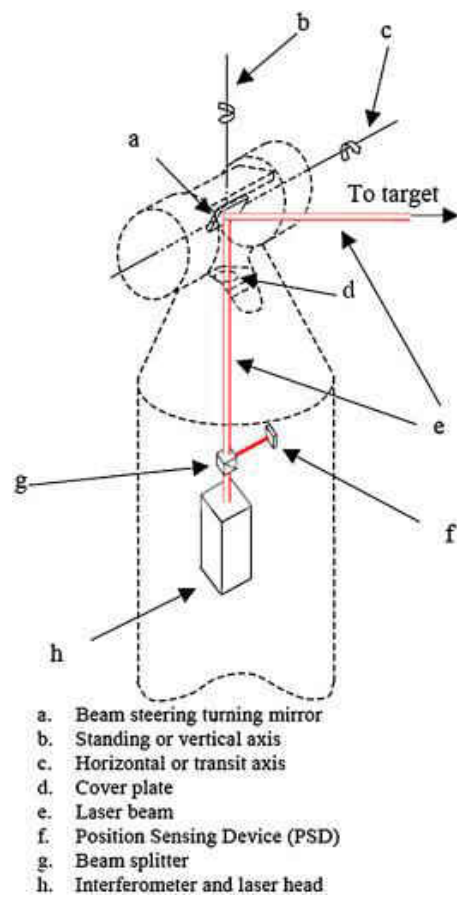


Figure 28: Schematic of Laser Tracker [16]

The general functional process of a laser tracker starts by placing a retroreflective target on the item being measured. These targets typically consist of a cat eye reflector or a spherically mounted retroreflector (SMR) seen in Figure 29.



Figure 29: Cat Eye and SMR Reflectors [18]

The SMR is the general target of choice due to its lower cost and its availability to the common consumer. The SMR consists of three variations that can be used when taking measurements, each with its own properties. These configurations consist of the solid glass SMR, the open air SMR, and the open air with a window covering SMR [18]. Each configuration contains its own acceptance angle; the angle in which the reflector can accept and reflect the beam to stay within the tolerances of the tracker. Generally, the SMR can be condensed into only two configurations when it comes to the associated acceptance angle, the solid glass and the open air. The solid glass SMR has a larger acceptance angle of $\pm 40^\circ$ while the open air SMR only has an acceptance range of $\pm 25^\circ$. With the low cost and durable, precise performance the SMR is a very common reflector used in industry. However, if a wider acceptance range is needed a cat eye reflector is generally the reflector of choice. This reflector is typically more expensive, but the higher costs allow for the reflector to have a larger acceptance angle. This angle is increased from $\pm 40^\circ$ to $\pm 120^\circ$ due to its geometry during the manufacturing process. These reflectors are

generally made up of two solid glass hemispheres that are fused together to become a cat eye reflector. The front hemisphere is the smaller of the two with a purpose of refracting the light to the center of the sphere. Once the light has entered the center of the sphere, the light then moves through the rear hemisphere. The rear hemisphere is larger thus projecting a smaller beam to the rear surface of the hemisphere. The smaller beam projection is then reflected off the rear surface of the hemisphere and parallels the transmitted beam back to the tracker. [18] However, since the light is being refracted from one hemisphere to another, the beam wavelength must be considered when choosing a cat eye reflector. This wavelength is determined by two factors: the laser tracker's interferometer (IFM) and the laser tracker's absolute distance meter (ADM). The IFM is measured by splitting a beam and measuring its incremental time cycles as it is reflected off a retroreflector, and the ADM uses beam flight time to determine the absolute distance from the target [19]. Problems occur when using a cat eye reflector if the IFM and ADM wavelength are not close enough to each other when a laser tracker contains both measuring systems. If the wavelengths differ too much, then one wavelength may refract in a different way, not allowing the source to be reflected back to the tracker [20]. After the retroreflector is chosen, the process of tracking the target with a laser tracker can begin.

The laser tracker is typically mounted to a portable tripod stand that can be placed at various stations around the object being analyzed. Once the reflector is mounted to the target, the laser tracker is turned on and starts the measurement process by searching for and locking onto the retroreflector. The measurements are taken by measuring three components of the system: the azimuth angle, the elevation angle, and the measured distance. The first measurement taken is the distance measurement using solely IFM or IFM with ADM technology.

The idea behind IFM technology is the motion of merging two or more sources of light that come together to create an interference pattern. This pattern is then analyzed by summing the heights and depths of the separate waves to generate the interference pattern [20]. These waves are classified as being constructive or destructive waves seen in Figure 30.

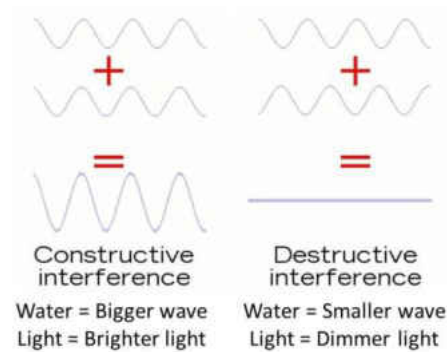


Figure 30: Constructive and Destructive Waves [22]

The theory behind inspecting the interference patterns from these constructive and destructive waves stems from the Michelson Interferometer. Originally, this technique was used to prove the existence of ether, however, the theory behind it has been implemented into laser tracker technology [22]. The Michelson Interferometer consists of a light source that is split into two beams that are reflected off two targets, one being a reference target and the other being the measured target seen in Figure 31.

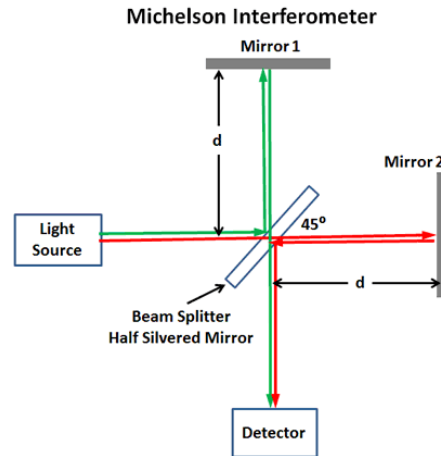


Figure 31: Basic depiction of Michelson Interferometer [23]

These two beams are then combined and create an interference pattern, also known as an interference fringe. This interference fringe provides information that resembles the combined wavelength height and depth. These fringes are counted and a measured displacement of distance is determined [24]. Although the interferometer is an accurate, robust system it does have its drawbacks. As a result of the general operation of the interferometer, if the beam is broken during measurement the tracker must be returned to a reference location to reorient itself to the target. This process can cause increased measurement time and complexity, therefore, the industry has introduced ADM technology.

To aid in the measurement process when the IFM is interrupted, the ADM was developed to prevent the laser tracker from having to be reset if the beam was broken. This technology determines distance by analyzing the amount of time it takes for the beam to be reflected back from the target [24]. This process begins by projecting a beam to the reflective target then waiting for the beam to be reflected back. Once the beam is reflected back the ADM integrates the time of flight of the beam to determine the target distance [24]. Since this does not rely on knowing the current position of the laser tracker, this system allows the tracker to reorient itself

with its current location from the target. From there, the IFM within the tracker takes over again to continue the measurement process, since it is the superior measurement technique [24].

The laser tracker outputs a frequency-stabilized, helium-neon laser into a beam splitter that directs one beam into the interferometer and the other beam onto the retroreflective target to initiate the distance measurement. The beam that is directed towards the interferometer is used as a reference beam while the other beam is used as the measurement beam. The measurement beam passes from the beam splitter to a steering mirror and then to the target. The beam steering mirror consists of two axes, the horizontal (azimuth) axis and the vertical (elevation) axis. To measure the azimuth and elevation angle displacement an angle encoder is mounted coaxially along the horizontal axis and another is mounted coaxially along the vertical axis [25]. Once the beam is reflected back to the tracker, a portion of that beam is directed to a position sensor detector and the other portion is directed back to the interferometer for fringe counting to occur.

After the interferometer determines the distance by the method of fringe counting, the position sensor begins its process to determine the azimuth and elevation of the target. The integrated position sensor detects the amount of offset the laser beam is experiencing from the reflective target and initializes micro adjustments within the encoders to mitigate the measured offset. Once the encoders steer the beam back to the center of the reflective target, position coordinates are recorded to define the position of the target. These coordinates are then transformed from spherical coordinates to Cartesian coordinates utilizing the distance and two angles measured by the laser tracker. As the target moves through its range of motion, this process incrementally records the data to obtain an accurate measurement of the total movement of the target. With the collaboration of each component within the laser tracker, seen in Figure 32, accuracy as small as 0.7 micrometers can be obtained [14].

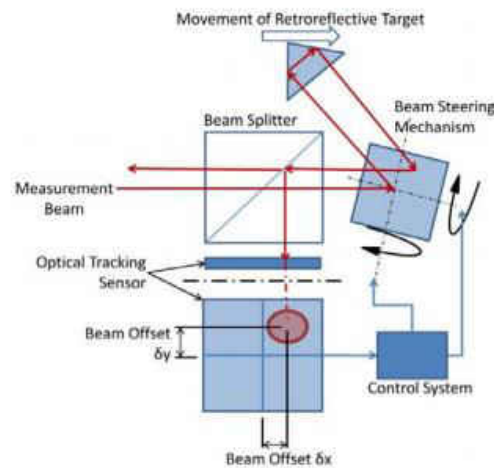


Figure 32: Laser Tracker Components [26]

3.1.3 Case Study

With the given background information from the literature review pertaining to the laser tracker system, an example application of this system was desired. This would better explain how the system will measure the blade angles as well as highlight problematic areas to address in the method used by previous researchers. Therefore, the article “Laser and Vision-Based Measurements of Helicopter Blade Angles” by Emmanuel et al. was analyzed [27]. The article discusses the method of using a laser system to measure the pitch, flap, and lead-lag angles of helicopter rotors during flight.

The study focuses on using 2D laser triangulation on a 3D target that is mounted to the tension link of the blade grip. This is done by fixing the laser sensor to the top of the hub so that it will spin at the same rate as the 3D target. The laser then analyzes the orientation of the 3D

target by projecting a beam onto the target surface that analyzes the designed sharp corners and ridges of the target (Figure 33).

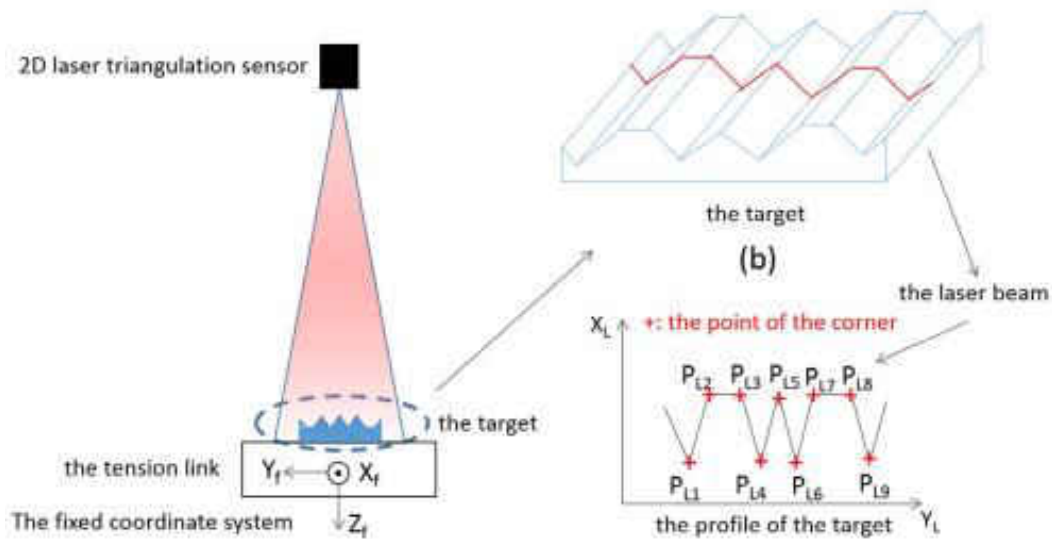


Figure 33: Laser projection on target [27]

Once the target is analyzed in the laser sensor coordinate system, it is transformed into the hub-fixed coordinate system to determine blade orientation using the pseudoinverse algorithm [27]. However, before the measurement can begin, the sensor must be calibrated to the target. This calibration process involves tilting the target in various ways to measure three assigned points that aid in determining the parameters needed to transform the data from laser sensor coordinate system to the hub-fixed coordinate system. After calibrating the sensor to the 3D target, a rotation and vibration analysis was conducted to ensure there was no influence in measurements from the sensor movement. The vibration analysis utilized an electromechanical shaker that was driven at a frequency simulating the vibrations induced by an Agusta Westland AW139 rotor hub. The vibration test concluded that the vibrations had no effect on the sensor in terms of gathering data. The sensor was then placed through a vibration test coupled with a

rotation test using a ground-tied fuselage housing an AW139 gearbox and simplified rotor hub. This allowed the sensors to experience the vibrations and centrifugal forces generated by the hub during flight. Again, these tests concluded that the rotational forces and vibrations induced by the hub had no effect on sensor data collection. Therefore, after verifying the sensor is sustainable in the testing environment, the experiment was conducted.

The test setup used in the experiment utilized the AW139 endurance rig at the Leonardo Helicopters laboratories [27]. This rig contained the subassembly of the AW139 main rotor allowing the system to model real world applications. The rig allowed the blades to be moved one axis at a time or by fully coupling the flap, pitch, and lead-lag blade movements generated realistic blade movements experienced during flight. During the experiment, the rotor was spun at 4.94 revolutions per second sampling at 247 Hz, which equates to 50 samples per revolution [27]. Realistic blade motion was evaluated by analyzing the system with the 3 axes of motion fully coupled at the rotational speed mentioned. The blades were then trimmed at four different levels during the flight simulation with an incremental increase of freestream airspeed values v_1 , v_2 , v_3 , and v_4 . While in motion, the range of motion applied to the blades were as follows:

- Pitch angle: -22 to 22 degrees
- Flap angle: -2 to 12 degrees
- Lead-Lag angle: -3.5 to 6 degrees

After conducting the experiment, it was determined that the laser system had discrepancies as large as 1 degree in the lead-lag measurement, but had much smaller errors in the pitch and flap measurement. The high error in the lead-lag measurement was probably caused by only having small changes in the target profile when measuring that axis. Due to the operating principle of the laser system, it depends on profile changes of the 3D target. Since the lead-lag

only measures side to side movement, the target does not experience a rotation or depth change during measurement, hindering its ability to detect a change in angle when compared to the pitch and flap measurement. Also, as the pitch angle approached the maximum and minimum values it acquired larger error as well, attributable to the operating principle. As the target rotated to these steeper angles the laser sensor was unable to detect the measurement points due to the disappearance of the points within the valleys of the target. During this experiment, the author sanitizes the paper by not including specific velocity values during the four tests as well as the standard deviation associated with the values. Therefore, these four velocities will be referred to as V_1 , V_2 , V_3 , and V_4 . The following table summarizes the mean errors associated with each blade axis at the four given velocities:

	Velocity 1 (V_1)	Velocity 2 (V_2)	Velocity 3 (V_3)	Velocity 4 (V_4)
Lead-Lag (deg)	1.05	0.795	-0.828	-0.67
Flap (deg)	-0.031	-0.00721	0.0159	0.0309
Pitch (deg)	-0.269	-0.209	-0.273	-0.29

Table 41: Summary of Results

The results concluded that the laser system was able to measure the blade motions during flight even though some axes had large error. However, this system is being analyzed dynamically, whereas the new calibration method discussed in this thesis will be analyzed statically. Also, the laser sensor used is a low cost 2D sensor while the new calibration method will be using a higher quality 3D laser tracking system. Therefore, it can be assumed that the new calibration method will be superior in accuracy when compared to the analyzed 2D

measurement system. Based on the success discussed in the paper, it is determined that the laser tracker system could be a candidate to implement in the new calibration method.

3.2 PHOTOGRAMMETRY

3.2.1 History/ Background

The method of photogrammetry was first used by a French geodesist by the name of Francois Arago in 1840 in an effort to determine the position of an object in space without prior knowledge of its position using triangulation. A few years later a Frenchman by the name of Laussedat, bestowed with the name “father of photogrammetry”, created topographic maps using terrestrial photographs for the French Army [28]. Since then, photogrammetry has gone through four development cycles: Plane table photogrammetry, Analog photogrammetry, Analytical photogrammetry, and Digital photogrammetry [28]. Throughout these phases photogrammetry has evolved into a metrology tool that has the ability to capture the static and dynamic geometry of various systems. These images allow engineers to analyze critical information of the systems being evaluated such as material deformation, displacement, and position. Photogrammetry can be broken down into three major types: Aerial photogrammetry, Land photogrammetry, and Satellite photogrammetry [29]. Aerial photogrammetry is typically used to create topographic maps of new locations. This is done by mounting cameras to an aircraft that flies over unknown areas to record the geographic features. Satellite photogrammetry is similar to aerial, however, this method is done by mounting cameras to satellites that are used to triangulate an object or area on the Earth [29]. Land photogrammetry, also known as close range photogrammetry, typically consists of placing a camera on the ground mounted to some type of tripod or pole. This

photogrammetric method is typically used to create 3D models, obtain desired measurements, or create point clouds.

3.2.2 Concepts of Operation

Digital photogrammetry has been perceived as being an accurate way to capture crucial measurements of an object where traditional measurement tools are unable. These measurements are obtained by taking a series of photographs that are used to determine point coordinates, define features and patterns of an object, or to determine the boundaries of the object being measured [30]. Two of the most common types of cameras used for photogrammetry are the Charged Coupled Devices (CCD) and the Complementary Metal Oxide Semiconductors (CMOS). The CCD camera utilizes a chipset that converts the analog light to digital pixels with high resolution and low distortion. The CMOS camera, however, utilizes transistors that transport the charges generated by the pixels through a traditional wire set. Since the data is moved through a wire set the images from a CMOS camera tend to have higher noise making them a lower resolution compared to the CCD cameras [31]. These cameras are generally set up in two configurations to obtain data: a single camera setup or a stereo camera setup. The single camera setups allow for two dimensional measurements such as measuring the displacement of an object, whereas the stereo camera setup allows for three dimensional measurements involving point coordinate measurements using the method of triangulation seen in Figure 34.

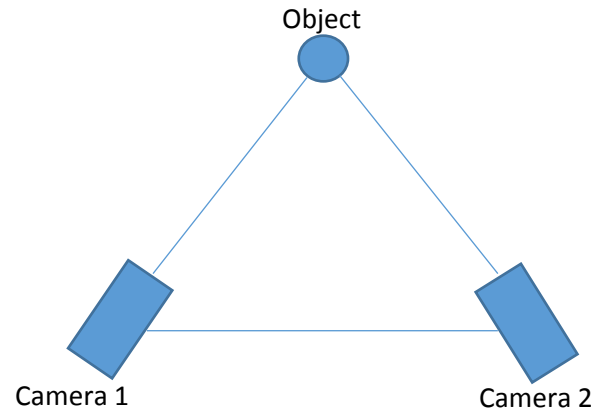


Figure 34: Stereo Camera Triangulation

The measurement process begins by calibrating the camera(s) to reduce distortion and increase the accuracy of the photographs being taken. This calibration process typically follows the method of bundle adjustments, which examines all system parameters and correlates them with the interior and exterior orientation parameters. These parameters include principal distance and offset, three coefficients of radial distortion, and two coefficients of decentering distortion [31]. These parameters are adjusted by placing the cameras on a scale bar of known length and aiming them at a coded target to analyze. The camera begins taking the measurement and each parameter is adjusted until the measured value falls into the specified desired tolerance. Once the cameras are calibrated, accurate measurements are taken using one of two most common methods: a target or a target-less approach.

The target approach consists of placing a target on the object being measured for the camera to “follow”. These targets are typically some form of retroreflective sticker with a circular pattern that is classified as being coded or non-coded seen in Figure 35.

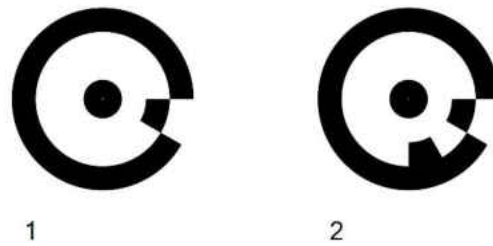


Figure 35: Photogrammetry pattern target [32]

The non-coded targets are placed throughout the structure to identify the geometry of the object being measured. Once the geometry is defined, coded targets are then used to obtain more precise measurements. The coded style retroreflectors allow the camera system to identify the target easier at various angles as well as increase the accuracy of the measurement. These coded targets are made with a solid circle in the center that is a minimum of 10 pixels across in the photos [33]. The advantage of using these coded targets is that the user is able to precisely place the target on the exact point desired for measurement as well as having the flexibility of being able to control the measurement density. Therefore, the user is able to adjust the measurement tolerances based on the density of targets placed. Another advantage of using these coded targets is that when two targets are placed close together and the camera offset is large, the coded targets allow identification of a third point in space that the camera is unable to capture.

Another method of taking measurements with photogrammetry is using a target-less approach. These types of measurements include edge detection and pattern recognition within the structures being observed. The most common algorithm used with this approach is edge detection due to its speed and low computational demand [30]. This method is commonly used in situations where reflective targets cannot be mounted such as on thin, long cables or low-profile edges. The method greatly reduces the setup complexity while still producing quality results.

Once the measurement approach is chosen, the cameras are placed around the object being measured and photos are taken. These photographs are then analyzed through proprietary software that translates the analog images to associated numeric values. During this transformation, coordinate positions are determined as discussed in a later section and the object distance is calculated. Since the stereo cameras are on the same plane as each other and at a specified distance apart, image correlation is used to determine the objects distance [34].

This is done by evaluating the image overlap of the two cameras being used during measurement. More specifically, the x coordinate of the image plane of the left and right camera are compared to the baseline, the horizontal distance between the two cameras, and scaled by the focal length to determine the object distance. This is done in the following manner [34]:

$$Distance = \frac{baseline * focal\ length}{x_{left\ camera} - X_{right\ camera}}$$

3.2.3 Case Study

To better understand how the photogrammetry technique could be applied, a case study was found applying this metrology technique. The case study “An optoelectronic system for the in-flight measurement of helicopter rotor blades motions and strains” by Huang et al. discusses the use of a single CCD camera to measure the flap, lead-lag, and pitch angle of a helicopter blade during flight [35].

The study focuses on using the technique of optical triangulation to determine the blade angles during operation. This is done by placing the flight test system on the rotor hub containing the required measurement sensors. This unit is comprised of three CCD cameras that independently monitor the position of the three blades attached to the hub and onboard

processing equipment that translate the measured coordinates into blade angles. Once the flight system is mounted to the rotating hub, two light emitting diodes (LED) are placed on each blade. These LED's allow the CCD cameras to determine blade position based on the position of the LED. The flap and lead-angles are derived from a single LED, and the pitch is derived from combining the positions of the two LED's (Figure 36).

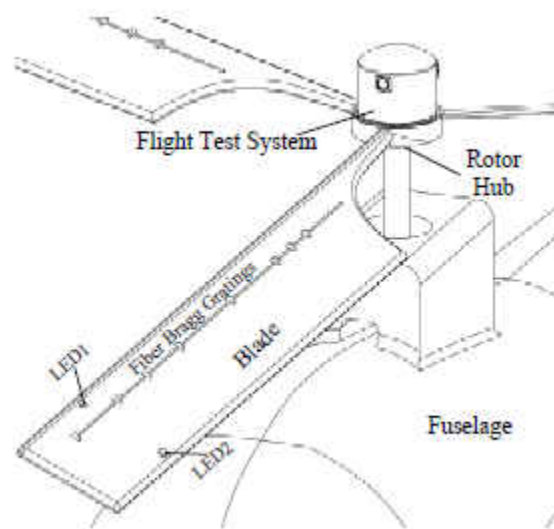


Figure 36: Experimental Test System [35]

Once the sensors are fixed to the experimental testing rig, the model is spun at an unknown rpm utilizing three stepper motors to aid in the actuation of the blade angles. The input angles for each blade axis are as follows:

- Flap: -7 to 20 degrees
- Lead-Lag: -7 to approximately 11 degrees
- Pitch: 0 to approximately 22 degrees

Upon experimental investigation, it was found that each measurement axis had an error of approximately 1% of the measurement range. This equates to roughly a 0.27 degree error in flap, a 0.18 degree error in lead-lag, and a 0.22 degree error in pitch. These results correlate well with the study discussed in the laser tracker section. The study involving the laser sensor by Emanuele et al. also utilized a single and stereo optic set up in a similar manner to analyze blade angles during operation [27]. The setup and sensor analysis was conducted similarly to the laser sensor, therefore, the reader can refer to that section to recall the experiment configuration. The following figure is a representation of the single and dual camera setup:

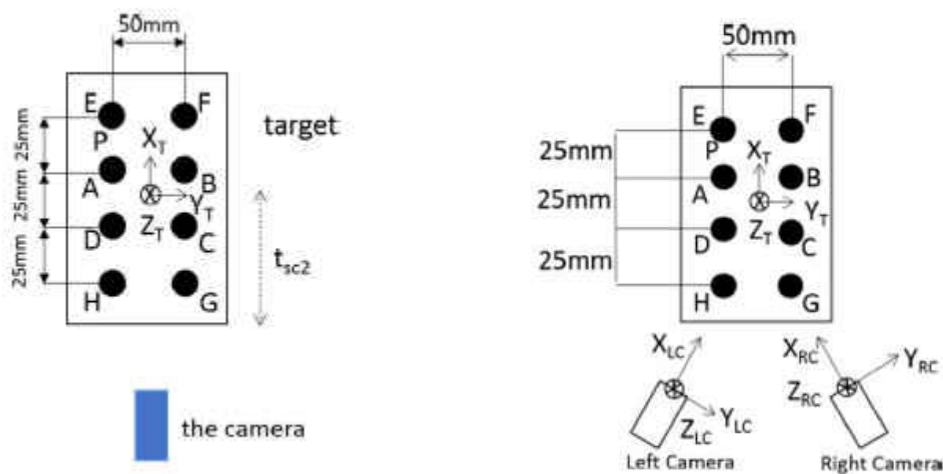


Figure 37: Single camera setup (left) and dual camera setup (right) [27]

This test concluded that the single camera setup at airspeed velocity one had similar results to the study conducted using the three CCD cameras [27]. Once the stereo camera setup was implemented and analyzed, it was found to be superior to the single camera setup. Due to the data representation in [27], approximations of error are determined based on the provided

plots. Therefore, the data will be presented using the plot from [27] as table 3. Unfortunately, the author does not specify the velocity values as well as if the data is one standard deviation.

	Single Camera Vision	Stereo Camera Vision
Flap (deg)	0.08	0.1
Lead-Lag (deg)	0.05	0.01
Pitch (deg)	0.35	0.25

Table 42: Single Vs Stereo Camera Measurement Uncertainty

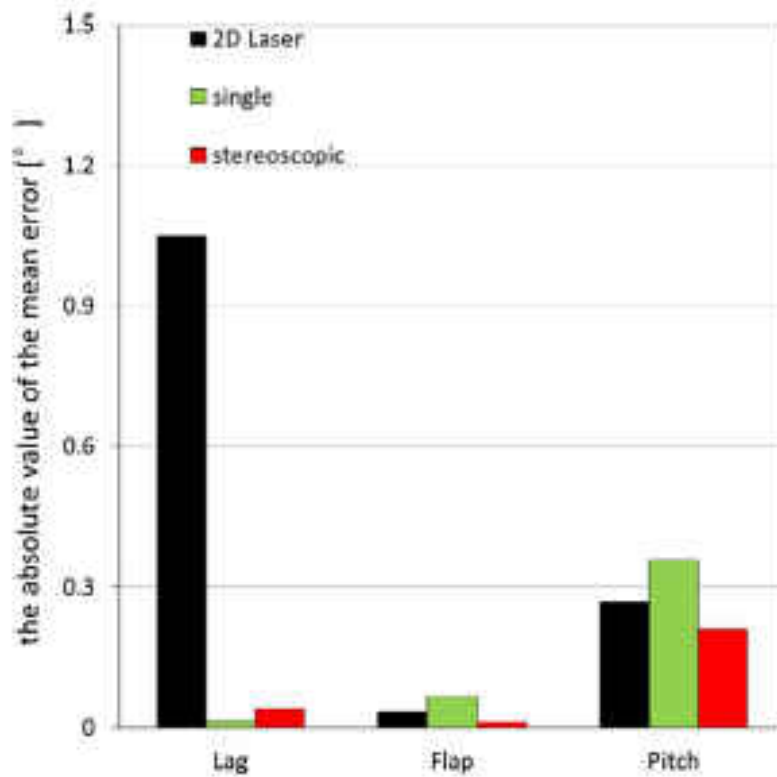


Figure 38: Plot of errors [27]

All of these results are generated using a dynamic platform making it challenging for the sensors to obtain accurate measurements. Even though the system is dynamic, the sensors are still capable of generating accurate measurements within 0.3 degrees. Therefore, it can be assumed that the data collection is successful and when applied to a static model it can be much more accurate making it a candidate for use in the new calibration method.

3.3 Coordinate Measurement Arm

3.3.1 Historic Background

Coordinate measurement machines have been around for the past 60 years becoming more precise after each design iteration [36]. Before these machines were invented, measurements relied on humans to measure parts up to the thousandth of an inch using analog technology. These types of measurements were relatively accurate for small scale building, however during large scale manufacturing the quality control varied greatly due to inconsistent human measuring [36]. To overcome these problems, coordinate measurement machines were invented in the 1950's and early 1960's with 2 and 3 axis measurement capability [36]. These machines were operated manually with the ability to measure in the X, Y, and Z coordinate system using a series of micrometer fine adjustments that measured the position of a solid probe mounted to the machine. As time progressed, Sir David McMurtry invented the first touch trigger probe in 1972 allowing for over travel after contact of the probe was automatically detected [36]. This device allowed Olympus engines to pass specific requirements needed when building their Concorde aircraft [36]. Since then, 3D measurement has further progressed into

digital systems and it is now allowing engineers to take measurements that have high accuracy and are repeatable.

3.3.2 Concept of Operation

The coordinate measurement arm (CMA) has become more popular in the metrology industry due to its portability, high accuracy, and its ease of use. This type of coordinate measurement machine allows the user to place the arm around or on the object to be measured at virtually any desired location seen in Figure 39.



Figure 39: Coordinate Measurement Arm in use [37]

This is done by using two different style mounts: a tripod setup or a fixed base mounted to the object being measured. The tripod setup consist of a prefabricated base that the measurement arm is affixed to allowing the arm to be steadily placed about the subject. The

other style mounting system is a base mount that is fixed to the object being measured. This is done by placing a mounting base, usually magnetic, to the object being measured (Figure 40). The magnetic base allows the measurement arm to be securely attached to the machine being measured while still maintaining the versatility of easily removing the CMA. This style mount allows the user to place the arm in locations not reachable by the tripod stand allowing for full range of motion during the measurement sequence. Once the desired mount is chosen, the measurement process can take place.



Figure 40: Mounting styles of CMA [38]

The CMA uses a series of articulating joints to allow for full range of motion during the measurement process. Attached to the end of the series of joints is a “pistol” like device with a measuring probe on the end of the “barrel”. The operator uses this tool to place the tip on the surface of the object being measured. Once the probe is in position the operator presses a button on the machine that documents each joint position. Within these joints are rotary encoders that measure the movement angle of each joint while the system is being measured. The information from the encoders is compiled into the proprietary software associated with the CMA and

translated to a coordinated position. The accuracy associated with the determined position is generally in the 0.002 inch to 0.004 inch range per 12 feet of arm used [39]. Once the measurement is taken, the operator simply places the probe at the next measurement point and the process repeats. However, before any type of measurement is taken the machine must be calibrated once it is placed in its measurement position. This process is done by using a calibration plate provided with the CMA. This plate consists of three dish-shaped contact points with a known location that the CMA uses to orient itself (Figure 41). The operator places the probe on each point and captures the position by pressing the measurement button on the CMA. After the CMA is calibrated, the measurement process can begin.



Figure 41: CMA calibration plate [40]

Sometimes, the CMA must be repositioned to make all measurements needed to fully capture the system being evaluated. In this case, the arm must “jump” to the next position to be able to reach the desired measurement points. This action of moving the arm to another position

requires the arm to be calibrated again. This is done in a similar manner mentioned previously, however, an added step of measuring the previous location of the arm is need. This allows the arm to “know” its previous position to maintain consistency throughout the measurements.

3.3.3 Case Study

Given the ease of use of the FARO Arm, a case study was found that evaluated the overall operation of the metrology device to aid in better understanding how the system could be applied to the new calibration method. The study “Use of a Faro Arm for optical alignment” by Crause, A et al. discusses the use of a 1.8 meter, 6-axis platinum Faro Arm to correct the poor image quality of the Southern African Large Telescope (SALT) [41]. The purpose of using the Faro arm was to measure the focal gradient across the focal plane and adjust the gradient to increase the image quality of the telescope. However, the test turned into highlighting characteristics of the Faro Arm itself. Before the measurements were done, accuracy and repeatability tests were conducted. The repeatability test was done by doing a single point articulation test and the accuracy test was conducted by measuring traceable length artifacts at different locations within the working volume [41]. These tests concluded that the probe had to be calibrated regularly due to the software losing track of the probe. Also, if a new probe was used it must be recalibrated. After performing the accuracy and repeatability test, it was found that there was an overall spread of 100 microns based off the 1000 measurements taken concluding that the initial calibration done at the factory is rather poor seen in Figure 42 [41].

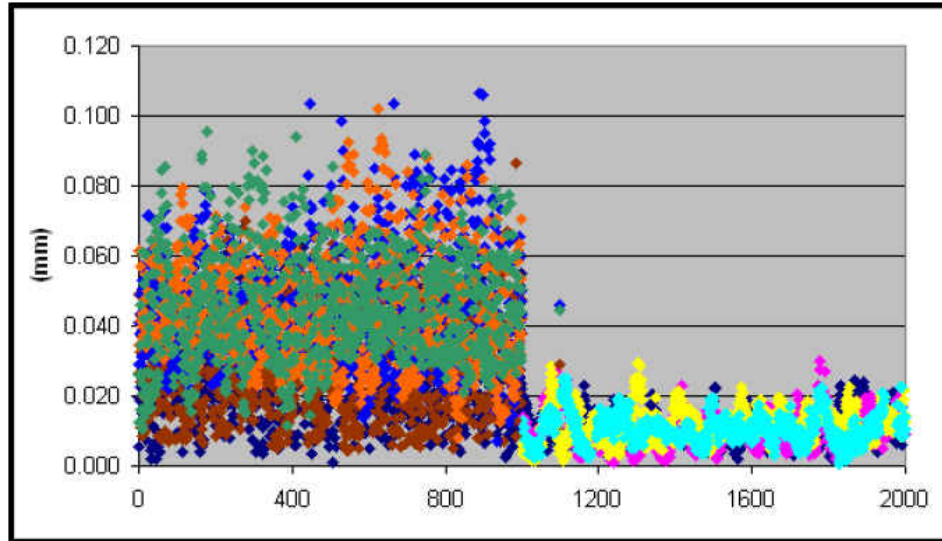


Figure 42: Accuracy and Repeatability Measurement Spread [41]

After concluding the poor factory calibration, the measurement process proceeded in evaluation by investigating the error when the Faro Arm “jumps”. The “jump” refers to moving the faro arm from one base position to another to fully capture the system being measured when a single base station is not sufficient to reach all points [41]. This process is done by measuring 3 fixed points at the initial location, moving the arm to the next location, and re-measuring the same base location points. The software then reorients the arm’s coordinate system based on the new location. This test determined that the arm contains a RMS deviation of less than 20 microns when measuring the three jump points [41]. During the measurement process, some complications arose interfering with the repeatability of the system. Therefore, Invar buttons were created to aid in measurement repeatability as seen in Figure 43.



Figure 43: Invar buttons [41]

These buttons contained pyramid-like indentions that were fixed to the object being measured so that the measuring probe could be placed on the object in a repeatable manner. The device was also used to aid in keeping the probe in position during movement. Overall, it was determined that the Faro Arm was user friendly, effective when operating without much articulation, and contained live feedback making it easier to interpret fine adjustments. Despite the poor calibration done at the factory, it is still considered to be a feasible option to apply to the new calibration method.

3.4 GYROSCOPE

3.4.1 Historic Background

Gyroscopes have been used over many years to aid in determining orientation of an object in motion. The first gyroscope was invented by John Serson in 1743 which was nicknamed the whirling speculum designed to identify the horizon by using it as a level [42]. Since then, gyroscopes have evolved into navigational devices that were first used in 1904 by militaries across the world [42]. Through the generations, gyroscopes have evolved into complex

devices that aid in piloting aircraft and determine position and orientation of devices such as cell phones. These devices have become vital components of current technology today, evolving from single axis setups to three axes setups and able to determine angular velocities as small as 0.5 milliarcseconds [43].

3.4.2 Concept of Operation

The gyroscope has been a crucial inertial measurement device used in systems such as aircraft, automobiles, and other systems that move. The main objective of the gyroscope is to determine the angular velocity the system is moving with respect to its surrounding environment. These angular measurements help determine the RPM at which the system is operating or the relative angle the system has moved with respect to its reference point. There are three main categories of gyroscopes that are used to take these measurements: the ring laser gyroscope (RLG), the fiber optic gyroscope (FOG), and the micromechanical systems (MEMS) gyroscope.

The ring laser gyroscope contains no moving parts and is capable of measuring one degree of freedom at a time. Since there are no moving parts, the amount of gyroscopic drift is greatly reduced as a result of the frictionless environment which increases its accuracy [44]. The theory behind the RLG is that it is capable of measuring a rotation about its sensitive axis, therefore, the orientation of the RLG must be known at all times. The concept behind the operation of an RLG is that there is a laser beam within the gyroscope that is split into two beams. Both beams travel the same path, however, the beams travel in opposite directions [44]. These beams are steered within the cavity of the gyroscope using a series of mirrors and are directed into a photo detector that analyzes the two beam wavelengths. In the absence of rotation

the wavelengths remain the same, therefore when the interference pattern is analyzed, there is no interruption. As a result of the wavelength not changing, the RLG interprets the data as zero movement. However, as the gyroscope begins to spin the beam phase begins to diverge from the opposing beam. This phase shift creates an interference pattern that is translated via a diode into a rotation rate [45].

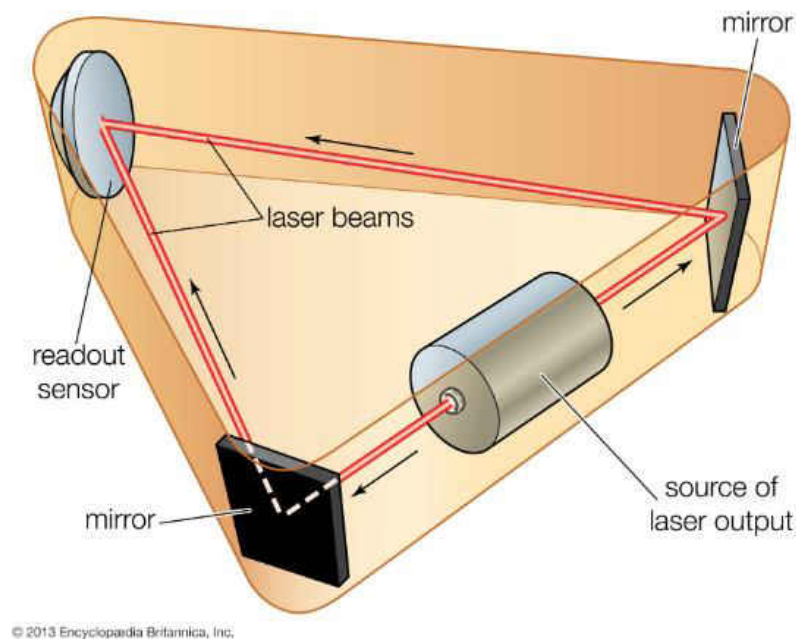


Figure 44: Representation of RLG [46]

The FOG follows a similar process to the RLG, however instead of steering a beam of light with mirrors the gyroscope utilizes fiber optics to direct the beam path. The process begins by directing a laser beam into a fiber optic bundle that splits the beam in two. The two beams travel within the same fiber, but they travel in opposing directions. Once the beams travel through the fiber, they are directed to a photo detector that analyzes the time differential between

the two beams. Therefore, when the gyroscope is not spinning the beam travel time will be the same resulting in a zero time differential. However, as the gyroscope begins to spin the beam traveling against the rotation will experience a shorter path delay, known as the Sagnac effect [47]. The Sagnac effect causes a phase shift between the two beams due to the rotation of the gyroscope resulting in different travel times [47] from which angular velocity is determined.

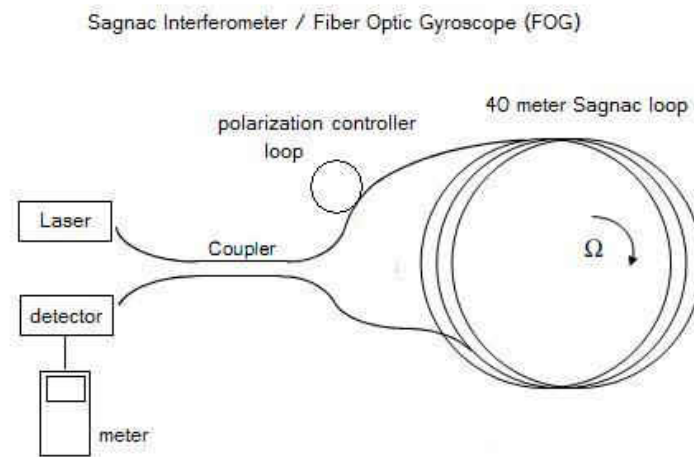


Figure 45: Representation of FOG [48]

The MEMS gyroscope uses a different approach over the RLG and FOG to obtain angular velocity information. These newer style gyroscopes incorporate the ability to measure angular rates in a much smaller, more affordable platform over the RLG and FOG style systems. Typically the MEMS gyroscope uses a tuning fork configuration comprised of two proof masses that move within the body of the gyroscope [49]. As the gyroscope begins to spin, these masses begin to oscillate in opposing directions due to the Coriolis Effect explained in an earlier section. Since these masses move in opposing directions, there is a differential in capacitance between

the two masses [49]. This capacitance is directly related to the angular velocity via a transformation equation unique to the sensor being used. This angular velocity is then translated to an analog or digital output that becomes an input to the analysis software being used. One important characteristic to consider when using these style gyroscopes is their inability to detect linear acceleration. Due to the inherent nature of how these sensors work, linear acceleration would cause both proof masses to accelerate in the same direction at the same rate. This would result in a zero differential in capacitance between the two masses thus giving a zero read out. This proves to be an advantage to the sensor since this characteristic mitigates effects from shocks or vibrations during use [49].

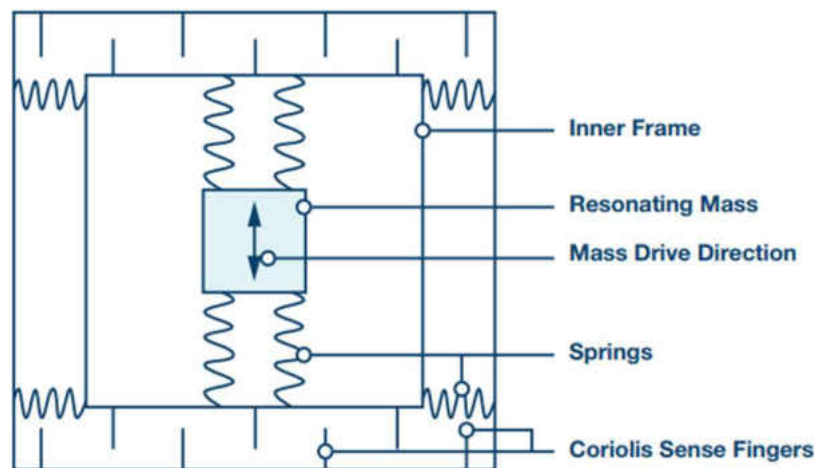


Figure 46: Representation of MEMS Gyroscope [50]

3.4.3 Case Study

To obtain a better understanding how the gyroscope would be used to measure the lead-lag angles of the rotors, an example application was researched. The article “MEMS Gyroscope

Sensors for Wind Turbine Blade Tip Deflection Measurement” was analyzed [51]. This paper discusses mounting a MEMS based gyroscope onto a wind turbine to determine the blade deflection experienced during rotation. Though this study does not directly involve a helicopter rotor, the blade displacement motion measured by the gyroscope is similar to the lead-lag motion experienced by the helicopter rotor later discussed.

The study focusses on utilizing a MEMS based gyroscope coupled with a laser distance sensor to determine the blade deflection experienced by the wind turbine blade during operation. The data from the sensors is coupled using an artificial neural network (ANN) to determine the blade deflection. The inputs into the ANN are the angular rate measurement from the gyroscope in the three dimensions, the turbine yaw angle, and the blade pitch angle from current sensors [51]. The experiment utilizes three ADXRS620 gyroscopes that are mounted orthogonally onto a printed circuit board to capture each axis of the blade. The circuit board is then mounted 20 meters from the blade root and the laser distance finder is mounted 2 meters higher than the blade tip horizon [51]. Once the sensors are positioned on the turbine, the data is collected using an independent data acquisition system known as the down-tower DAQ system. The sensor positioning can be seen in the following figure:

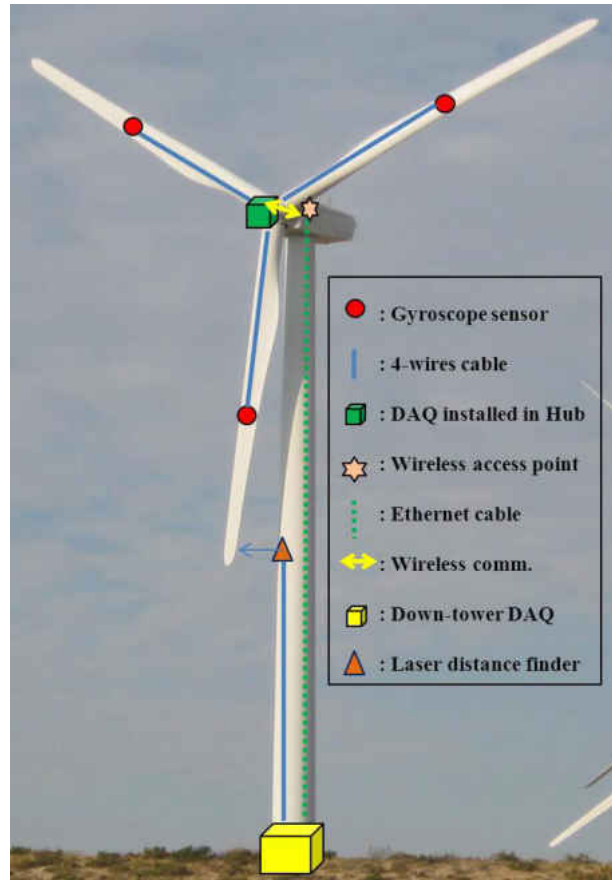


Figure 47: Sensor position on Wind Turbine [51]

Upon data analysis, it was found that the blade tip deflection measurement accuracy was ± 0.4 meters which equates to approximately ± 1.146 degrees. Though the measurement accuracy is fairly large, it proves that the gyroscope will successfully measure the blade deflection directly correlating to the lead-lag measurement of the rotor blade. The large error associated with this experiment is more than likely due to sensor quality rather than testing configuration. Upon further investigation of the sensor being used, it has a larger angle random walk (ARW) value of $0.05 \text{ deg}/\sqrt{hr}$ when compared to the sensor proposed for the new calibration method in a later section. It also does not specify the gyroscope bias, therefore, it is

possible that the lower quality gyroscope is causing the poor accuracy within the measurement. Another study done by Allred et al. utilizes a series of accelerometers and gyroscopes to determine rotorcraft blade position during a flight simulation.

A series of 8 MEMS based accelerometers and 4 MEMS based gyroscopes are used to determine the blade positions. These sensors are placed on a 3D printed puck around the circumference of the circle with 4 pairs of accelerometers opposing each other and a gyroscope is placed between each pair of accelerometers (Figure 48).

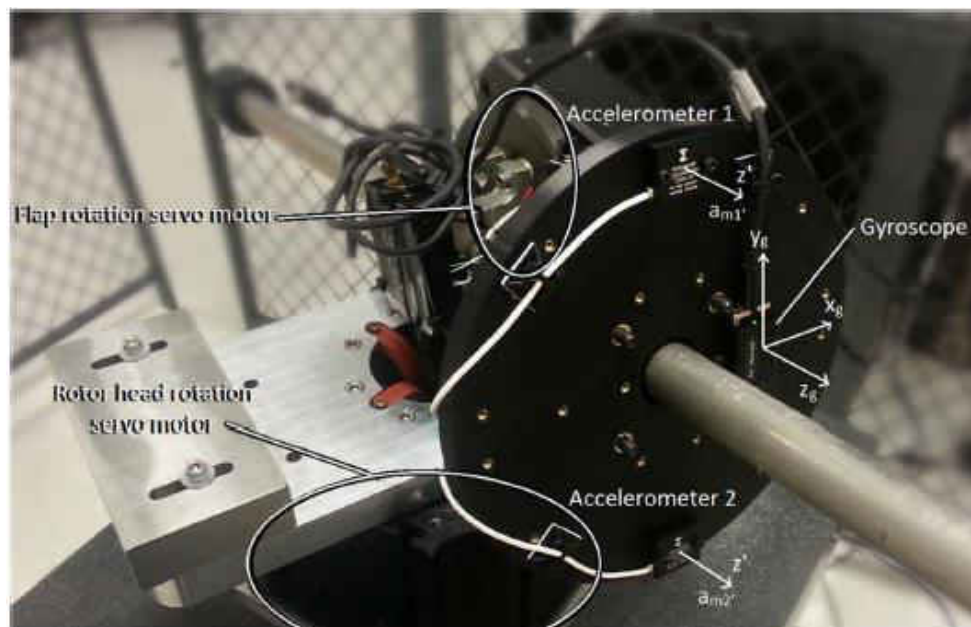


Figure 48: Test stand [52]

The purpose of pairing the accelerometers is to negate the centrifugal force of the spinning hub so that the blade angles are the measurement concentration [52]. The data from the sensors are collected and an artificial neural network (ANN) is used to translate the sensor output to

angle measurement. A series of servo motors are used to control the blade position during rotation and provide blade angle positions in the following manner:

- Pitch: 0 to 20 degrees
- Flap: -1 to 9 degrees
- Lag: 3 to 5 degrees

After concluding the test, it was found that using a single-output ANN is superior to a three-output ANN translating the data. A summary of the results can be seen in the following table:

	Three-Output ANN (%FS)	Single-Output ANN (%FS)	Three (deg)	Single (deg)
Pitch	1.57	0.72	0.314	0.144
Flap	1.03	0.80	0.103	0.08
Lead-Lag	7.76	6.23	0.1552	0.1246

Table 43: Test results [52]

Based on the results of the two studies, it can be seen that sensor choice and application has a key role in measurement accuracy. However, the results from the two studies show that the application of a gyroscope can be successfully used to measure blade angles. Therefore, the gyroscope is determined to be a contender when deciding what sensor type to use when applying the new calibration method.

CHAPTER 4

UNCERTAINTY ANALYSIS

The literature review revealed several methods for calibrating the pitch, flap, and lead-lag angles including a laser tracker, photogrammetry equipment, coordinate measurement machine (CMM), and an inertial measurement unit (IMU). These four methods would allow the calibration to be conducted in a timely and accurate manner, staying within the desired ± 0.1 degree tolerance. To ensure each calibration technique would produce results that fall within these tolerances, an uncertainty analysis was conducted.

4.1 Propagation of Error

The method of propagation of error was used to define the uncertainties associated with each calibration method being evaluated. This method is defined as the “Statistical Tolerance” within the engineering world in which it focuses on how a component within a system is behaviorally related to the system as a whole [553]. This process involves identifying each component of the system that contributes to the overall error and summing them together to determine the total error of the system being evaluated. The propagation of error theory can be derived using a second order Taylor series expansion assuming the variables within the system are statistically independent [54]. To aid in understanding this method let the system be defined as follows:

$$Y = f(x_1, x_2, \dots, x_n) \quad (1)$$

Since each component within the defined system is independent, the system can be broken up into separate independent systems when applying the Taylor series. Assuming this, the

second order expansion term is derived by summing the first derivative of each component and squaring it. This value is then multiplied by the variance associated with it to give the total expanded term [54].

$$\sigma_Y^2 = \sum_{i=1}^n \left(\frac{\partial f(x)}{\partial x_i} \right)^2 * \sigma_{x_i}^2 + \text{higher order terms} \quad (2)$$

The variance associated with the measured values are broken into two classifications: systematic error (B_r) and random error (P_r) [55]. The systematic error is the error characteristic of the system that remains constant while the random error is typically distributed normally and due to chance [61]. Therefore, when applying the propagation of error the method must analyze each contribution separately.

$$B_r = \sqrt{\sum_{i=1}^n \left(\frac{\partial f(x)}{\partial x_i} \right)^2 * \sigma_{B_i}^2} \quad (3)$$

$$P_r = \sqrt{\sum_{i=1}^n \left(\frac{\partial f(x)}{\partial x_i} \right)^2 * \sigma_{P_i}^2} \quad (4)$$

The final step is to take the square root of the sum of the two types of variance associated with the system to find the total uncertainty:

$$U_{total} = \sqrt{B_r^2 + P_r^2} \quad (5)$$

4.1.1 Laser Tracker

The first calibration method evaluated was the laser tracker, specifically focusing on the Leica AT960 laser tracker. This laser tracker would be placed at a determined distance away from the rotor hub and used to track the motion of the blade. Once the laser tracker is placed, three reference points must be attached for the laser tracker to read. These three points will define the plane on which the blade lies with respect to the rotor hub. Two reference points will be placed on the top edge of each blade with the other adjacent to it. The third reference point will then be placed on the center of the hub. Once these three points are acquired, two vectors can be formed using the hub reference point as the origin of the two vectors. The cross product can then be taken to determine the axis of rotation of the blade seen in Figure 49. If needed, a confirmation point can be added to verify the accuracy of the newly defined hub coordinate system.

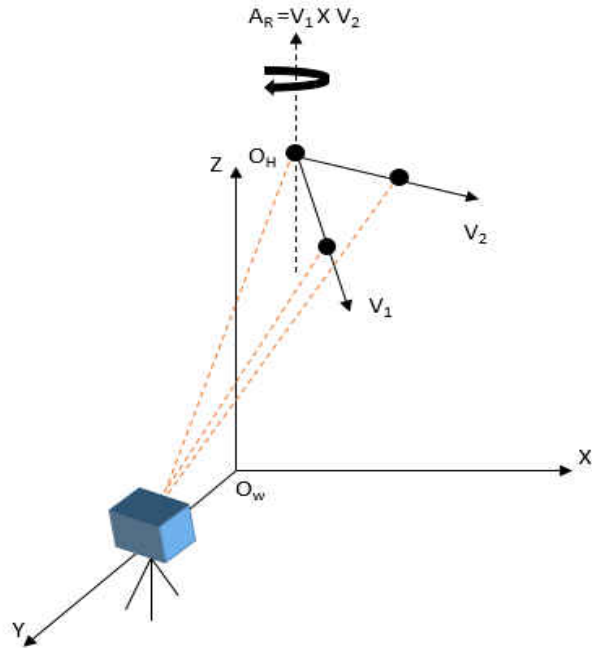


Figure 49: Hub coordinate system defined by laser tracker

Once the hub coordinate system is defined, a target would be placed on the blade for the laser tracker to follow. The blade would then be moved through its range of motion and data would be collected. However, post processing of the data must be done to acquire the correct angles being expressed by the blade throughout its motion. Since the laser tracker is defined as being in the world coordinate system and the target is defined in the hub coordinate system, a coordinate transformation must be done to properly determine the incremental change in the blade angles seen in Figure 50.

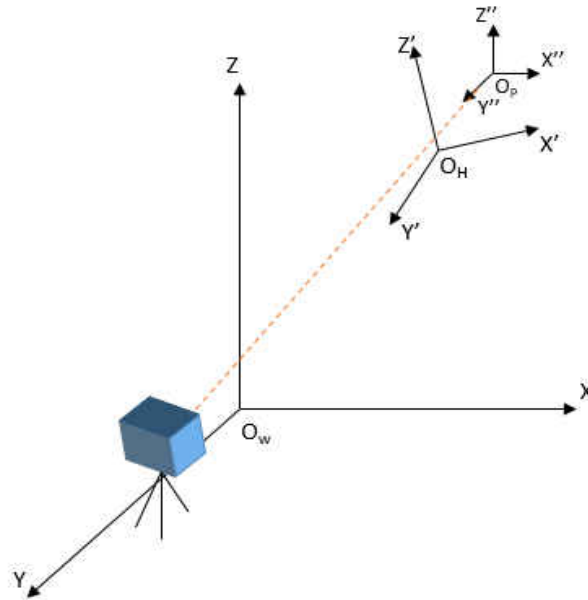


Figure 50: Defined coordinate system of laser tracker and target

This transformation from the world coordinate system to the blade coordinate system can be done using the method of Euler angles or quaternions [56]. For simplicity, the method of Euler angles will be used and the angle transformations can be seen in Figure 51.

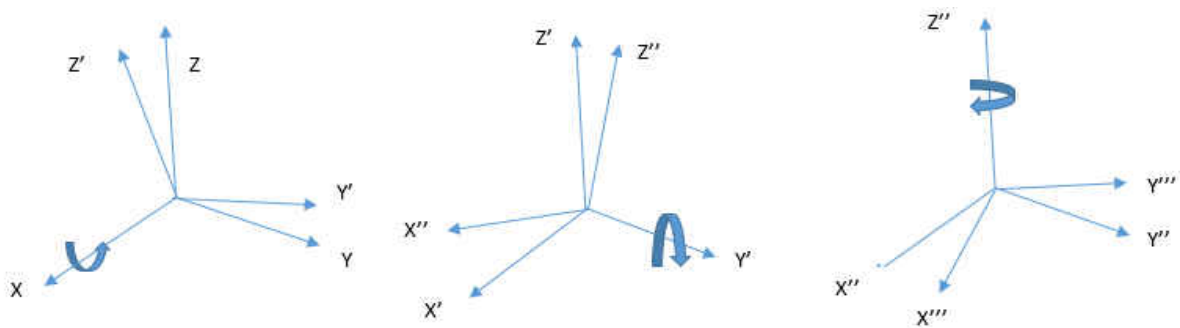


Figure 51: Rotation visual from local to world coordinate system

The rotation sequence being used is the XYZ sequence, meaning that the system will first be rotated about the X-axis, then the Y-axis, and finally about the Z-axis [57]. The rotation sequence is directly related to the yaw (ψ), pitch (θ), and roll (ϕ) of the system, therefore, these values are used to generate the rotation matrix. These rotation matrices are then applied to the coordinates to fully transform the local coordinates to the world coordinates. Following the XYZ sequence, the first rotation matrix is applied to the coordinates corresponding to the rotation about the x-axis:

$$\begin{bmatrix} X' \\ Y' \\ Z' \end{bmatrix} = \begin{bmatrix} 1 & 0 & 0 \\ 0 & \cos(\phi) & \sin(\phi) \\ 0 & -\sin(\phi) & \cos(\phi) \end{bmatrix} \begin{bmatrix} X \\ Y \\ Z \end{bmatrix} \quad (6)$$

Once the point is rotated about the x-axis, the point is then rotated about the y-axis:

$$\begin{bmatrix} X'' \\ Y'' \\ Z'' \end{bmatrix} = \begin{bmatrix} \cos(\theta) & 0 & -\sin(\theta) \\ 0 & 1 & 0 \\ \sin(\theta) & 0 & \cos(\theta) \end{bmatrix} \begin{bmatrix} X' \\ Y' \\ Z' \end{bmatrix} \quad (7)$$

After the rotation about the y-axis, the point is rotated about the z-axis to complete the transformation:

$$\begin{bmatrix} X''' \\ Y''' \\ Z''' \end{bmatrix} = \begin{bmatrix} \cos(\psi) & \sin(\psi) & 0 \\ -\sin(\psi) & \cos(\psi) & 0 \\ 0 & 0 & 1 \end{bmatrix} \begin{bmatrix} X'' \\ Y'' \\ Z'' \end{bmatrix} \quad (8)$$

After defining how the system will work and the world coordinates will be generated, the uncertainty analysis was conducted focusing on the three dimensional output from the laser tracker. The X, Y, and Z components of the tracker will be defined in the following manner based on determining a point position in 3D space (Figure 52):

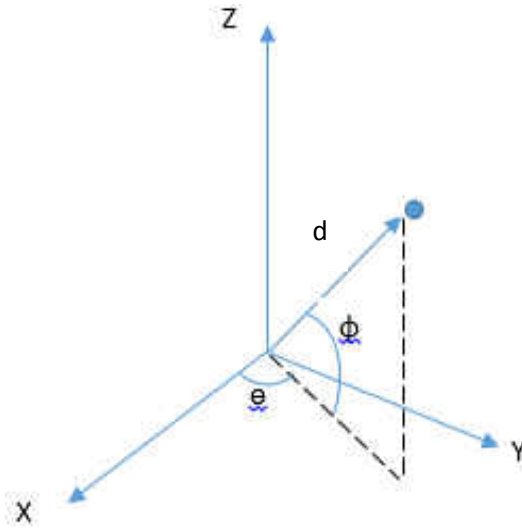


Figure 52: 3D point in space

$$X = d * \cos(\theta) * \sin(\Phi) \quad (9)$$

$$Y = d * \sin(\theta) * \sin(\Phi) \quad (10)$$

$$Z = d * \cos(\Phi) \quad (11)$$

Note that d corresponds to the distance from the target, θ corresponds to the azimuth angle, and Φ corresponds to the elevation angle of the rotor blade. The partial derivative of each dimension is then taken with respect to the distance, azimuth, and elevation angle of the blade.

Partial derivatives of X:

$$\frac{\partial X}{\partial d} = \cos(\theta) \sin(\Phi) \quad (12)$$

$$\frac{\partial X}{\partial \theta} = -d * \sin(\theta) \sin(\Phi) \quad (13)$$

$$\frac{\partial X}{\partial \Phi} = d * \cos(\theta) \cos(\Phi) \quad (14)$$

Partial derivatives of Y:

$$\frac{\partial Y}{\partial d} = \sin(\theta) \sin(\Phi) \quad (15)$$

$$\frac{\partial Y}{\partial \theta} = (d * \cos(\theta) \sin(\Phi)) \quad (16)$$

$$\frac{\partial Y}{\partial \Phi} = \sin(\theta) \cos(\Phi) \quad (17)$$

Partial derivatives of Z:

$$\frac{\partial Z}{\partial d} = \cos(\Phi) \quad (18)$$

$$\frac{\partial Z}{\partial \theta} = 0 \quad (19)$$

$$\frac{\partial Z}{\partial \Phi} = -d * \sin(\Phi) \quad (20)$$

Since there are no systematic uncertainties associated with the current analysis, only random uncertainty will be considered. Therefore, once the partial derivatives are taken, the results are applied to equation (3) and become:

$$\delta X = \sqrt{(\cos(\theta) \sin(\Phi) \sigma_d)^2 + (-d * \sin(\theta) \sin(\Phi) \sigma_\theta)^2 + (d * \cos(\theta) \cos(\Phi) \sigma_\Phi)^2} \quad (21)$$

$$\delta Y = \sqrt{(\sin(\theta) \sin(\Phi) \sigma_d)^2 + (d * \cos(\theta) \sin(\Phi) \sigma_\theta)^2 + (\sin(\theta) \cos(\Phi) \sigma_\Phi)^2} \quad (22)$$

$$\delta Z = \sqrt{(\cos(\Phi) \sigma_d)^2 + (-d * \sin(\Phi) \sigma_\Phi)^2} \quad (23)$$

The total uncertainty for the laser tracker is then calculated by taking the sum of squares of the uncertainties in the X, Y, and Z axis. This is done in the following manner:

$$U_{meter} = \sqrt{\delta X^2 + \delta Y^2 + \delta Z^2} \quad (24)$$

The total uncertainty is given in the units of meters, however, the focus of this analysis is to define the uncertainties associated with the blade angles of the rotor. Therefore, the total uncertainty is converted from meters to degrees providing there is a defined distance from the measured target to the laser tracker seen in Figure 53. This conversion is done in the following manner:

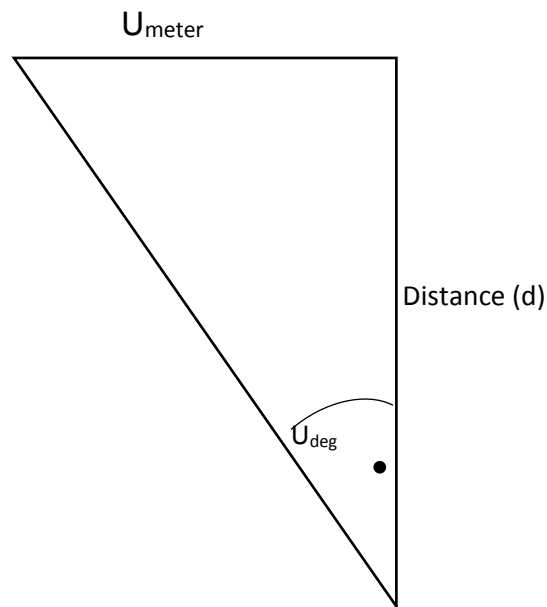


Figure 53: Representation of conversion from meters to degrees

$$U_{deg} = \tan^{-1}\left(\frac{U_{meter}}{\text{target distance } (d)}\right) \quad (25)$$

The analysis is then conducted given the following assumptions based on calculation simplicity and manufacturer specifications:

- The laser tracker is on the same plane as the rotor
- The rotor is at zero reference (flap and lag angles at zero)
- The tracker is placed 5 meters from the target
- The distance error is 0.0000005 meters
- The flap angle and lag angle error is 0.000015 meters + 0.000006 meters * distance

With the assumptions made and the manufacture specifications defined, the total uncertainty associated with the laser tracker was found to be $7.58E-7$ degrees. Distance was found to be the driving factor for the uncertainty of the laser tracker as seen in Figure 54.

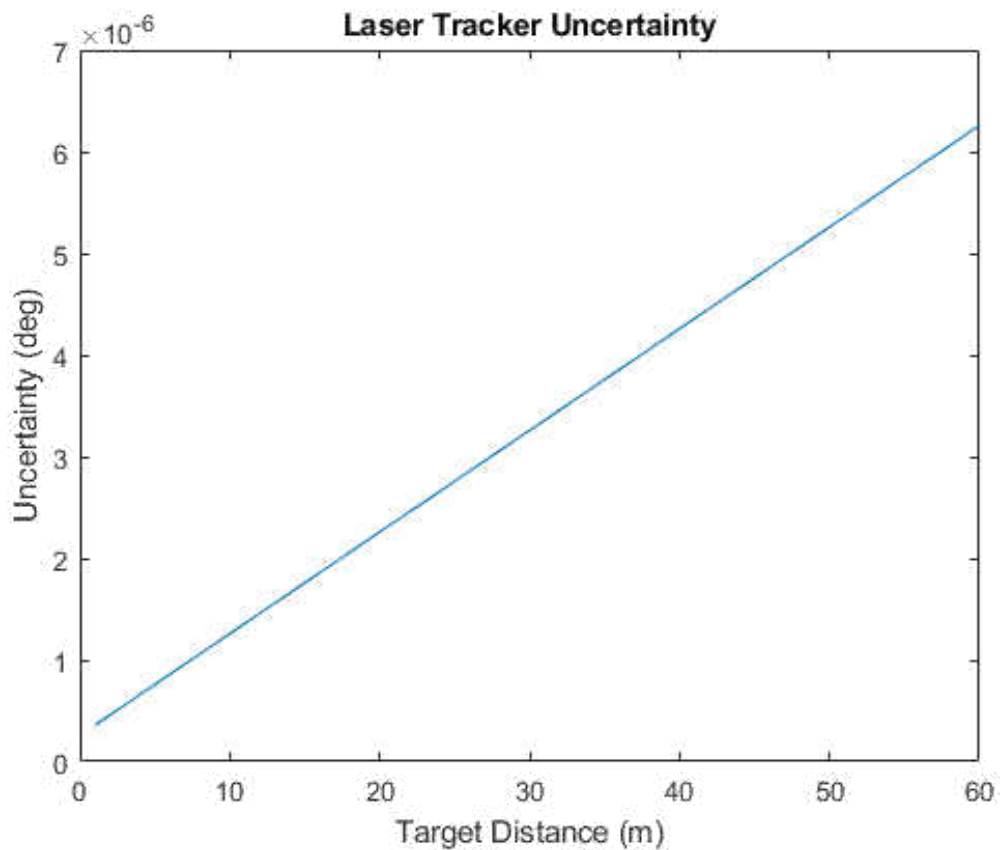


Figure 54: Graph representing laser tracker uncertainty driving factor

4.1.2 Stereo Vision Camera

The next method of calibration being evaluated for its uncertainty is the system utilizing photogrammetric techniques, specifically the use of an Optotrak Certus. This system is similar to the laser tracker for the rotor plane must be defined in the same way using 3 reference points. The cross product of the two vectors is taken and the rotation axis is defined. Once the hub reference system is defined, the Optotrak tracks the target as it moves through its full range of motion. The data is then transformed from the hub reference frame to the world reference frame similarly to the laser tracker and the delta angles are determined. Since the Optotrak uses the method of triangulation, there is no need to use Euler angles or quaternions to define the calculated angles from the 3D coordinates. This method of calibration is illustrated in Figure 55.

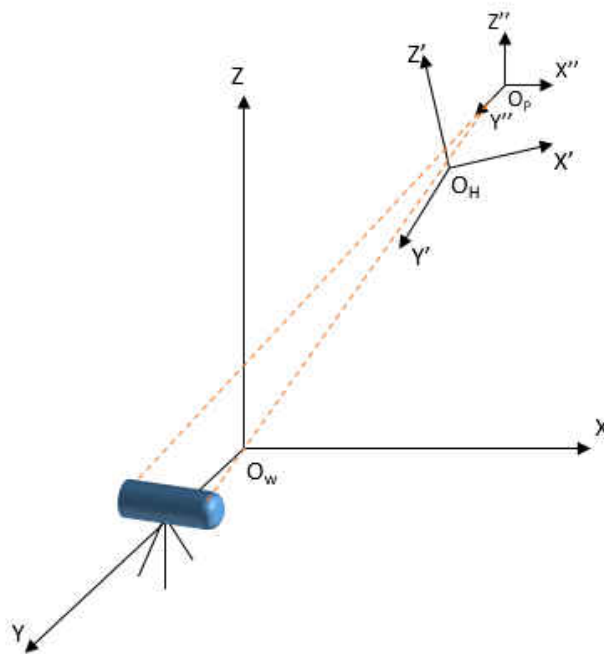


Figure 55: Optotrak with respect to hub and world coordinate system

The Optotrak system will be modeled as a stereo optic system being analyzed using the pinhole method. A pinhole camera is defined as a camera that has no lens, therefore, they produce an image using the principle of rectilinear theory of light [58]. Essentially this is relying on the light traveling in a straight line. The camera is comprised of a dark box containing a small hole in the middle where the light enters. When the light enters the hole, the image is projected onto the back of the box in an inverted manner. The hole size plays a role in picture quality, meaning that if the hole is too small the picture may become distorted due to the light scattering at the edges [58]. Since the pinhole method is being used, there is no need to account for any type of lens distortion during the evaluation [59]. The analysis of the photogrammetric system follows [60] closely, therefore refer to the reference for further detail. The evaluation system is comprised of determining the relationship of the world coordinate system to the camera coordinate system seen in Figure 56.

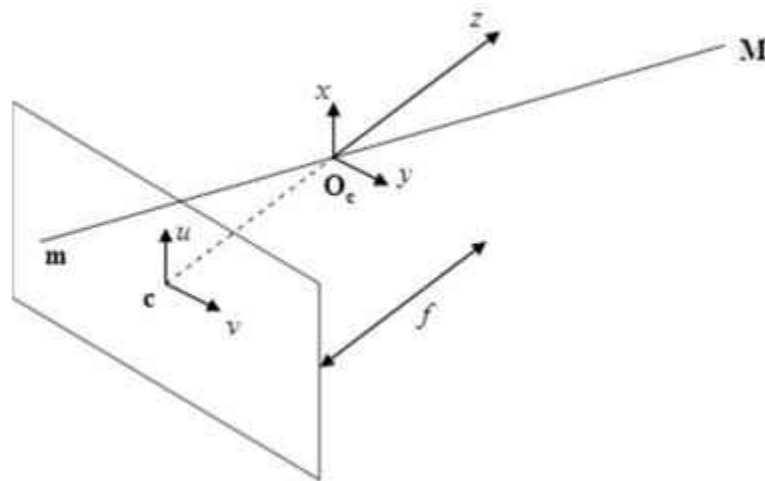


Figure 56: Representation of World Vs Camera Coordinate System [60]

Since the point is in the world coordinate system, the point must be projected onto the image plane of the camera. To simplify the camera model, the following assumptions will be made:

- The principal point is exactly on center
- The pixels are perfectly square
- The skewness (distortion between pixels) will be neglected

Applying these assumptions, where the variables are the target distance (d), focal length (f), viewing angle (γ), and the pixel coordinates for camera one (u_1, v_1) and camera two (u_2 and v_2), the following projection matrix is formed for the first camera [60]:

$$\begin{bmatrix} U \\ V \\ S \end{bmatrix} = \begin{bmatrix} -f & 0 & 0 & 0 \\ 0 & -f & 0 & 0 \\ 0 & 0 & 1 & 0 \end{bmatrix} \begin{bmatrix} x \\ y \\ z \\ t \end{bmatrix} \quad (263)$$

The basic projection of the 3D world points onto the 2D image points is done in the following manner where S is defined as the projection of the image plane, u , onto the world plane, U [60]:

$$u = \frac{U}{S} \quad (27)$$

$$v = \frac{V}{S} \quad (28)$$

Once the projection matrix for the first camera is defined, the second camera is evaluated. There are two reference points during this calculation, the left camera frame and the right camera frame. For this evaluation, the left camera frame will be analyzed as being true and the right camera frame will be projected onto the left camera frame. This will be done using a translational and rotational vector. Before the projection can be applied, the orientation of the cameras must be defined. The left and right cameras will be oriented in the XZ plane and rotated

about the y-axis [66] (Figure 6). Therefore the rotation matrix (R) and the right camera position matrix (P_R) become:

$$R = \begin{bmatrix} \cos(\gamma) & 0 & \sin(\gamma) \\ 0 & 1 & 0 \\ -\sin(\gamma) & 0 & \cos(\gamma) \end{bmatrix} \quad (29)$$

$$P_R = \begin{bmatrix} d * \sin(\gamma) \\ 0 \\ d - d * \cos(\gamma) \end{bmatrix} \quad (304)$$

The two matrices are then multiplied together to translate the world coordinates seen in the right camera frame onto the left camera frame. Once this is achieved, the next step is to combine the world coordinate transformations from the right and left camera, matrix T, and project them onto the image plane of the two cameras. This is done in the following manner [60]:

$$T = \begin{bmatrix} \cos(\gamma) & 0 & \sin(\gamma) & -\sin(\gamma) * (d - d * \cos(\gamma)) - d \cos(\gamma) \sin(\gamma) \\ 0 & 1 & 0 & 0 \\ -\sin(\gamma) & 0 & \cos(\gamma) & d * \sin(\gamma)^2 - \cos(\gamma) * (d - d * \cos(\gamma)) \\ 0 & 0 & 0 & 1 \end{bmatrix} \quad (31)$$

$$\begin{bmatrix} U \\ V \\ S \end{bmatrix} = \begin{bmatrix} -f & 0 & 0 & 0 \\ 0 & -f & 0 & 0 \\ 0 & 0 & 1 & 0 \end{bmatrix} [T] \begin{bmatrix} x \\ y \\ z \\ t \end{bmatrix} \quad (32)$$

As mentioned earlier, the stereo vision camera is being solved using the method of triangulation to determine the 3D coordinates. Therefore, the coordinates are solved in a linear fashion using the following equation [60]:

$$AX = 0 \quad (33)$$

where

$$A = \begin{bmatrix} u_1 P_1^{3T} - P_1^{1T} \\ v_1 P_1^{3T} - P_1^{2T} \\ u_2 P_2^{3T} - P_2^{1T} \\ v_2 P_2^{3T} - P_2^{2T} \end{bmatrix} \quad (34)$$

The superscripts in equation A refer to the row of the camera matrix T and the subscripts refer to the left and right camera. The subscript 1 refers to the left camera and the subscript 2 refers to the right camera [60]. Due to the size of matrix A, it will not be shown. The solution to the linear equation solving for the XYZ coordinates becomes [66]:

$$X = \frac{du_1(u_2 - f \sin(\gamma) - u_2 \cos(\gamma))}{(u_1 u_2 + f^2) \sin(\gamma) + f(u_2 - u_1) \cos(\gamma)} \quad (35)$$

$$Y = \frac{dv_2(u_1 + f \sin(\gamma) - u_1 \cos(\gamma))}{(u_1 u_2 + f^2) \sin(\gamma) + f(u_2 - u_1) \cos(\gamma)} \quad (36)$$

$$Z = \frac{fd(u_2 - f \sin(\gamma) - u_2 \cos(\gamma))}{(u_1 u_2 + f^2) \sin(\gamma) + f(u_2 - u_1) \cos(\gamma)} \quad (37)$$

The theory of propagation of error can then be applied to these equations to determine the measurement uncertainty of the camera system. The variances associated with the camera will be modeled as systematic for the focal length and target distance, while the rest will be modeled as random. To begin, the partial derivatives of each coordinate position are taken with respect to each variable within the equations. Due to the size of each partial derivative of the X, Y, and Z components, only the partial derivatives associated with the random variables of the X-axis will be shown. However, the other two are taken in a similar manner.

$$\frac{\partial X}{\partial u_1} = \frac{-df(f^2 \sin(\gamma)^2 + 2fu_2 \cos(\gamma) \sin(\gamma) - fu_2 \sin(\gamma) + u_2^2 \cos(\gamma)^2 - u_2^2 \cos(\gamma)^2)}{(f^2 \sin(\gamma) - fu_1 \cos(\gamma) + fu_2 \cos(\gamma) + u_1 u_2 \sin(\gamma))^2} \quad (38)$$

$$\frac{\partial X}{\partial u_2} = \frac{dfu_1(u_1 - u_1 \cos(\gamma) + f \sin(\gamma))}{(f^2 \sin(\gamma) - fu_1 \cos(\gamma) + fu_2 \cos(\gamma) + u_1 u_2 \sin(\gamma))^2} \quad (39)$$

$$\frac{\partial X}{\partial d} = \frac{u_1(u_2 \cos(\gamma) - u_2 + f \sin(\gamma))}{f^2 \sin(\gamma) - fu_1 \cos(\gamma) + fu_2 \cos(\gamma) + u_1 u_2 \sin(\gamma)} \quad (40)$$

$$\frac{\partial X}{\partial f} = \frac{du_1(\cos(\gamma) - 1)(u_2^2 \cos(\gamma) + u_1 u_2 - f^2 - f^2 \cos(\gamma) + 2f u_2 \sin(\gamma))}{(f^2 \sin(\gamma) - f u_1 \cos(\gamma) + f u_2 \cos(\gamma) + u_1 u_2 \sin(\gamma))^2} \quad (41)$$

$$\frac{\partial X}{\partial \gamma} = \frac{du_1(f^2 u_1 + u_1 u_2^2 - f^2 u_2 \cos(\gamma) - u_1 u_2^2 \cos(\gamma) + f u_2^2 \sin(\gamma) - f u_1 u_2 \sin(\gamma))}{(f^2 \sin(\gamma) - f u_1 \cos(\gamma) + f u_2 \cos(\gamma) + u_1 u_2 \sin(\gamma))^2} \quad (42)$$

Once the partial derivatives are taken, the random uncertainties are applied to the derivatives to determine the uncertainty of each coordinate position in a similar fashion to the laser tracker discussed previously. The sum of squares of the three coordinate position uncertainties are then taken to determine the total uncertainty of the 3D coordinate position associated with the camera position:

$$U_{camera(m)} = \sqrt{\delta X^2 + \delta Y^2 + \delta Z^2} \quad (43)$$

The analysis is then conducted given the following assumptions and uncertainty specifications:

Variable	Estimated True Value	Random Uncertainty	Systematic Uncertainty
Left pixel coordinate(u_1)	0	0.68E-6 (m)	0
Right pixel coordinate (u_2)	0	0.68E-6 (m)	0
Left pixel coordinate (v_1)	0	0.68E-6 (m)	0
Right pixel coordinate (v_2)	0	0.68E-6 (m)	0
Target Distance (d)	1.5, 7 (m)	0	24E-9 (m)
Focal Length (f)	30, 50, 70 (mm)	0	24E-9 (m)
Camera angle (γ)	30, 40, 50 (deg)	1.3889E-6 (deg)	0

Table 44: Estimated Values and their uncertainty

Note, the uncertainties given to each variable come from [60] since the Optotrak Certus data sheet does not provide these values. Also, according to the Optotrak Certus data sheet the

working distance for the camera is a minimum of 1.5 meters and a maximum of 7 meters.

Therefore, the analysis includes both distances to capture the minimum and maximum error the Optotrak Certus is capable of. With a focal length of 40 mm a viewing angle of 30 degrees, and a distance of 1.5 meters, the camera system achieves an uncertainty of 0.0721 mm which is very close to the claimed 0.1 mm accuracy of the sensor. However, when the distance is increased to 7 meters the uncertainty increases to 0.4488 mm meaning that target distance plays a role in measurement uncertainty. Another trend found was that the uncertainty was determined by the focal length of the camera. The ideal focal length was found to be around 30 mm with an increase of uncertainty as you increased or decreased the focal length from the ideal 30 mm. Lastly, the verge angle (ψ) played a key role in determining the uncertainty of the system. As the verge angle (ψ) decreased and the viewing angle increased (γ), the overall system uncertainty decreased. This trend is caused by the error ellipse from the triangulation method becoming smaller as the verge angle of the cameras decrease [60]. The following figure below represents the trends found during this analysis:

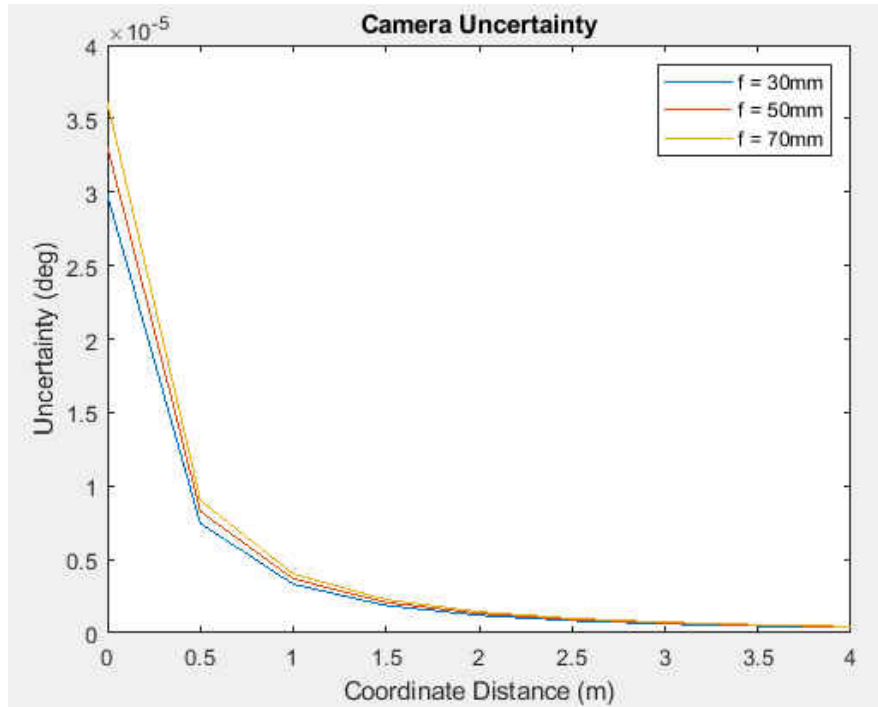


Figure 57: Uncertainty trend of Optotrak Certus

4.1.3 Coordinate Measurement Arm

The method of using a CMM will now be evaluated with a focus on using a Faro Arm Quantum E VS 2.5m 7-axis. This system uses 7 angle encoders within the faro arm to determine the distance and angle associated with each recorded point. To obtain the desired angles, the CMM will be mounted on the rotation axis of the hub using a temporary mounted base. A calibration plate will then be attached to the blade with three measurement points. The Faro arm is then be calibrated and the rotor plane will be defined in a similar manner to the laser tracker and photogrammetric system. Once calibrated, the blade will be moved through its range of motion and data points will be taken using the probe tip of the Faro arm. With the measurement process defined, the uncertainty analysis is conducted to ensure proper measurement tolerances.

Two factors influence the uncertainty associated with the use of the Faro arm: the distance measurement and the encoder angle measurement [61]. The uncertainty associated with the distance measurement was defined by using the distance formula between two 3-D points seen in Figure 58 and equation 8.

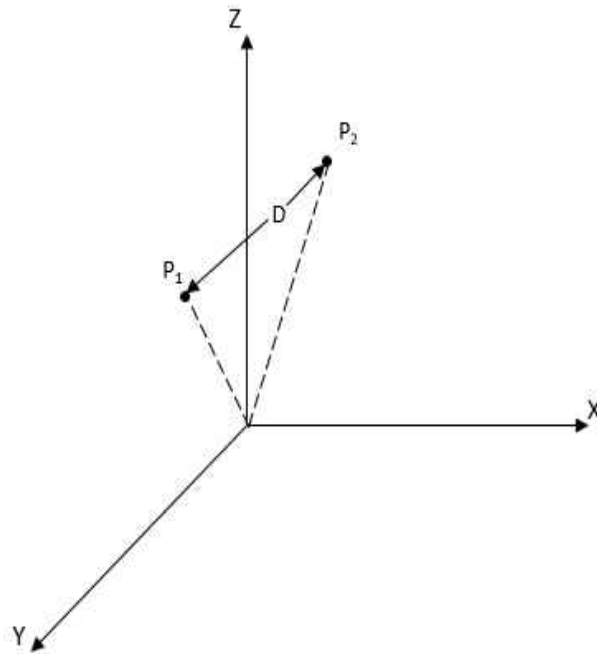


Figure 58: Distance between two 3D points

$$d = \sqrt{(X_2 - X_1)^2 + (Y_2 - Y_1)^2 + (Z_2 - Z_1)^2} \quad (44)$$

The partial derivatives with respect to the distance equation and its variables are taken presented in the following manner:

$$\frac{\partial d}{\partial X_1} = \frac{(X_1 - X_2)}{\sqrt{(X_2 - X_1)^2 + (Y_2 - Y_1)^2 + (Z_2 - Z_1)^2}} \quad (45)$$

$$\frac{\partial d}{\partial Y_1} = \frac{(Y_1 - Y_2)}{\sqrt{(X_2 - X_1)^2 + (Y_2 - Y_1)^2 + (Z_2 - Z_1)^2}} \quad (46)$$

$$\frac{\partial d}{\partial Z_1} = \frac{(Z_1 - Z_2)}{\sqrt{(X_2 - X_1)^2 + (Y_2 - Y_1)^2 + (Z_2 - Z_1)^2}} \quad (47)$$

$$\frac{\partial d}{\partial X_2} = \frac{-(X_1 - X_2)}{\sqrt{(X_2 - X_1)^2 + (Y_2 - Y_1)^2 + (Z_2 - Z_1)^2}} \quad (48)$$

$$\frac{\partial d}{\partial Y_2} = \frac{-(Y_1 - Y_2)}{\sqrt{(X_2 - X_1)^2 + (Y_2 - Y_1)^2 + (Z_2 - Z_1)^2}} \quad (49)$$

$$\frac{\partial d}{\partial Z_2} = \frac{-(Z_1 - Z_2)}{\sqrt{(X_2 - X_1)^2 + (Y_2 - Y_1)^2 + (Z_2 - Z_1)^2}} \quad (50)$$

After taking the partial derivatives, the theory of propagation of error is applied and each derivative is multiplied by its associated variance and squared. For this model, only random error will be evaluated based on the uncertainty of the measured components from the Faro Arm datasheet. The following equation represents the uncertainty in distance measurement between two points in space in condensed form:

$$U_d = \sqrt{\frac{(X_2 - X_1)^2(X_1\sigma_x + X_2\sigma_x)^2 + (Y_2 - Y_1)^2(Y_1\sigma_y + Y_2\sigma_y)^2 + (Z_2 - Z_1)^2(Z_1\sigma_z + Z_2\sigma_z)^2}{(X_2 - X_1)^2 + (Y_2 - Y_1)^2 + (Z_2 - Z_1)^2}} \quad (51)$$

Since there was little information on the Faro Arm Quantum being evaluated in terms of the uncertainty associated with the measurement capability, the specifications from the Faro Gage Arm were used. Therefore, the specifications of the X, Y, and Z components are as follows [62]:

- Error in X (σ_x): 0.000005 m + (working distance) * 0.000008 m/ meter

- Error in Y (σ_Y): $0.000005 \text{ m} + (\text{working distance}) * 0.000008 \text{ m/ meter}$
- Error in Z (σ_Z): $0.000005 \text{ m} + (\text{working distance}) * 0.000008 \text{ m/ meter}$

Using these specifications and the assumption that the arm is on the same plane as the rotor at a working distance of 1.5 meters, the distance uncertainty was calculated to be $3.40\text{E-}5$ meters with a trend of uncertainty increasing as the distance increases seen in Figure 59.

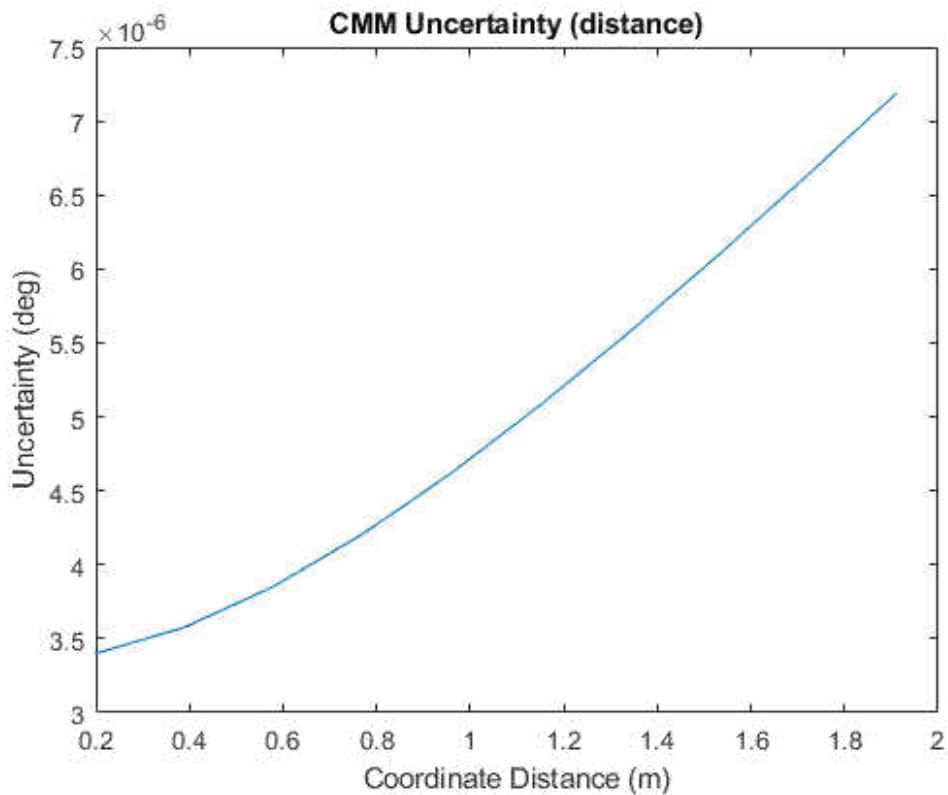


Figure 59: Distance Uncertainty Trend

To keep the units consistent, the uncertainty of the distance needs to be converted to the units of degrees. This is done in a similar manner to the laser tracker and Optotrak (Figure 3).

$$U_d = \tan^{-1}\left(\frac{U_{meter}}{\text{target distance}}\right) \quad (52)$$

Therefore the uncertainty transformation given a working distance of 1.5 meters becomes 1.97E-5 degrees.

Once the distance uncertainty is modeled, the focus can shift to evaluating the uncertainty associated with the vector angles measured by the Faro Arm. To simplify the uncertainty model, the two vectors will be assumed to be on the same plane (Y and Z coordinate are the same) as each other. This method involves calculating the angle between two vectors formed about the same axis of rotation as seen in Figure 60.

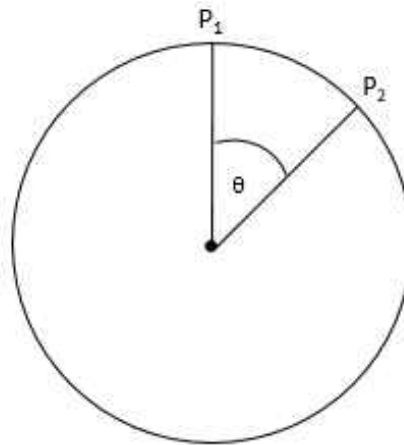


Figure 60: Cosine method to determine angle between 2 vectors

$$\text{Cos}(\theta) = \frac{\vec{V}_1 \cdot \vec{V}_2}{\|\vec{V}_1\| \cdot \|\vec{V}_2\|} \quad (53)$$

For the method of cosines to be applied, three points must be generated to form an angle between the two vectors. Therefore, P_1 will be defined as (X_1, Y_1, Z_1) , P_2 will be defined as (X_2, Y_2, Z_2) , and P_0 will be the origin of the circle at (X_3, Y_3, Z_3) . Now that the three points are defined, vectors 1 and 2 can be generated and V_1 becomes $(X_1 - X_3, Y_1 - Y_3, Z_1 - Z_3)$ while V_2 becomes $(X_2 - X_3, Y_2 - Y_3, Z_2 - Z_3)$. The propagation of error theory is then applied and the partial derivatives are taken with respect to each component of the system. Due to the length of the partial derivatives and derived data reduction equation it will not be presented, therefore, refer to the appendix for the MATLAB script to review these calculations. It was found that as the delta angle increased the uncertainty decreased seen in Figure 61.

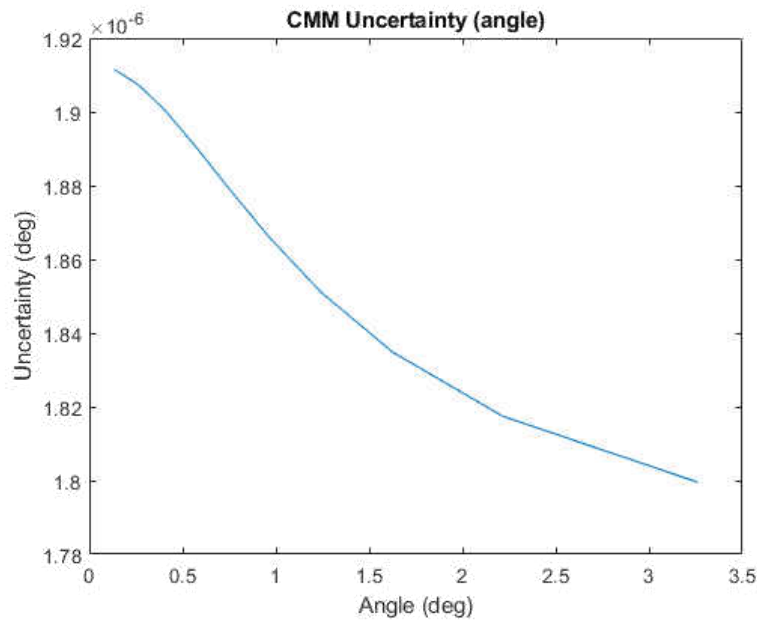


Figure 61: Angle Uncertainty Trend

The uncertainty associated with the angle was found to be 1.91E-6 degrees. After determining the uncertainty associated with the distance and vector angle, the total uncertainty can be found by combining the two.

$$U_{Total} = U_d + U_\theta \quad (54)$$

The two uncertainties are then combined to determine the overall uncertainty of the Faro Arm Quantum found to be 5.31E-5 degrees. Since distance is the driving factor for the uncertainty of the Faro Arm, the overall trend of the uncertainty increases as the distance and delta angle increase seen in Figure 62.

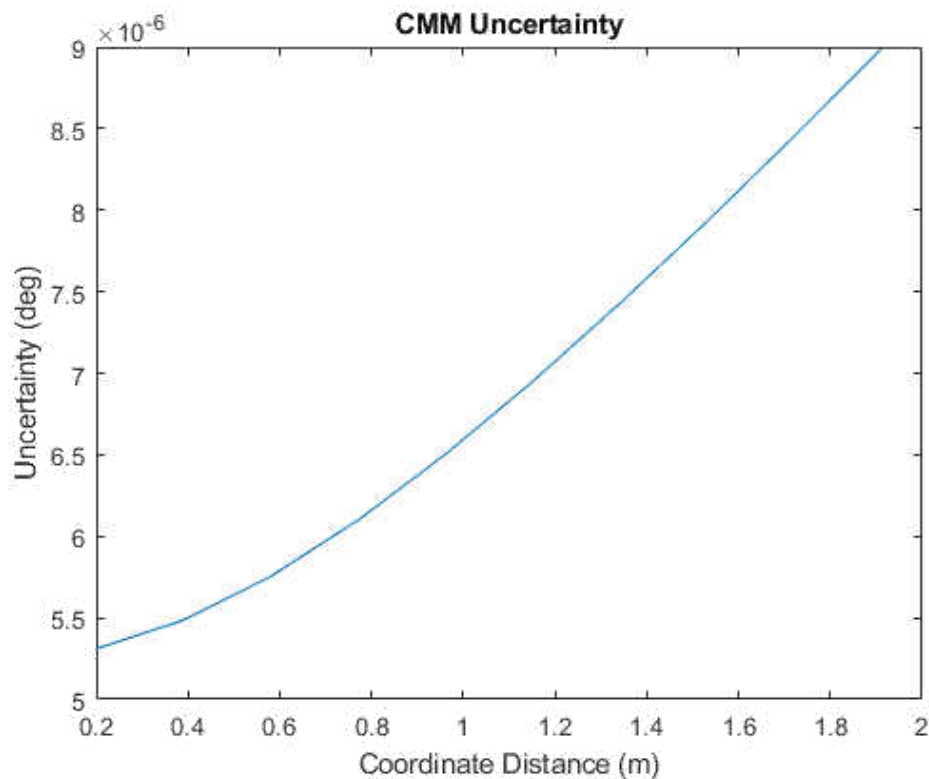


Figure 62: Total Uncertainty of Faro Arm Trend

4.1.4 Gyroscope

The final method evaluated was the use of an IMU with the main focus of analyzing the gyroscope within the measurement unit. The specifications used for this evaluation are obtained from the Honeywell HG4930-CA1 data sheet. This system would consist of mounting the IMU to the fabricated NASA Langley Angle Measurement System (AMS) package mount already in use. With the AMS and IMU package mounted, the pitch and flap angle will be measured by the AMS package and the lead-lag angle will be measured by the IMU. These two sensors combined will allow for a dynamic calibration which will decrease calibration time as well as increase calibration accuracy. Since the AMS package is well documented within the NASA archives, only the IMU package needed to be evaluated. To model the IMU, the method outlined in [63] was largely followed, therefore, more details can be found there. This method models the gyroscope within the IMU as being placed at the latitude it will be used with respect to Earth seen in Figure 63.

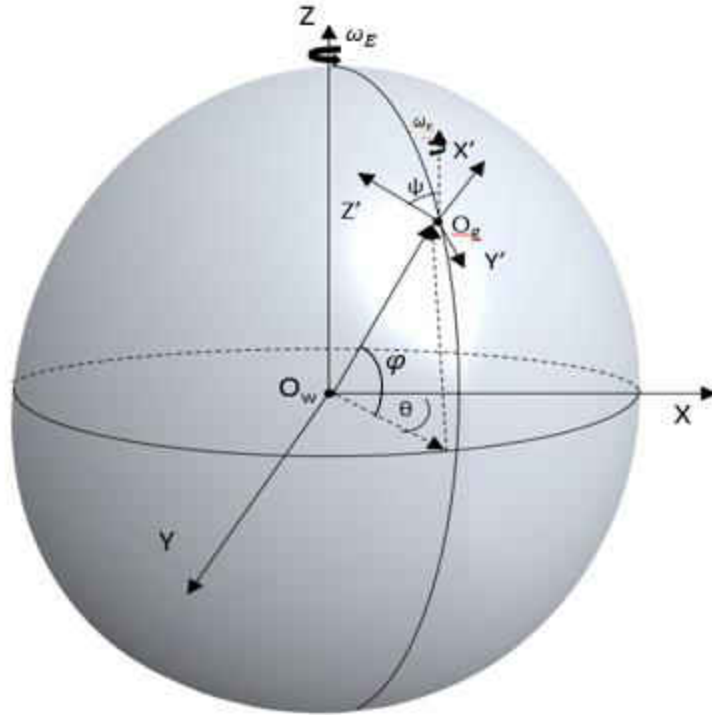


Figure 63: Modeling Gyroscope to Determine Uncertainty

Once the location of the gyro is known with respect to the Earth, the rotation rate of the sensor at the specified latitude, φ , must correspond with the rotation rate, ω_E , of the Earth. This is performed in the following manner:

$$\omega_0 = \begin{bmatrix} 0 \\ \omega_E \cos \varphi \\ \omega_E \sin \varphi \end{bmatrix} \quad (55)$$

Once the gyroscope axis is aligned with the Earth's rotation axis, the right-hand rule can be used to define the rotation matrix of the gyroscope about the Z-axis of the Earth [63].

$$R(\Psi) = \begin{bmatrix} \cos \Psi & -\sin \Psi & 0 \\ \sin \Psi & \cos \Psi & 0 \\ 0 & 0 & 1 \end{bmatrix} \quad (56)$$

The rotation matrix is then applied to the angular velocity of the gyroscope since the Earth's coordinate system is fixed [63], this now defines the angular velocity of the gyroscope with respect to the Earth:

$$\omega_G = \begin{bmatrix} \cos \Psi & -\sin \Psi & 0 \\ \sin \Psi & \cos \Psi & 0 \\ 0 & 0 & 1 \end{bmatrix} \begin{bmatrix} 0 \\ \omega_E \cos \varphi \\ \omega_E \sin \varphi \end{bmatrix} = \begin{bmatrix} -\omega_E \cos \varphi \sin \Psi \\ \omega_E \cos \varphi \cos \Psi \\ \omega_E \sin \varphi \end{bmatrix} \quad (57)$$

The vector W_G is then projected onto the XY-plane of the Earth so that the lag angle can be calculated:

$$\omega_{Gp} = \begin{bmatrix} 1 & 0 & 0 \\ 0 & 1 & 0 \\ 0 & 0 & 0 \end{bmatrix} \begin{bmatrix} -\omega_E \cos \varphi \sin \Psi \\ \omega_E \cos \varphi \cos \Psi \\ \omega_E \sin \varphi \end{bmatrix} = \begin{bmatrix} -\omega_E \cos \varphi \sin \Psi \\ \omega_E \cos \varphi \cos \Psi \\ 0 \end{bmatrix} \quad (58)$$

For calculation simplicity, the reference point of the gyroscope will be aligned with the x-axis offset by the specified Ψ angle [63] seen in Figure 64.

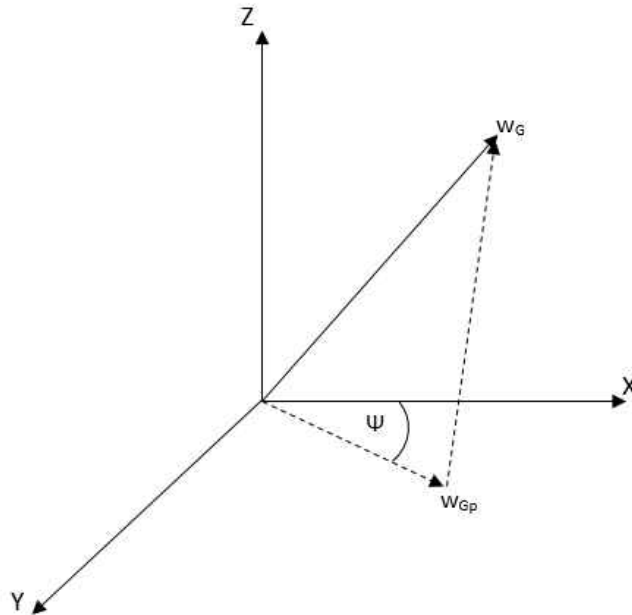


Figure 64: Projection of Gyroscope onto XY-plane

The errors of gyro bias drift and angle random walk (ARW) are then added to model the sensor more accurately. Therefore, the gyroscope velocity projected onto the XY-plane becomes:

$$\omega_{Gp} = \omega_E \cos\varphi \cos\psi + \varepsilon_{bias} + \varepsilon_{ARW} \quad (59)$$

Since desired measured value is the delta angle the gyroscope travels, the angular velocity must be multiplied by time to produce the delta angle seen in the following equation:

$$\theta_G = (\omega_E \cos\varphi \cos\psi + \varepsilon_{bias} + \varepsilon_{ARW}) * time \quad (60)$$

Note, the data reduction equation does not include the turn on bias value and only includes the bias in run instability, ε_{bias} , and the ARW uncertainty, ε_{ARW} . The turn on bias value is not needed for this analysis due to it being a constant known value each time the gyroscope is initialized. During the data analysis, this value is subtracted out to obtain the true measured value. Now that the data reduction equation is formed, the theory of propagation of error can be applied to determine the uncertainty with the gyroscope. Therefore, the partial derivatives of each component with respect to the data reduction equations were taken except with respect to time. Time was neglected due to its minuscule effect on the systems uncertainty.

$$\frac{\partial \theta_G}{\partial \omega_E} = \cos\varphi \cos\psi \quad (61)$$

$$\frac{\partial \theta_G}{\partial \varphi} = -\omega_E \cos(\psi) \sin(\varphi) \quad (62)$$

$$\frac{\partial \theta_G}{\partial \psi} = -\omega_E \cos(\varphi) \sin(\psi) \quad (63)$$

$$\frac{\partial \theta_G}{\partial \varepsilon_{Bias}} = 1 \quad (64)$$

$$\frac{\partial \theta_G}{\partial \varepsilon_{ARW}} = 1 \quad (65)$$

Now that the partial derivatives are taken, the systematic error is evaluated by applying equation (3) to each partial derivative. Therefore, the systematic error becomes:

$$B_{\omega_G}^2 = \left(\frac{\partial \theta_G}{\partial \omega_E} * B_{\omega_E}\right)^2 + \left(\frac{\partial \theta_G}{\partial \varphi} * B_{\varphi}\right)^2 + \left(\frac{\partial \theta_G}{\partial \psi} * B_{\psi}\right)^2 + \left(\frac{\partial \theta_G}{\partial \varepsilon_{Bias}} * B_{\varepsilon_{Bias}}\right)^2 + \left(\frac{\partial \theta_G}{\partial \varepsilon_{ARW}} * B_{\varepsilon_{ARW}}\right)^2 \quad (66)$$

Once the systematic error is calculated, the random error can be calculated by applying equation (4) to the partial derivatives. Therefore, the random error becomes:

$$P_{\omega_G}^2 = \left(\frac{\partial \theta_G}{\partial \omega_E} * P_{\omega_E}\right)^2 + \left(\frac{\partial \theta_G}{\partial \varphi} * P_{\varphi}\right)^2 + \left(\frac{\partial \theta_G}{\partial \psi} * P_{\psi}\right)^2 + \left(\frac{\partial \theta_G}{\partial \varepsilon_{Bias}} * P_{\varepsilon_{Bias}}\right)^2 + \left(\frac{\partial \theta_G}{\partial \varepsilon_{ARW}} * P_{\varepsilon_{ARW}}\right)^2 \quad (67)$$

The estimated true values and their associated uncertainties can then be applied to the uncertainty equations to generate the systematic and random uncertainty. The values for the ARW and Bias of the gyroscope are based off the data sheet for the Honeywell IMU. A study conducted by John Wahr evaluating the rotation rate of the Earth determined that the classical astronomical techniques are accurate to about 0.2 to 0.4 msec [64]. Therefore, this nominal value equates to an average uncertainty of 5.020833E-08 degrees per hour associated with rotational rate of the Earth. Next, the location of the gyroscope with respect to Earth must be known to estimate the rate at which the gyroscope is spinning with Earth's rotation. To determine the location of the gyroscope, Google Earth was used to provide the latitude and longitude of the sensor location. However, Google Earth does not provide the uncertainties associated with the coordinate positions generated by the program. Therefore, a literature search was conducted and an article by Mohammed et. al was found discussing the uncertainties associated with these

measurements. Their findings concluded that the average height difference observed from the supplied Google Earth value was 1.73 meters [65]. This value is then translated into the uncertainty associated with the latitude which was found to be 2.71543E-07 degrees. These values can then be broken down into estimated true values, systematic uncertainty, and random uncertainty as seen in Table 45.

Variable	Estimated True Value	Systematic Uncertainty	Random Uncertainty
Earth's Rotation (ω_E)	15.041 (deg/hr)	0 (deg/hr)	5.20E-8 (deg/hr)
Latitude Location (φ)	37.086 (deg)	0 (deg)	2.71543E-7 (deg)
X-Axis Offset (ψ)	0 deg	0 (deg)	2.71543E-7 (deg)
Bias Error (ϵ_{Bias})	0.25 (deg/hr)	0.25 (deg/hr)	0 (deg/hr)
ARW Error (ϵ_{ARW})	0.04 degrees/ \sqrt{hour}	0 (deg/hr)	0.04 degrees/ \sqrt{hour}

Table 45: True and Uncertainty Values of Gyroscope

The quantified values can then be applied to equations 3 and 4 to determine the systematic and random error within the gyroscope. The values are then summed together and the square root is taken, seen in equation 5, to calculate the total uncertainty of the gyroscope. The uncertainty of the gyroscope is then multiplied by the coverage factor of 2 to achieve a 1 sigma deviation in the following manner [55]:

$$\text{Expanded Uncertainty} = \text{coverage factor} * \text{calculated total uncertainty} \quad (68)$$

Therefore, to achieve an uncertainty of ± 0.1 degrees within a 95% confidence interval the gyroscope must be operated for no longer than 11 minutes as seen in Figure 65.

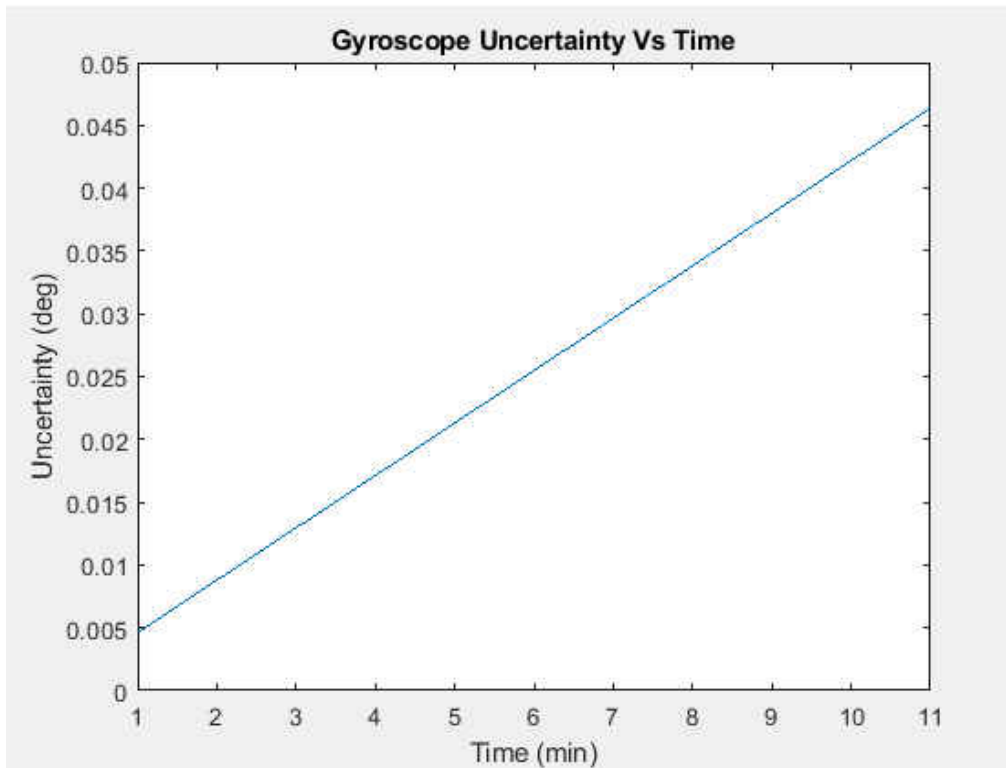


Figure 65: Gyroscope Uncertainty over time

4.2 Monte Carlo Method

The Monte Carlo Method is a powerful tool used to analyze the uncertainties associated with systems containing complex equations as an alternative method to propagation of error and where correlation among error sources may exist. This analysis begins by inputting the assumed true values of each variable used to model the system into the simulator. Once the assumed true values are entered, the associated random and elemental systematic uncertainties pertaining to these values must be entered into the simulation. Typically, these values use a Gaussian distribution, however, other distributions can be used to represent the uncertainties [55]. After determining the parent distribution of the uncertainties, the simulation can begin. Each estimated true value is given an associated uncertainty from the parent Gaussian distribution. Once the

uncertainty is added to the estimated true value, the model uses this value in the system's equations to produce a result that represents the calculated system output. The process is repeated N number of times until the desired sample size is obtained. Ideally, 10,000 iterations is usually a sufficient sample size when analyzing the uncertainties associated with the system, however, more iterations may be needed for the system to properly converge [55]. Once the values are calculated within the simulator, the mean and standard deviation of the values are used to determine the uncertainty associated with the system. The direct Monte Carlo Method can be summarized in a simple flow chart for visual interpretation of the process as seen in Figure 66.

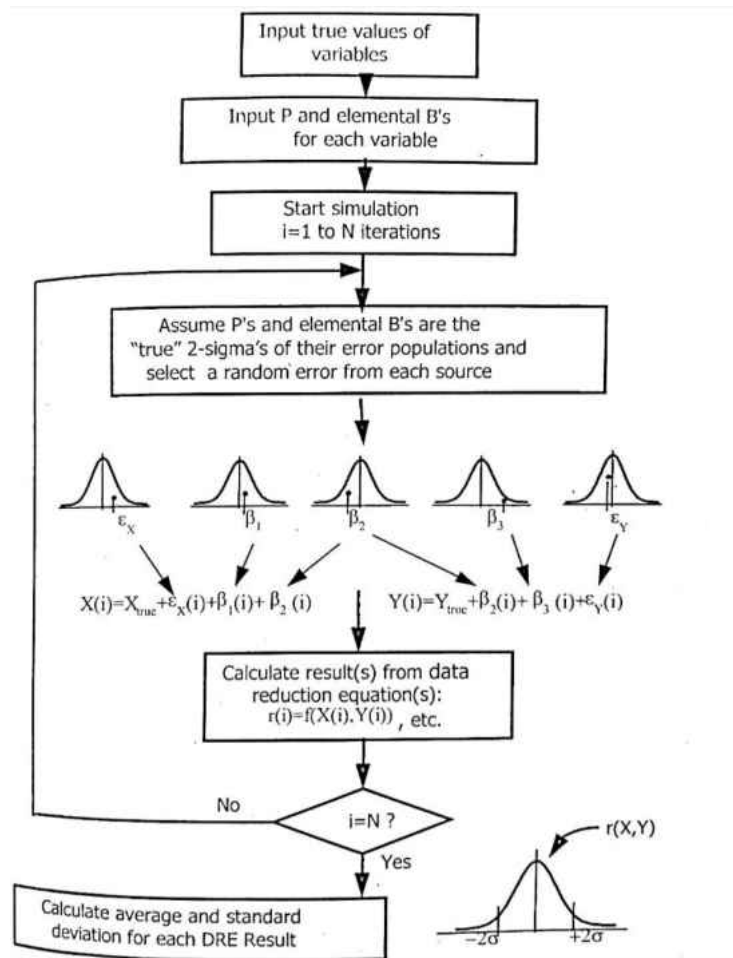


Figure 66: Direct Monte Carlo Method Flowchart [55]

4.2.1 Gyroscope

Given the ease of application of the Monte Carlo Method, it was in the best interest of the sensor analysis to analyze the IMU using the Monte Carlo Method. Not only will this provide a better understanding of the uncertainty associated with sensor, but it will also aid in the justification of choosing the IMU over the other techniques. This analysis will begin using equation 60 derived previously:

$$\theta_G = (\omega_E \cos\phi \cos\psi + \varepsilon_{bias} + \varepsilon_{ARW}) * time \quad (60)$$

The estimated true values associated with the variables in equation 67 are as follows:

- $W_E = 15.041$ deg/hour (Earth's rotation rate)
- $\varphi = 37.086$ degrees (Latitude position of Gyroscope)
- $\psi = 0$ degrees (X-Axis Offset of Gyroscope)
- $\alpha_i = 10$ degrees (Incremental change in angle)
- $\varepsilon_{bias} = 0.25$ degrees/hour (Bias error in gyroscope)
- $\varepsilon_{ARW} = 0.04$ degrees/ \sqrt{hour} (angle random walk of gyroscope)

Note, the uncertainty associated with time is very small therefore it will not be accounted when applying uncertainties to each value. Following the procedure of the Monte Carlo Method, the uncertainties of each variable must be generated to continue the analysis. These values will remain the same to keep the analysis consistent with the propagation of error analysis. For this simulation, the sample size used was 10,000 and the amount of time the gyroscope was simulated to be on for was 12 minutes. After the simulation was conducted, the expanded uncertainty associated with the gyroscope was found to be 0.0996 degrees.

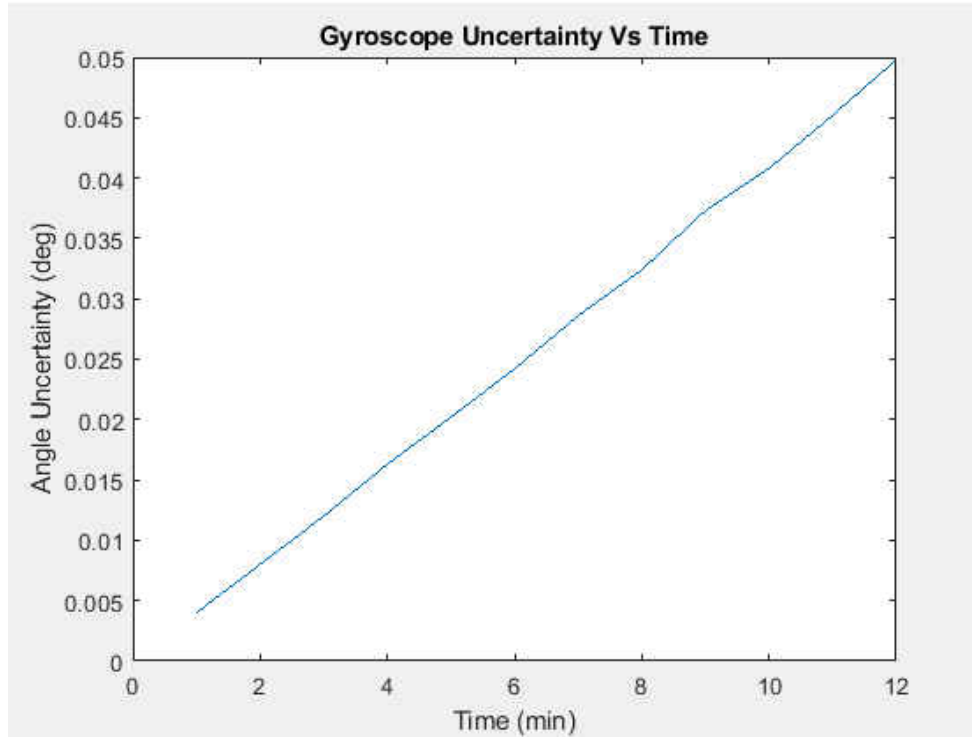


Figure 67: Gyroscope uncertainty over time

When compared to the propagation of error technique, the results coincide with each other only differing by 1 minute. Therefore, the confidence in choosing the IMU over the other three methods is greater and better justified.

CHAPTER 5

PROPOSED CALIBRATION METHOD

The new calibration method will involve mounting the modified AMS bracket accommodating the IMU to the blade grip. This will be achieved by drilling and tapping four precise holes on the bottom of the current AMS bracket that will allow for the IMU to be securely attached. By utilizing the current AMS bracket, the production time and cost will be reduced and fitment issues should not be present when mounting the newly modified bracket to the blade grips. The IMU being used for the new calibration method will be the Honeywell HG4930 due to its low drift of $0.04 \frac{\text{degrees}}{\sqrt{\text{hr}}}$ and small bias error of $0.25 \frac{\text{degrees}}{\text{hr}}$. These values are used during the uncertainty analysis conducted in the previous section determining that this sensor will be able to accurately measure the blade positions.

Once the modified AMS brackets are mounted to each blade grip the new calibration process can be conducted. This process begins by ensuring the swashplate is completely level utilizing the four AMS packages individually mounted to each blade. By integrating an AMS package on each blade, the operator is able to see the swashplate angle in each quadrant simultaneously. This method is superior to the previous method since multiple measurements and movement of equipment position are not needed. Therefore, all the operator has to do is adjust the control inputs of the swashplate until all AMS packages read zero degrees. Once the swashplate is level, the focus is shifted towards calibrating the blades attached to the hub. This process begins by ensuring the blade is set to a zero reference, meaning that the pitch, flap, and lead-lag angles are all set to zero. The zeroing of the pitch and flap will be done using the attached AMS package and the lead-lag position will be zeroed using the existing marks on the

hub and rotor cuff link. Once the blades are in their respective zero position, the blades will be ready for calibration to begin. The calibrator will then move the blade in the maximum positive pitch, flap, and lag angle desired and data will be taken. The blade should then be moved back to the zero reference to reorient the IMU. After the IMU is reoriented, the blade will then be moved to the maximum negative pitch, flap, and lag angle desired and data will be taken. The blade will then be moved back to the reference position so the IMU is reoriented once again. After each of the three data points are taken, the blade sensors will be zeroed, assuming there are no interactions between each degree of freedom.

Data acquisition will be done with the current open channels in the National Instruments (NI) server being used. The data from the AMS package and the IMU will be coupled together for full system evaluation. To ensure that both sensors capture similar data, they will be sampled at the same rate and initialized at the same time. The AMS package will provide a direct angle output using its transformation equations relating the inertial movements the sensor experiences to blade orientation. The IMU package will require a set of transformation equations as well that associate its inertial and gyroscopic movements. The inertial movements will be transformed using the XYZ Euler sequence in the following manner:

This process begins by combining equations 6-8 from the uncertainty analysis section with the z-axis aligned downward [57]:

$$R_{xyz} = R_x(\phi)R_y(\theta)R_z(\psi) \begin{pmatrix} 0 \\ 0 \\ 1 \end{pmatrix} \quad (69)$$

This is then simplified to [57]:

$$R_{xyz} = \begin{pmatrix} -\sin(\theta) \\ \cos(\theta) \sin(\phi) \\ \cos(\theta) \cos(\phi) \end{pmatrix} \quad (70)$$

Equation (63) is then rewritten to relate the roll and pitch angles to the accelerometer readings

A_i :

where

$$i = x, y, z$$

$$\frac{A_i}{\|A_i\|} = \begin{pmatrix} -\sin(\theta) \\ \cos(\theta) \sin(\phi) \\ \cos(\theta) \cos(\phi) \end{pmatrix} \quad (71)$$

The roll and pitch angles are then solved from equation 70 [57]:

$$\text{(roll) } \tan(\phi) = \frac{A_y}{A_z} \quad (72)$$

$$\text{(pitch) } \tan(\theta) = \frac{-A_x}{\sqrt{A_y^2 + A_z^2}} \quad (73)$$

Note, the sensor output will be in millivolts therefore the sensitivity of the sensor must be taken into consideration to convert the voltage output to an experienced sensor acceleration. This is done by dividing the voltage output by the sensor sensitivity:

$$A_i = \frac{mV}{\text{Sensitivity}} = \text{gravitational acceleration } (g) \quad (74)$$

The gyroscopic movements will be transformed into real-time angle measurements using time integration. Time integration must be used to determine the delta angle the gyroscope moved

since the output is an angular velocity. Therefore, the gyroscope output will be modeled in the following manner:

$$\theta(t) = \int_0^t \frac{d\theta}{dt} dt \quad (75)$$

where

$$\frac{d\theta}{dt} = \frac{mV}{Sensitivity} = \text{measured angular velocity} \left(\frac{deg}{s} \right) \quad (76)$$

Similar to the accelerometer data, the gyroscope indirectly outputs the angular velocity through a voltage signal. This voltage is then divided by the sensitivity of the sensor deriving the angular velocity the sensor is experiencing.

This proposed method has the potential to reduce the current calibration time of three hours per blade to approximately thirty minutes or less per blade. This drastic time reduction would result in user satisfaction as well as reduced operating costs. Also, if problems arise during testing, the blades should be able to be calibrated within the same day of operation. Another advantage of using the new proposed method is having the ability to compare the data from the AMS package and the IMU. Not only will this aid in the accuracy and repeatability of the calibration process, it allows a comparison study to be conducted between the two sensors. If the two sensors are found to be in agreement with each other, there is the potential to only use the IMU for the full calibration. This will reduce the calibration equipment cost as well as increase the robustness of the calibration itself.

CHAPTER 6

CONCLUSION AND FUTURE WORK

During investigation of the current calibration method, the rotorcraft testing hub was analyzed and deemed to have a larger error than the desired ± 0.1 degree tolerance. This discovery led to a literature review analyzing various new methods that could be used to increase the accuracy of the system. These included using a laser tracker system, a photogrammetry system, a coordinate measurement arm, or an inertial based measurement device. Upon discovering these four new methods, an uncertainty analysis was conducted to aid in choosing the best option of the four. During this analysis it was found that the laser tracker system and the photogrammetry system had the best accuracy, however, they were the most sophisticated systems in terms of set up and data analysis. Therefore, due to the ease of integration and simplicity of data reduction, the Honeywell IMU was the chosen sensor to conduct the new calibration. Once the sensor was chosen, a new calibration method was proposed providing the necessary equations for converting the sensor outputs to angle outputs. This new method suggests that the calibration time can be reduced to 30 minutes or less per blade versus 3 hours as well as increase user friendliness of the calibration operation by being able to calibrate all factors at one time. Unfortunately, the new calibration method was unable to be implemented in time to test and report results for this thesis due to resource constraints.

Given the resource constraints, future work involving implementing the new calibration method is needed to verify that it will be an improvement over the current method. After implementing the new method, data collection and analysis will be performed of the system. This data will then be compared to the current calibration method to determine if the new method

contains less error. Also, a comparison study between the AMS package and the IMU can be conducted to determine if they are in agreement. If they are in agreement, there is a potential to only use the IMU for the full calibration of the pitch, flap, and lead-lag sensors. Furthermore, it would be of interest to implement the new calibration method for leveling of the swashplate using the onboard IMU sensors to reduce the swashplate leveling time.

REFERENCES

- [1] Dissymmetry of lift. (n.d.). Retrieved from <http://www.helicopterinstruction.com/dissymmetry-of-lift/>
- [2] Etl. (2018, August 25). What is the Coriolis effect? Retrieved from <https://www.thehelicopterstudyguide.com/what-is-the-coriolis-effect/>
- [3] Daniels, A. (2016). Rotorcraft Design 1 Day 3: Parametric Design Analysis [PowerPoint Slides]. Retrieved from <https://slideplayer.com/slide/6040240/>
- [4] Sekula, M., & Gandhi, F. (1999). Influence of controlled blade lead-lag motions on helicopter vibrations. In 40th Structures, Structural Dynamics, and Materials Conference and Exhibit (p. 1223).
- [5] E.L. Houghton, P.W. Carpenter, Steven H. Collicott, Daniel T. Valentine, Chapter 5 - Wing Theory, Editor(s): E.L. Houghton, P.W. Carpenter, Steven H. Collicott, Daniel T. Valentine, Aerodynamics for Engineering Students (Sixth Edition), Butterworth-Heinemann, 2013, Pages 269-347,
- [6] Dissymmetry of lift. (n.d.). Retrieved from <http://www.helicopterinstruction.com/dissymmetry-of-lift/>
- [7] Cantrell, P. (n.d.). Semi-Rigid Main Rotors. Retrieved from http://www.copters.com/mech/mr_semi.html
- [8] Cepeda-Gomez, R. (2019). Delayed feedback control of pitch-flap instabilities in helicopter rotors. In Stability, Control and Application of Time-delay Systems (pp. 123-142). Butterworth-Heinemann.

- [9] FAA. (n.d.). ALC_Content. Retrieved from https://www.faa.gov/gslac/ALC/course_content.aspx?CID=104&SID=449&preview=true
- [10] Montgomery, D. C. (2013). Design and analysis of experiments. (p. 449 – 477)
- [11] Lau, K, Qiao, H, & Song, H . (2016). Design and Testing of the API Real-time Metrology System for FAST [PowerPoint slides]. Retrieved from <http://www.gb.nrao.edu/MetConf/talks/Friday/Lau.pdf>
- [12] [Automated Precision]. (2019, May 10). Dr. Lau | Inventor of the Laser Tracker | Part 1 [Video File]. Retrieved from <https://www.youtube.com/watch?v=N68bfXOa1qk>
- [13] Greeff, G. P. (2010). A study for the development of a laser tracking system utilizing multilateration for high accuracy dimensional metrology (Doctoral dissertation, Stellenbosch: University of Stellenbosch).
- [14] Radian Laser Trackers. (2019, July 17). Retrieved from <https://apimetrology.com/laser-trackers/>
- [15] Tkachenko, N. V. (2006). Optical spectroscopy: methods and instrumentations. Elsevier. (p. 15-38)
- [16] Muralikrishnan, B., Phillips, S., & Sawyer, D. (2016). Laser trackers for large-scale dimensional metrology: A review. *Precision Engineering*, 44, 13-28.
- [17] Robert E. Parks "Prism alignment using a point source microscope", *Proc. SPIE 11103, Optical Modeling and System Alignment*, 1110303 (30 August 2019); <https://doi.org/10.1117/12.2526534>

- [18] Faro Technologies. (2017, August 2). Understanding Laser Tracker targets – FARO. Retrieved from <https://insights.faro.com/calibration/understanding-laser-tracker-targets>
- [19] Lockwood, A. (2013, November 26). High-speed ADM Distance Measurement in Laser Tracking Applications. Retrieved from <https://www.digitalengineering247.com/article/high-speed-adm-distance-measurement-in-laser-tracking-applications/>
- [20] What is an Interferometer? (n.d.). Retrieved from <https://www.ligo.caltech.edu/page/what-is-interferometer>
- [21] The Center for Photogrammetric Training. (2006). History of Photogrammetry. Retrieved from https://ibis.geog.ubc.ca/courses/geob373/lectures/Handouts/History_of_Photogrammetry.pdf
- [22] Choo, D. (1998). Michelson-Morley Experiment . Retrieved from <http://visav.phys.uvic.ca/~babul/ASTRO/DebbieC/mme.html>
- [23] Mechelson Interferometer. (n.d.). Retrieved April 10, 2020, from <https://www.mpoweruk.com/figs/Michelson-Interferometer.htm>
- [24] Zygo CorporationMar. (2019, August 7). Distance Measuring Interferometry – The Art of Fringe Counting. Retrieved from <https://www.azonano.com/article.aspx?ArticleID=4818>
- [25] Martin, J. (2015). Tracking Progress: RE-EVALUATING LASER TRACKER TECHNOLOGY. *Quality*, 54(1), 32.
- [26] Wright, I. (2019, April 17). How to Avoid 3 Common Mistakes When Using Laser Trackers - Automated Precision. Retrieved from <https://apisensor.com/avoid-3-common-mistakes-using-laser-trackers/>

- [27] Zappa, E., Liu, R., Trainelli, L., Ferrario, A., Cordisco, P., Terraneo, M., ... & Redaelli, M. (2018). Laser and vision-based measurements of helicopter blade angles. *Measurement*, 118, 29-42.
- [28] Olague G. (2016) Vision and Evolution: State of the Art. In: *Evolutionary Computer Vision*. Natural Computing Series. Springer, Berlin, Heidelberg
- [29] Publishing, P. (2019, August 14). How Does Photogrammetry Work? Retrieved from <https://www.photomodeler.com/how-does-photogrammetry-work/>
- [30] Baqersad, J., Poozesh, P., Niezrecki, C., & Avitabile, P. (2017). Photogrammetry and optical methods in structural dynamics—A review. *Mechanical Systems and Signal Processing*, 86, 17-34.
- [31] Remondino, F., & Fraser, C. (2006). Digital camera calibration methods: considerations and comparisons. *International Archives of Photogrammetry and Remote Sensing*, 36 (5), 266-272.
- [32] EE Publishers. (2018, May 24). Fig. 1 - Two RAD targets. Retrieved from <https://www.ee.co.za/article/automating-photogrammetry-with-coded-targets.html/fig-1-two-rad-targets>
- [33] Walford, A. (2019, July 18). Photogrammetry Targets & Coded Targets. Retrieved from <https://www.photomodeler.com/the-other-photogrammetry-automation-coded-targets/>
- [34] Adi K. & Widodo C. (2017 November). Distance Measurement with a Stereo Camera. *International Journal of Innovative Research in Advanced Engineering*. Volume 4. Issue 11.
- [35] Huang, Y., Cheng, W., Li, Y., & Li, W. (2012, November). An optoelectronic system for the in-flight measurement of helicopter rotor blades' motions and strains. In *Optical Metrology*

and Inspection for Industrial Applications II (Vol. 8563, p. 85630X). International Society for Optics and Photonics.

[36] A Brief History Of CMM Technology. (2019, November 14). Retrieved from <https://status-cmm.co.uk/blog/a-brief-history-of-cmm-technology/>

[37] FaroArm® - Portable 3D Measurement Arm for any application. (2019, November 5). Retrieved from <https://www.faro.com/products/3d-manufacturing/faroarm/>

[38] 6" Magnetic Mount for Portable CMM with 3 1/2" threaded ring. (n.d.). Retrieved April 10, 2020, from <https://www.metrologyworks.com/product/6-magnetic-mount-for-portable-cmm-with-3-12-threaded-ring/>

[39] Smith , K. (2006, December 1). Options Abound in the World of Large-Part Metrology . Retrieved from https://www.qualitydigest.com/sept03/articles/02_article.shtml

[40] https://www.precisionballs.com/all_kinematic_platforms.php

[41] Crause, L. A., O'Donoghue, D. E., O'Connor, J. E., & Strümpfer, F. (2010, July). Use of a Faro Arm for optical alignment. In Modern Technologies in Space-and Ground-based Telescopes and Instrumentation (Vol. 7739, p. 77392S). International Society for Optics and Photonics.

[42] Passaro, V., Cuccovillo, A., Vaiani, L., De Carlo, M., & Campanella, C. E. (2017). Gyroscope technology and applications: A review in the industrial perspective. *Sensors*, 17(10), 2284.

[43] Gravity Probe B - Testing Einstein's Universe . (2005, February 1). Retrieved from http://einstein.stanford.edu/content/fact_sheet/GPB_FactSheet-0405.pdf

[44] Weapons and System Engineering Department United States Naval Academy . (n.d.). Ring Laser Gyro. Retrieved April 10, 2020, from <https://fas.org/man/dod-101/navy/docs/fun/rlg.htm>

[45] Shiner, L. (2002, August 31). How Things Work: Ring Laser Gyros. Retrieved from <https://www.airspacemag.com/flight-today/how-things-work-ring-laser-gyros-32371541/?page=2>

[46] Encyclopaedia Britannica. (2020, February 19). Ring laser gyroscope. Retrieved from <https://www.britannica.com/technology/ring-laser-gyroscope>

[47] Wang, R., Zheng, Y., Yao, A., & Langley, D. (2003). Modified Sagnac experiment for measuring travel-time difference between counter-propagating light beams in a uniformly moving fiber. *Physics Letters A*, 312(1-2), 7-10.

[48] Marett, D. (2010, May 12). How to Build a Sagnac Interferometer/ Fiber Optic Gyroscope (FOG). Retrieved from <http://www.conspiracyoflight.com/Sagnac/Sagnac.html>

[49] Semiconductor Digest . (2016, February 1). Introduction to MEMS gyroscopes | Solid State Technology. Retrieved from <https://sst.semiconductor-digest.com/2010/11/introduction-to-mems-gyroscopes/>

[50] Watson, J. MEMS Gyroscope Provides Precision Inertial Sensing in Harsh, High Temperature Environments.

[51] Fu, X., He, L., & Qiu, H. (2013, May). MEMS gyroscope sensors for wind turbine blade tip deflection measurement. In 2013 IEEE International Instrumentation and Measurement Technology Conference (I2MTC) (pp. 1708-1712). IEEE.

- [52] Allred, C. J., Churchill, D., & Buckner, G. D. (2017). Real-time estimation of helicopter rotor blade kinematics through measurement of rotation induced acceleration. *Mechanical Systems and Signal Processing*, 91, 183-197.
- [53] Ku, H. H. (1965). Notes on the use of propagation of error formulas. doi: 10.6028/nbs.rpt.9011
- [54] Appendix B: Taylor Series Method (TSM) for Uncertainty Propagation. (n.d.). *Experimentation, Validation, and Uncertainty Analysis for Engineers*, 257–269. doi: 10.1002/9780470485682.app2
- [55] Coleman, H. W., & Steele, W. G. (1999). *Experimentation and Uncertainty Analysis for Engineers*. Hoboken, NJ, United States: Wiley.
- [56] Diebel, J. (2006). Representing Attitude: Euler Angles, Unit Quaternions, and Rotation Vectors. doi: 10.3897/bdj.4.e7720.figure2f
- [57] Pedley, M. (2013). Tilt sensing using a three-axis accelerometer. Freescale semiconductor application note, 1, 2012-2013.
- [58] Alternative Photography Posted in Cameras. (2019, July 16). How a pinhole camera works. Retrieved December 11, 2019, from <https://www.alternativephotography.com/how-a-pinhole-camera-works/>.
- [59] Monari, E., Maerker, J., & Kroschel, K. (2009). A Robust and Efficient Approach for Human Tracking in Multi-camera Systems. 2009 Sixth IEEE International Conference on Advanced Video and Signal Based Surveillance. doi: 10.1109/avss.2009.16

- [60] Schreve, K. (2014, September). How accurate can a stereovision measurement be?. In 15th International Workshop on Research and Education in Mechatronics (REM) (pp. 1-7). IEEE.
- [61] Peters, T. M., & Ellis, R. E. (2003). Medical image computing and computer-assisted intervention - Miccai 2003: 6th International Conference, Montréal, Canada, November 2003: proceedings. Springer Science & Business Media
- [62] FARO Technologies, Inc. (2018, March 5). Accuracy Specifications for the Gage Arm. Retrieved December 10, 2019, from https://knowledge.faro.com/Hardware/Legacy-Hardware/Gage/Accuracy_Specifications_for_the_Gage_Arm.
- [63] Luo, J., Wang, Z., Shen, C., Kuijper, A., Wen, Z., & Liu, S. (2016). Modeling and Implementation of Multi-Position Non-Continuous Rotation Gyroscope North Finder. *Sensors*, 16(9). doi: 10.3390/s16091513
- [64] Wahr, J. (1985). The Earth's Rotation Rate: Precise measurements of fluctuations in the length of day are revealing the effects of a surprising variety of geophysical phenomena, even atmospheric winds. *American Scientist*, 73(1), 41-46. Retrieved April 10, 2020, from www.jstor.org/stable/27853060
- [65] Mohammed, N. Z., Ghazi, A., & Mustafa, H. E. (2013). Positional accuracy testing of Google Earth. *International Journal of Multidisciplinary Sciences and Engineering*, 4(6), 6-9.

APPENDIX

Camera Uncertainty

```

clc; clear all; close all;

syms d f u v s x y z theta u1 u2 v1 v2 su1 su2 sv1 sv2 sd sf stheta

R = [cos(theta),0,sin(theta);0,1,0;-sin(theta),0,cos(theta)];

C = [d*sin(theta);0;d-d*cos(theta)];

T = -R*C;

A = [-f,0,0,0;0,-f,0,0;0,0,1,0];

RR = [- sin(theta)*(d - d*cos(theta)) - d*cos(theta)*sin(theta);
      0;
      d*sin(theta)^2 - cos(theta)*(d - d*cos(theta));1];

LL = [cos(theta),0,sin(theta);0,1,0;-sin(theta),0,cos(theta);0,0,0];

b = [LL,RR];

comb = A*b;

R1 = u1*A(3,:)-A(1,:);
R2 = v1*A(3,:)-A(2,:);
R3 = u2*comb(3,:)-comb(1,:);
R4 = v2*comb(3,:)-comb(2,:);

```

```

% R1 = u1*(A(3,:)-A(1,:));
% R2 = v1*(A(3,:)-A(2,:));
% R3 = u2*(comb(3,:)-comb(1,:));
% R4 = v2*(comb(3,:)-comb(2,:));

AA = [R1;R2;R3;R4];

Cart = [x;y;z;1];

eq = AA*Cart==0;

solx = solve(eq);

X = simplify(solx.x);
Y = simplify(solx.y);
Z = simplify(solx.z);

% partial derivatives of X

dx1 = simplify(diff(X,u1));
dx2 = simplify(diff(X,u2));
dx3 = simplify(diff(X,d));
dx4 = simplify(diff(X,f));
dx5 = simplify(diff(X,theta));

Ux = sqrt((dx1*su1)^2+(dx2*su2)^2+(dx3*sd)^2+(dx4*sf)^2+(dx5*stheta)^2);

% partial derivatives of Y

dy1 = simplify(diff(Y,u1));
dy2 = simplify(diff(Y,u2));
dy3 = simplify(diff(Y,d));

```

```

dy4 = simplify(diff(Y,f));
dy5 = simplify(diff(Y,theta));
dy6 = simplify(diff(Y,v2));

Uy = sqrt((dy1*su1)^2+(dy2*su2)^2+(dy3*sd)^2+(dy4*sf)^2+(dy5*stheta)^2+(dy6*sv2)^2);

% partial derivatives of Z
dz1 = simplify(diff(Z,u1));
dz2 = simplify(diff(Z,u2));
dz3 = simplify(diff(Z,d));
dz4 = simplify(diff(Z,f));
dz5 = simplify(diff(Z,theta));

Uz = sqrt((dz1*su1)^2+(dz2*su2)^2+(dz3*sd)^2+(dz4*sf)^2+(dz5*stheta)^2);

% define variables
Utotal = zeros(7,1);
for i = 1:7
u1 = 0;
su1 = 0.68E-6; %micrometers
u2 = u1;
su2 = su1;
v1 = 0;
sv1 = su1;
v2 = v1;
sv2 = sv1;
f = 70;
sf = 24E-9; %m
d = i*1000; %mm
sd = sf; %m

```

```
theta = deg2rad(30);  
stheta = deg2rad(0.005/3600);  
  
UX = double(subs(Ux));  
  
UY = double(subs(Uy));  
  
UZ = double(subs(Uz));  
  
Utotal(i) = sqrt(UX^2+UY^2+UZ^2)  
end
```

[Published with MATLAB® R2019b](#)

Laser Tracker Uncertainty

```

syms d theta phi dd dtheta dphi
% Define functions that model laser tracker

X = d*cosd(theta)*sind(phi);
Y = d*sind(theta)*sind(phi);
Z = d*cosd(phi);

% Take partial derivatives

dX = sqrt((diff(X,d)*dd)^2+(diff(X,theta)*dtheta)^2+(diff(X,phi)*dphi)^2);
dY = sqrt((diff(Y,d)*dd)^2+(diff(Y,theta)*dtheta)^2+(diff(Y,phi)*dphi)^2);
dZ = sqrt((diff(Z,d)*dd)^2+(diff(Z,theta)*dtheta)^2+(diff(Z,phi)*dphi)^2);

%
% Define values
distance = 60; %meters
for d = 1:distance
    %d = 5; % meters
    dd = .0000005; %meters
    theta = 0; % degrees (max pitch)
    dtheta = 0.000015+(0.000006*d); %meters + 6 microm/m
    % convert dtheta from m/m to deg/deg
    step1 = d*sind(theta);
    step2 = step1+dtheta;
    step3 = asind(step2/d);
    dtheta = step3-theta;

    phi = 0; %degrees (max yaw)
    dphi = dtheta; %meters

```



```
% plug variables in
```

```
dX1 = double(subs(dX));
```

```
dY1 = double(subs(dY));
```

```
dZ1 = double(subs(dZ));
```

```
% Total Uncertainty
```

```
Ulaser(d) = dX1+dY1+dZ1; %meters
```

```
Ulaserd(d) = atan(Ulaser(d)/distance); %degrees
```

```
end
```

Published with MATLAB® R2019b

Coordinate Measurement Arm Uncertainty

```

Count = 10;
P1 = [1 2 3];
a = 0.01;
%b = 2;
D = 1.5;

UFarom = zeros(Count,1);
UFarod = zeros(Count,1);

for k = 1:Count
    a = a+0.19;
    %b = b+1;
    % Define givens
    P2 = [a 2 3];

    dx1 = 0.000005;
    dx2 = dx1;
    dy1 = 0.000005;
    dy2 = dy1;
    dz1 = 0.000005;
    dz2 = dz1;

    % Determine uncertainty in distance
    Udd(k) = sqrt(((P2(1)-P1(1))^2*(P1(1)^2*dx1^2+P2(1)^2*dx2^2)+...
        (P2(2)-P1(2))^2*(P1(2)^2*dy1^2+P2(2)^2*dy2^2)+...
        (P2(3)-P1(3))^2*(P1(3)^2*dz1^2+P2(3)^2*dz2^2))/...
        ((P2(1)-P1(1))^2+(P2(2)-P1(2))^2+(P2(3)-P1(3))^2)); %meters
    UDD(k) = atan(Udd(k)/D);

    syms ax ay az bx by bz dax day daz dbx dby dbz

```

```
Theta = acos((ax*bx + ay*by + az*bz)/(sqrt(ax^2+ay^2+az^2)*sqrt(bx^2+by^2+bz^2)));
```

```
Utheta = sqrt((diff(Theta,ax)*dax)^2+(diff(Theta,ay)*day)^2+(diff(Theta,az)*daz)^2+...
    (diff(Theta,bx)*dbx)^2+(diff(Theta,by)*dby)^2+(diff(Theta,bz)*dbz)^2);
```

```
% substitue values in
```

```
ax = P1(1);ay = P1(2);az = P1(3);
```

```
bx = P2(1);by = P2(2);bz = P2(3);
```

```
dax = 0.000005;
```

```
day = dax;
```

```
daz = dax;
```

```
dbx = 0.000005;
```

```
dby = dbx;
```

```
dbz = dbx;
```

```
UTheta(k) = double(subs(Utheta)); %degrees
```

```
% % Combine both uncertainties in degrees
```

```
UFarod(k) = UTheta(k) + UDD(k); %degrees
```

```
theta(k) = tan(a/D);
```

```
end
```

[Published with MATLAB® R2019b](#)

Gyroscope Uncertainty

```

clc; clear all; close all;

% Define variables in data reduction equation

syms We sWe rWe Psi sPsi rPsi Phi sPhi rPhi ebias sbias rbias earw sarw rarw t st rt

% Define data reduction equation

Utheta = (We*cos(Phi)*cos(Psi)+ebias+earw)*t;

% Take partial derivatives of data reduction equation

partWe = diff(Utheta,We); % partial derivative with respect to We

partPsi = diff(Utheta,Psi); % partial derivative with respect to Psi

partPhi= diff(Utheta,Phi); % partial derivative with respect to Phi

partebias = diff(Utheta,ebias); % partial derivative with respect to Bias error

partearw = diff(Utheta,earw); % partial derivative with respect to ARW error

partt = diff(Utheta,t); % partial derivative with respect to time

% Application of Systematic and Random Error
errortype = 1;

if errortype==1 % Error without time uncertainty

BUtheta = sqrt((partWe*sWe)^2 + (partPsi*sPsi)^2 + (partebias*sbias)^2 + ...

```

```

(partearw*sarw)^2) + (partPhi*sPhi)^2; % Systematic Error

PUtheta = sqrt((partWe*rWe)^2 + (partPsi*rPsi)^2 + (partebias*rbias)^2 + ...
(partearw*rarw)^2) + (partPhi*rPhi)^2; % Random Error

elseif errortype==2 % Error with time uncertainty

BUtheta = sqrt((partWe*sWe)^2 + (partPsi*sPsi)^2 + (partebias*sbias)^2 + ...
(partearw*sarw)^2 + (partt*st)^2); % Systematic Error

PUtheta = sqrt((partWe*rWe)^2 + (partPsi*rPsi)^2 + (partebias*rbias)^2 + ...
(partearw*rarw)^2 + (partt*rt)^2); % Random Error
end

% Apply values to propagation of error

time = 12; % Time gyro on (min)

for t = 1:time
% Define Variables and Uncertainties
We = 15.041/60; % Earth rotation (deg/min)
sWe = 0;
rWe = 5.2E-8; % Earth rotation uncertainty (deg/min)
Phi = 37.086; % Latitude location of gyroscope (deg)
sPhi = 0;
rPhi = 2.71543E-7; %Latitude location uncertainty (deg)
Psi = 0; % X-Axis offset (deg)
sPsi = 76.38;
rPsi = 2.71543E-7; % X-Axis offset uncertainty (deg)
ebias = 0.25;
sbias = 0.25/60; % Gyro bias error (deg/min)

```

```
rbias = 0;
earw = 0.0016;
sarw = 0;
rarw = 0.0016/60; % Gyro ARW error (deg/min)
%t = 23; % Time gyro on (min)
st = 0; % Time uncertainty (min)
rt = 0.001; % Time uncertainty (min)

BUtheta(t) = double(simplify(subs(BUtheta)));
PUtheta(t) = double(simplify(subs(PUtheta)));

Utheta(t) = BUtheta(t) + PUtheta(t);
end

Ugyro = Utheta(time)
```

[Published with MATLAB® R2019b](#)

Gyroscope Monte Carlo

```

clc; clear all; close all;

nsamples = 10000; % Sample size
time = 12; % Amount of time the gyro is on (min)
We = 15.041/60; % Rotation of Earth in deg/min
Phi = 37.086; % Latitude of Gyroscope (deg)
Psi = 0; % X-Axis Offset (deg)
se = 0 + 0.25/60*randn(nsamples,1); % Bias error and ARW in deg/min
sarw = 0 + 0.04/60*randn(nsamples,1); % ARW error deg/sqrt(min)
sWe = We + (5.20*10^-8)*randn(nsamples,1); % Rotation of Earth with uncertainty (deg/min)
sPsi = Psi + (2.71543*10^-7)*randn(nsamples,1); % X-Axis Offset (deg)
sPhi = Phi + (2.71543*10^-7)*randn(nsamples,1); % Latitude with uncertainty (deg)
stime = time + (0.001)*randn(nsamples,1); % Time with uncertainty (min)

% Data Reduction Equation

Wge = (sWe.*cosd(sPhi).*cosd(sPsi)+se+sarw).*time; % Without time uncertainty

Wget = (sWe.*cosd(sPhi).*cosd(sPsi)+se+sarw).*stime; % With time uncertainty

% Data distribution plots

figure(1)
histogram(Wge)
xlabel('Angular Velocity (deg/min)')
ylabel('Frequency')
title('Normal Distribution without Time Uncertainty')
figure(2)
histogram(Wget)

```

```

xlabel('Angular Velocity (deg/min)')
ylabel('Frequency')
title('Normal Distribution with Time Uncertainty')

% Confidence Interval (without time uncertainty)

Wgesort = sort(Wge,'ascend'); %Reorder values from small to large
Wgelow = Wgesort(0.025*nsamples); % Left tail of distribution
Wgehigh = Wgesort(0.975*nsamples); % Right tail of distribution

% Confidence Interval (with time uncertainty)
Wgetsort = sort(Wget,'ascend'); % Reorder values from small to large
Wgetlow = Wgetsort(0.025*nsamples); % Left tail of distribution
Wgethigh = Wgetsort(0.975*nsamples); % Right tail of distribution

% Uncertainty

Uw = (Wgehigh-Wgelow)/4

Uwt = (Wgethigh-Wgetlow)/4

figure(3)

Ud = [0.004,0.008,0.012,0.0163,0.0202,0.0242,0.0286,...
0.0324,0.0373,0.0408,0.0452,0.0498];

tt = linspace(1,12,12);
plot(tt,Ud)
xlabel('Time (min)')
ylabel('Angle Uncertainty (deg)')
title('Gyroscope Uncertainty Vs Time')

```


Published with MATLAB® R2019b

VITA

NAME: Brian David Calvert Jr.

DATE OF BIRTH: February 4th, 1995

PERSONAL STATEMENT

A dynamic, team spirited and performance driven engineering student with an extraordinary blend of skills. Ability to communicate and motivate team members to enhance goals and objectives. Opportunity driven with creative problem solving and trouble shooting skills complimented by meticulous attention to detail and specifications.

EDUCATION

Old Dominion University (ODU)

MSc Aerospace Engineering 2018-Present

James Madison University (JMU)

BSc Engineering Class of 2018

WORK EXPERIENCE

Measurement Systems Intern

NASA Langley Research Center

Jun. 2019 – Dec. 2019

- During this internship I conducted the research presented in this thesis. As a generalized summary, I developed a new calibration method for rotorcraft blade angles that improved the weaknesses found in the current calibration method being used.

Mechanical Engineer Intern

RG Engineering

Jun. 2016 – Aug. 2016

- During this internship I conducted failure analysis studies on the main structures used in industrial printing presses.

KEY SKILLS

- **Programming Languages**
 - MATLAB/SIMULINK (Advanced),
- **Data Analysis Software**
 - Design Expert (Intermediate), JMP (Intermediate), Lab View (Novice)
- **CAD Software**
 - SOLIDWORKS, Autodesk Inventor
- **Other Software**
 - MS Office